Department of Physics
Indian Institute of Technology Guwahati
Ph.D. Thesis

Quantum conductance in spin-orbit coupled devices: A focus on transport in Graphene

Sudin Ganguly

Supervisor: Prof. Saurabh Basu

Quantum conductance in spin-orbit coupled devices: A focus on transport in Graphene

A thesis submitted by

Sudin Ganguly

to

Indian Institute of Technology Guwahati
in partial fulfillment of the requirements
for the award of the degree of
Doctor of Philosophy in Physics

Department of Physics
Indian Institute of Technology Guwahati
Guwahati - 781039, Assam, India

Statement

The work contained in the thesis entitled "*Quantum conductance in spin-orbit coupled devices: A focus on transport in Graphene*" has been carried out at the Department of Physics, Indian Institute of Technology Guwahati, India by me under the supervision of Prof. Saurabh Basu. The material of this thesis has not been has been submitted elsewhere for any other degree. Works presented in the thesis are all my own unless referenced to the contrary in the text.

(Sudin Ganguly) October 3, 2017
Department of Physics
Indian Institute of Technology Guwahati
Guwahati - 781039, India

Disclaimer

The bibliography included in this thesis is, by no means complete but contains the ones which are consulted thoroughly by me. I apologize for inadvertently missing out some of the research papers, review articles and other scientific documents pertaining to the focus of this thesis which should also have been cited. For illustration purpose some of the figures in this thesis are taken from other sources and properly cited.

Certificate

It is certified that the work contained in the thesis entitled “*Quantum conductance in spin-orbit coupled devices: A focus on transport in Graphene*” by Mr. Sudin Ganguly, a Ph.D. student of the Department of Physics, Indian Institute of Technology Guwahati is carried out under my supervision and has not been submitted elsewhere for the award of any other degree.

(Prof. Saurabh Basu) October 3, 2017
Department of Physics
Indian Institute of Technology Guwahati
Guwahati - 781039, India

Dedicated in the memory of BDR Sir,
my Mother and Father
&
My two sweet little angels
Ritoja and Prakriti

Acknowledgment

First and foremost, I would like to express my gratitude to my Ph.D. supervisor, Prof. Saurabh Basu, for accepting me in his research group. His knowledge, intelligent ideas, and energetic spirit have helped me to complete the thesis work successfully, well in time. He is one of the most energetic and enthusiastic person I have ever seen. You will always be a role model to me: a great supervisor, researcher, and human being. Thank you for inspiring me, guiding me, sharing the experience with me and caring for me throughout all these years.

I would like to thank the chairman of my doctoral committee Prof. Subharadip Ghosh, doctoral committee members Dr. Ashwini Kumar Sharma and Dr. Biplab Bose for reviewing my progress every year and for their frank comments and valuable suggestions. I am thankful to all other members of the Physics department for their friendly behaviour whenever it was needed.

I am grateful to Indian Institute of Technology Guwahati, and Government of India, Ministry of Human Resource Development for the financial support. I wish to thank Department of Physics, IIT Guwahati for providing me the necessary computational facilities. I thank all the technical assistants of the department of physics, especially Mr. Basab Bijoy Purkayastha, for their assistance in various ways during my research period.

I would like to thank my junior Noor for his silent cooperation, wish I had a senior like him. I would also like to thank my other group members Sunayana, Priyadarshini, Priyanka for their cooperation and assistance. I would like to thank my seniors Dr. Apurba Barman, Dr. Ramesh Ghosh, Dr. Tapash Singha and Dr. Kartik Sau for their help and support.

My MSc mate Biswajit deserves special thanks. The only reason I came to IIT Guwahati because he was here. In the last five years, I came too close to too many friends and have so much fun with them. We became a family together. They are Kallol, Koushik (KC), Anabil, Ramiz, Ashis, Sourav, Abhijit, Rahul. I would also like to thank my senior labmates, Himangshu (for his critical expertise in computer and computation related issues and Biriyani), Bappaditya, my friends Shibananda, Venkanna and my juniors Sayan (deep), Sanjib and Pratap. Another long list of friends is worth to mention in IIT Guwahati, my football mates, with them I enjoyed so much. Few of them are already mentioned. Rest of them are Subhankar, Srikrishna (Kesta), Gourab, Dr. Kabirul, Dr. Arindam, Sourav (SRV), Uday, Anirban, Soumen (Boss), Sumit, Karuna, Dr. Debasish (DK), Dr. Santa, Sayan (RC), Dr. Somnath.

Most importantly and especially, I owe a lot to my Kaka (Prabir Gangopadhyay) and Kakima (Shukla Ganguly). My career would not have been possible without their support and unconditional love. My Didi (Dunia) and Bon (Sharmishtha) for their love and having a memorable childhood.

Above all, I would like to thank my wife Mrinmayee for her love and constant support. You were always my support in the moments when there was no one to answer my queries. But most of all, thank you for being my best friend. I owe you everything.

Abstract

The thesis investigates the behaviour of conductance properties of spin-orbit coupled ballistic junction devices using the Landauer-Büttiker formalism and Green's function technique. The primary motivation is to explore spin Hall effect in these devices via computing the spin Hall conductance which assesses their utilities for spintronic applications. Two terminal, three terminal (Y-shaped) and four terminal structures are discussed extensively in the thesis. The step-like features in the longitudinal conductance, emphasizing discrete modes available for transport, and an oscillatory, coupled with an antisymmetry about the zero bias for the spin Hall conductance are the highlights of the transport characteristics. The inclusion of disorder destroys the former and suppresses the latter. Further, since conductance in graphene and graphene-based devices have been under focus in recent times for their non-trivial topological physics and possible spintronic properties, we have considered adatom decorated graphene nanoribbons described via Kane-Mele model. The quantum spin Hall (QSH) phase is shown to be robust in presence of heavy adatoms that are capable of inducing strong spin-orbit coupling. On the other hand, the Rashba spin-orbit interaction is seen to have detrimental effects on the QSH phase, which however has prospects in enhancing spintronic applications. Finally, an interplay between an external magnetic field and the Rashba spin-orbit coupling is explored for a six terminal graphene nanoribbon.

List of Publications

Publications in journals:

1. *Conductance properties of six terminal graphene nanoribbons in presence of a magnetic field : Integer quantum Hall effect revisited*,

   Sudin Ganguly and Saurabh Basu, Accepted to Journal of Electromagnetic Waves and Applications (Special Issue: The Current Trends of Graphene Technology).

2. *Spin Hall conductance in a Y-shaped junction device in presence of tunable spin-orbit coupling*,

   Sudin Ganguly and Saurabh Basu, Physica E **90**, 131 (2017).

3. *Interplay of Rashba spin orbit coupling and disorder in the conductance properties of a four terminal junction device*,

   Sudin Ganguly and Saurabh Basu, Eur. Phys. J. B **89**, 103 (2016).

4. *Anisotropic quantum transport in two dimension – hints of emergence of a metallic behaviour*,

   Sudin Ganguly and Saurabh Basu, Eur. Phys. J. B **88**, 96 (2015).

Paper submitted to journals:

5. *Adatoms in graphene nanoribbons: spintronic properties and the quantum spin Hall phase*,

   Sudin Ganguly and Saurabh Basu, paper submitted, arXiv:1704.06532v3 [cond-mat.mes-hall].

6. *Magnetic adatoms in two and four terminal graphene nanoribbons: A comparison between their spin polarized transport*,

   Sudin Ganguly and Saurabh Basu, Paper submitted, arXiv:1707.04098v1 [cond-mat.mes-hall].

Publications in conference proceedings:

1. *Spin Hall conductance in Y-shaped junction devices*,

   Sudin Ganguly and Saurabh Basu, Journal of Physics: Conference Series **807**, 082003 (2017).

2. *Spin dependent disorder in a junction device with spin orbit couplings*,

   Sudin Ganguly and Saurabh Basu, Journal of Physics: Conference Series **759**, 012028 (2016).

3. *Tunneling conductance through normal metal-superconductor junctions: effects of Rashba spin orbit coupling and magnetic field*,

   Priyadarshini Kapri, **Sudin Ganguly** and Saurabh Basu, Journal of Physics: Conference Series **759**, 012031 (2016).

4. *Magnetic versus Non-Magnetic Adatoms in Graphene Nanoribbons: Tuning of Spintronic Applications and the Quantum Spin Hall Phase*,

   Sudin Ganguly and Saurabh Basu, Paper submitted to 20th International Conference on Theoretical Physics and Quantum Technologies (2018).

Conference attended

Oral presentation

1. *Quantum conductance in a four-terminal junction device in presence of spin-orbit interaction and magnetic field*, Sudin Ganguly and Saurabh Basu, Xth National Conference of Physics Academy Of North-East (PANE) November 10-12, 2016 St. Anthony's College, Shillong, 793001, Meghalaya, India.

Poster presentation

2. *Spin dependent disorder in a junction device with spin orbit couplings*, Sudin Ganguly and Saurabh Basu, 58^{th} XXVII IUPAP Conference on Computational Physics: CCP2015 2 - 5 December 2015, IIT Guwahati, Assam, India.
3. *Effect of spin dependent disorder with different spin orbit interactions in four terminal device*, Sudin Ganguly and Saurabh Basu, Condensed Matter Days 2015 August 27-29, 2015 Department of Physics, Visva-Bharati, west Bengal, India.
4. *Adatoms in graphene nanoribbons : tuning of spin polarized conductance*, Sudin Ganguly and Saurabh Basu, Research Conclave'17, March 16-19, 2017, IIT Guwahati, Assam, India.

Contents

List of Figures

Chapter 1

Introduction

Mesoscopic physics is a relatively new branch of Condensed Matter physics. It deals with systems having dimensions that are intermediate between the microscopic (a few angstroms) and the macroscopic length (of an order of a micron) scale. A conductor of length L appears to be ohmic if $L \ll \lambda_{db}$ (λ_{db}: de Broglie wavelength), however, it is termed as non-ohmic or mesoscopic if $L \ll l_{\phi}$ (λ_{ϕ}: phase coherence length, over which the electrons retain phase coherence). This regime is governed by the Landauer formula for conductance[1], namely,

$$G = \left(\frac{e^2}{h}\right) T$$

where T is the probability of an electron to be transmitted through the conductor and has been summed over all the channels or modes. The constant, $\frac{e^2}{h} = \left[(25.8)k\Omega\right]^{-1}$ represents the quantum of conductance corresponding to a single transverse mode in a conductor.

Several typical characteristic length scales are briefly introduced to define and characterized different transport regimes[2–4]. They are:

(a) Fermi wavelength (λ_F): It is the de Broglie wavelength (λ_{db}) of the electrons near the Fermi energy.

(b) Mean free path (l_e): It is the distance that an electron travels before its initial momentum is destroyed, and describes the elastic scattering caused by the random impurity potential.

(c) Phase coherent length (L_{ϕ}): It is the distance that an electron travels before it looses its initial phase due to scattering from other electrons or lattice vibrations.

(d) Localization length ξ: It is an asymptotic property of the conductance as a function of the linear sample size and can be expressed by the relation, $G = G_0 e^{-2L/\xi}$, where G_0 is the conductance without the disorder.

In terms of the above length scales, one can define three distinct regimes for the mesoscopic transport. These are:

(1) Ballistic regime ($\lambda_{db} < L \ll l_e, l_\phi$): In this regime, the electrons propagate through the mesoscopic sample without any elastic or phase breaking scattering in the bulk. The scattering occurs at the contact region separating the leads and the conductor and the impurity scattering can be neglected.

(2) Diffusive regime ($\lambda_{db} \ll l_e \ll L < \xi$): In this regime, a few impurity atoms or a small concentration of disorder exist in the conducting sample and the electrons traverse coherently. Scattering is sample specific and one observes the full statistical fluctuations which are not suppressed by self-averaging.

(3) Insulating regime ($\xi < L$): It's also called localized regime in the presence of strong scattering limit where the interference can completely cease the transport inside the disordered mesoscopic conductor.

Many novel phenomena exist that are intrinsic to mesoscopic systems, such as the integer quantum Hall effect[5], where the Hall resistance is quantized in units of h/e^2, Aharonov-Bohm (AB) oscillations[6,7] in the conductance spectrum of mesoscopic rings with flux period h/e and "the dissipationless persistent currents" flowing in such systems in the normal (non-superconducting) resistive states etc. Since then, the attention to the physics governing mesoscopic transport has been growing rapidly, and a wide range of new physical concepts have been realized. Some of them are: mesoscopic resistors in series that do not obey standard resistance addition rules[2,8], the conductance of very narrow constrictions being quantized[9,10], the conductance of disordered systems shows sample specific reproducible fluctuations with universal amplitudes[11], the weak localization phenomena[12,13] etc.

Over the last two decades, it is possible to experimentally realize dimensions, $L < l_\phi$, using modern electronic material fabrication techniques, such as molecular beam epitaxy (MBE), lithography technique, scanning tunneling microscope (STM) etc[14–20]. They are denoted as nanostructures. Familiar examples are GaAs/GaAlAs semiconductor heterostructures, which are formed by two semiconducting samples with different doping levels. At the interface, a thin layer of charges, called a two-dimensional electron gas is realized (2DEG). These heterostructures yield mobilities of the order of $10^6 \text{cm}^2/(\text{V-s})$ that correspond to flow of electrons having a mean free path of about 10 μm. The numbers quoted here justify the onset of mesoscale transport phenomena which forms the central focus of the thesis.

A recent development in nanoscale technology is the exploitation of the spin degree of freedom, which popularly goes by the name, spintronics, where the spins of electrons carry the information. Compared to ordinary charge-based electronics, spin-based electronics offers opportunities for a new generation of devices. The advantages of these new devices are non-volatility, increased data processing speed, decreased electric power consumption and increased integration densities compared to the conventional semiconductor devices. The discovery of the giant magnetoresistive effect (GMR)[21,22] is considered the beginning of the study of this new spin-based electronics. The GMR effect denotes a large increase in resistance observed for a ferromagnet/metal/ferromagnet multilayer structure when the magnetization of the magnetic layers changes from being parallel to antiparallel. Important applications of the GMR effect are magnetic field sensors, read heads for hard drives, galvanic isolators and magnetoresistive random access memory (MRAM). Only ten years after its discovery, this effect has already found commercial applications in the form of read heads for hard drives and magnetic field sensors.

However, in order to realize spintronic devices, one has to generate a spin polarized current. In early attempts, the generation of spin-polarized currents was obtained by attaching ferromagnetic metallic contacts to the semiconductors[23–25]. But, the efficiency of the spin injection from a ferromagnet into a semiconductor does not meet expectations because of the conductivity mismatch between the two[26]. This drawback can be overcome by producing spin-polarized current intrinsically.

A strong spin-orbit scattering can generate spin-polarized electrons intrinsically[27]. In general, two types of spin-orbit coupling terms can be present in semiconductor heterostructures having two-dimensional electron systems (2DES). One of them is the Dresselhaus spin-orbit coupling (DSOC) which originates from the inversion asymmetry of the zinc blende type of structures[28]. The other is the Rashba spin-orbit coupling (RSOC) which originates due to the effective electric field originating from the asymmetry of the potential confining the systems in two dimensions[29]. The Dresselhaus term is found to be dominant in large bandgap materials and the strength can be controlled easily by tuning the quantum well width[30]. On the other hand, the Rashba term is dominant in narrow-gap systems where the strength of the Rashba term can be controlled by external gate voltages[31,32]. Since we are going to be interested in conductance properties of two-dimensional systems, RSOC will be important for most of our studies. However, Dresselhaus SOC has also been briefly discussed in the thesis, especially with regard to its interplay with the RSOC.

The strength of the spin-orbit interactions are sensitive to electric fields, enabling one to control the electron spin electrically, without the need to use any magnetic agent, such as a magnetic field. A large number of devices have been proposed based on spin-orbit interactions, for example, the spin field effect transistor[33], and several spin interference based devices (see Refs. [34,35]).

Just as the magnetic field creates a charge segregation thereby producing a Hall voltage in a 2DEG, the spin-orbit coupling can facilitate opposite spins to move across edges of the sample, producing a spin version of the Hall effect, generally referred to as the spin Hall effect. The discovery of spin Hall effect is one of the celebrated discovery in this field, in which a longitudinal unpolarized charge current can induce a transverse pure spin current due to spin-orbit interactions[36–38]. A quantum version of the spin Hall effect, denoted as the quantum spin Hall (QSH) effect has earned its reputation for having nontrivial topological properties. QSH effect is perceived as two copies of the quantum Hall system, one for each species of the spin. The QSH phase is usually identified by the presence of a plateau of finite value ($= 2e^2/h$) at and around the zero bias.

In two-dimensional systems, owing to its surface inversion asymmetry, RSOC is found to have large values and hence produces non-ignorable effects in quantum transport. Graphene was believed to be an excellent playground for testing known theories of quantum transport. It is useful to have an a priori mention of the prospects of a nontrivial topological phase lying therein. However, the existence of such phases is understood to be beyond the experimental accuracy for modern day measuring devices.

The successful fabrication of graphene[39] has attracted a wide attention over more than a decade owing to its several interesting electronic and transport properties[39–45]. Quantum Hall effect[39,41,42], half-metallicity[43,44], high carrier mobility[45] remarkable elastic properties etc. are the interesting features that make graphene, among many other technological usages, as promising candidate for nanoelectronics and spintronic applications. The recent realization of freestanding graphene nanoribbons (GNRs)[46,47] has generated renewed interest in carbon-based materials with exotic properties.

GNRs are basically a single strip of graphene. The electronic properties of GNRs depend on the geometry of the edges and the lateral width of the nanoribbons[48], and according to the edge termination type, mainly there are two kinds of GNRs, namely, the armchair graphene nanoribbon (AGNR) and the zigzag graphene nanoribbon (ZGNR). The ZGNRs are always metallic with zero bandgaps, while the AGNRs are conditionally metallic that is, when the lateral width, $N = 3M - 1$ (M is an integer) it is metallic, else they are semiconducting in nature[49] with a finite band gap.

Apart from the spintronic application point of view, there was a fundamental interest that guided the field of research ahead. The interest is to search for a new topological state other than the one obtained in the context of QHE. C. L. Kane and E. J. Mele[50,51] predicted that quantum spin Hall (QSH) state which may be perceived as a new topological state can be observed in presence of intrinsic spin-orbit coupling (SOC) in graphene, which triggered an enormous study on topologically nontrivial electronic materials[52–55]. Kane and Mele wrote down a Hamiltonian that respects all the symmetries, such as space inversion, time reversal, Kramer's degeneracy etc. and predicted the existence of (chiral) metallic edge states along with an insulating bulk. The edge states conduct, rendering 'metallic' properties of the topological 'insulators' thereby implying the existence of a QSH phase. However, as said earlier, the QSH effect in clean graphene is still not observed experimentally owing to its vanishingly small intrinsic spin-orbit coupling (SOC) strength[56,57], whereas in strained semiconductors, such as CdTe/HgTe quantum wells, the QSH effect has been experimentally observed[58].

It was theoretically proposed that adsorption of adatoms such as Indium (In), Thallium (Tl), Gold (Au) etc. can enhance or induce the intrinsic SOC and the Rashba SOC in graphene[59–61]. While the intrinsic SOC is indispensable for realizing the predicted QSH effect, Rashba SOC is found to be detrimental to it. Specifically, adatoms such as In or Tl can open up a significant topologically nontrivial gap implying inducing of predominantly the intrinsic SOC that lead to the stabilization of the QSH phase. Different theoretical studies have confirmed that the two systems (that is In and Tl decorated GNRs) are indeed stable two-dimensional topological insulators[59,61,62]. On the other hand, Au-like adatoms induce Rashba SOC which dominates over the intrinsic SOC and the QSH effect will likely to lose in the competition. Therefore it will be relevant to study the transport properties in Au adatom decorated graphene to assess the interplay of intrinsic SOC and RSOC and illustrate the validity of the above scenario. Moreover, owing to the presence of Rashba SOC induced by Au adatoms, features of the spin polarized conductance may provide additional clues on the topological phase and spintronic applications.

Among the metal adatoms, the study of GNRs in presence of transition metals (TM) warrants some special attention since TM serve as important catalysts for the synthesis of graphite, CNT, GNR etc. Since TM catalysts (particularly Fe) is a common impurity in the graphite[63], graphene layers fabricated from graphite are likely to have these impurities. Longo et al.[64] have shown that the behaviour of Fe atoms in a GNR renders a magnetic character, in contrast with the behavior found in graphene[65,66] which itself is non-magnetic. Mao et al.[67] showed that adsorption of Fe on graphene makes graphene metallic and generates 100% spin polarization. Basically the study of TM adsorption on graphene[68,69] shows possible applications in the realization of graphene-based electronic and spintronic devices. Another important point that should be noted here is that the adsorption of TM onto GNR gives rise to a Rashba spin-orbit interaction coupling and the hybridization between the carbon π-state and the $3d$-shell states of magnetic adatoms generates a macroscopic exchange field[70], which in turn breaks the time reversal symmetry (TRS) a feature otherwise present in the Kane-Mele model (relevant to non-magnetic adatoms, like Au etc.), where the TRS is preserved.

Motivated by the above discussion, we aim to study several interesting features concerning the charge and spin transport properties of junction devices, including GNRs via Landauer-Büttiker formalism. As we shall see in the subsequent discussion, the fundamental physics associated with quantum transport and the QSH phase will be as important as the spin polarized transport that is central to spintronic applications.

In the upcoming sections, we briefly introduce the two kinds of spin-orbit coupling (SOC), namely Dresselhaus and Rashba SOC, a general introduction to the graphene nanoribbons.

1.1 Spin-orbit interaction

When an electron with momentum $\mathbf{p}$ moves in a magnetic field $\mathbf{B}$, it experiences a Lorentz force in the direction perpendicular to its motion $\mathbf{F} = -e\mathbf{p} \times \mathbf{B}/m$ and possesses Zeeman energy $\mu_B \boldsymbol{\sigma} \cdot \mathbf{B}$, where $\boldsymbol{\sigma}$ is the vector of the Pauli spin matrices and $\mu_B = 9.27 \times 10^{-24}$ JT^{-1} is the Bohr magneton. According to the theory of special relativity, the electric and the magnetic fields undergo a Lorentz transformation as one goes from one inertial frame of reference to another. Thus for a charged particle moving through an electric field, it starts to experience some magnetic field in its own inertial frame of reference. A key example of this effect is the spin-orbit interaction in atomic systems. There the strong electric field of the atoms couples to the spin of the electrons, resulting in a Zeeman type splitting of the atomic spectral lines[71].

The Hamiltonian describing this type of spin-orbit interaction can be written as,

$$H_{SO} = -\frac{\hbar}{4m_e^2c^2}\boldsymbol{\sigma} \cdot \mathbf{p} \times (\boldsymbol{\nabla} V_0) \tag{1.1}$$

where, c is the velocity of light, $\mathbf{p}$ is the linear momentum and V_0 is an electric potential. The term H_{SO} is known as the Pauli spin-orbit term and can be derived by taking the non-relativistic limit of the Dirac equation[72]. In crystals we can approximate the potential originating from the atomic cores as being radial close to the cores, that is, $V_O \sim 1/r$. With this approximation we can write the Pauli spin-orbit term as,

$$H_{SO} \sim \mathbf{L} \cdot \mathbf{S} \tag{1.2}$$

where $\mathbf{L} = \mathbf{p} \times \mathbf{r}$ is the orbital angular momentum operator and $\mathbf{S} = \frac{\hbar}{2}\boldsymbol{\sigma}$ is the spin operator.

The crystal potential produces a spin-orbit field of the from, $\mathbf{w}(\mathbf{p}) \sim \boldsymbol{\nabla} V_O \times \mathbf{p}$. Since the spin-orbit coupling preserves the time reversal symmetry denoted by, $\mathbf{w}(\mathbf{p}) \cdot \sigma = -\mathbf{w}(-\mathbf{p}) \cdot \sigma$, the spin-orbit field must be odd in the electron momentum $\mathbf{p}$; that is $\mathbf{w}(-\mathbf{p}) \cdot \sigma = -\mathbf{w}(\mathbf{p})$[73]. This odd-in-$\mathbf{p}$ SO field only survives in systems that lack spatial inversion symmetry.

1.1.1 Dresselhaus spin-orbit interaction

Dresselhaus had noted that in the zinc-blende III-V semiconductor compounds lacking a center of inversion, such as GaAs, InSb etc., the SO coupling close to Γ point takes the form,

$$H_{D_3} = (\gamma/\hbar)\left[\left(p_y^2 - p_z^2\right)p_x\sigma_x + \left(p_z^2 - p_x^2\right)p_y\sigma_y\left(p_x^2 - p_y^2\right)p_z\sigma_z\right] \tag{1.3}$$

The addition symmetry considerations in the band structure results in additional odd-in-$\mathbf{p}$ SO coupling terms[74]. For 2DEG structures grown in the (001) crystal direction, the cubic Dresselhaus SO term given in Eq.(1.3) reduces to the linear Dresselhaaus SO term of the form[75],

$$H_{D_1} = (\beta/\hbar)\left(p_x\sigma_x - p_y\sigma_y\right) \tag{1.4}$$

where $\beta = \gamma p_z^2$ and it depends on the material band parameters and the thickness of the 2DEG.

1.1.2 Rashba spin-orbit interaction

When the motion of electrons is confined to two dimensions, for example in quantum wells, an asymmetric confinement potential becomes another source for SOC. The importance of this mechanism lies in the fact that asymmetry in the confinement potential can be varied by electrostatic means, allowing one to tune the SOC strength by an external gate voltage. This type of SOC is known as Rashba SOC[29]. The strength of RSOC depends also on the crystal composition in the quantum well, and is largest for narrow gap III-V semiconductors, such as InAs and InGaAs.

In the following subsections, we shall give brief descriptions to the Rashba SOC in the continuum model as well as in the lattice model. We have often used Rashba SOC or RSOC interchangeably for the Rashba spin-orbit coupling.

Let us discuss it in the context of a continuum model, in which case, the RSOC is described by the following Hamiltonian[29],

$$H_R = \alpha\left(\mathbf{p}\times\boldsymbol{\sigma}\right)\cdot\hat{z} \tag{1.5}$$

where $\mathbf{p} = -i\hbar\boldsymbol{\nabla}$ is the momentum operator, and $\boldsymbol{\sigma} = (\hat{\sigma_x}, \hat{\sigma_y}, \hat{\sigma_z})$ denote Pauli spin matrices. α is the strength of the SOC. In the absence of the Zeeman coupling and elastic scattering, the total Hamiltonian for the electrons is given by

$$H = \frac{\mathbf{p}^2}{2m} + \alpha\left(\mathbf{p}\times\boldsymbol{\sigma}\right)\cdot\hat{z} \;=\; \frac{p_x^2+p_y^2}{2m} + \alpha\left(\hat{\sigma_x}p_y - \hat{\sigma_y}p_x\right) \tag{1.6}$$

Diagonalizing this Hamiltonian yields the following energy spectrum[76],

$$E\left(\mathbf{k}\right) = \frac{\hbar^2\mathbf{k}^2}{2m} \pm \alpha|\mathbf{k}| \tag{1.7}$$

where $|\mathbf{k}| = \sqrt{k_x^2+k_y^2}$ is the modulus of the electron momentum and the plus and minus signs correspond to the two possible spin orientations. The eigenvectors of the Hamiltonian (Eq.(1.6)) relative to the spectrum (Eq.(1.7)) are plane wave functions of momentum $\mathbf{k}$ and they are given by,

$$\Psi_{\pm}\left(x,y\right) = \mathrm{e}^{\mathrm{i}(k_x x + k_y y)}\frac{1}{\sqrt{2}}\begin{pmatrix}1\\ \pm\mathrm{i}\end{pmatrix}\mathrm{e}^{-\mathrm{i}\theta} \tag{1.8}$$

where $\theta = \tan^{-1}\left(\frac{k_y}{k_x}\right)$. It is important to note that the spin states (Eq.(1.8)) are always perpendicular to the direction of motion. In fact, if an electron moves along

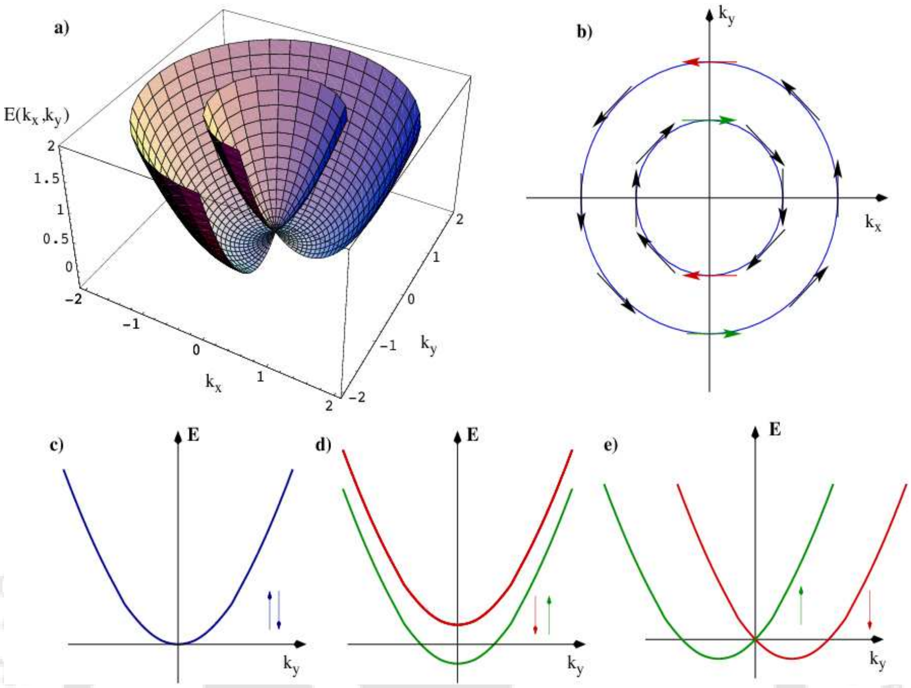

Figure 1.1: Single particle energy spectrum is shown in presence of Rashba spin-orbit coupling. (a) Three-dimensional view of the energy spectrum. (b) The Fermi energy contours with the spin states are indicated. (c) Energy spectrum for a free electron showing degeneracy of up and down spins. (d) Energy spectrum for an electron in presence of a magnetic field (Zeeman splitting). (e) Energy spectrum for an electron in presence of Rashba spin-orbit interaction. Courtesy of Ref. [77].

x-direction, the spinor part of the eigenvector is $\begin{pmatrix} 1 \\ \pm i \end{pmatrix}$, which denotes the spin up and spin down in the y-direction. On the contrary if the electron moves along the y-direction, the eigenvector is $\begin{pmatrix} 1 \\ \pm 1 \end{pmatrix}$, which represents spin up and spin down state in the x-direction (see Fig. 1.1).

In Fig.1.1(c-e) the energy spectra are plotted as a function of k_y for different physical situations as explained in the following. Fig.1.1(c) is related to a free electron of a 2DEG. In this case, the spin degeneracy is present. In presence of a magnetic field $\vec{B}$ (Fig.1.1(d)), the spin degeneracy is lifted upon by the Zeeman splitting and the gap separating spin up and spin down is equal to $g\mu_B B$ where g is the Bohr magneton. When the Rashba SOC is present (Fig.1.1(e)), the spin degeneracy is lifted up but only for $\vec{k} = 0$. In this situation, the degeneracy is removed without opening of gaps.

Similar calculations as above can be carried on to a discrete system that is a lattice model. In order to perform numerical calculations on a lattice, we have to discretize the Hamiltonian (Eq.(1.6)). For this, we adopted a discretization scheme[78] for the Rashba Hamiltonian which is elaborately discussed in the next section.

By following the general discretization method as discussed in the next section, the Rashba Hamiltonian in the local orbital basis representation with tight binding approximation becomes,

$$H = \sum_{i\sigma} \epsilon_i c^{\dagger}_{i\sigma} c_{i\sigma} + \sum_{ij\sigma\sigma'} c^{\dagger}_{i\sigma} t^{\sigma\sigma'}_{ij} c_{j\sigma'} \tag{1.9}$$

where ϵ_i is the on-site energy, $c^{\dagger}_{i\sigma}$ ($c_{i\sigma}$) is the creation (annihilation) operator of an electron at the i-th lattice site with spin σ. $t^{\sigma\sigma'}_{ij}$ are the generalized hopping parameters, which are actually a 2×2 Hermitian matrices. The generalized nearest neighbor hopping $t^{\sigma\sigma'}_{ij} = (t_{ij})_{\sigma\sigma'}$ accounts for the Rashba coupling.

$$t_{ij} = \begin{cases} -t_O I - i t_{SO} \hat{\sigma_y} & (\mathbf{m} = \mathbf{m} + \mathbf{e}_x) \\ -t_O I + i t_{SO} \hat{\sigma_x} & (\mathbf{m} = \mathbf{m} + \mathbf{e}_y) \end{cases} \tag{1.10}$$

where $t_O = \frac{\hbar^2}{2ma^2}$ is the orbital hopping term, $t_{SO} = \frac{\alpha}{2a}$ is the Rashba SO hopping term. the physical meaning of both of the hopping terms are illustrated in Fig.1.2.

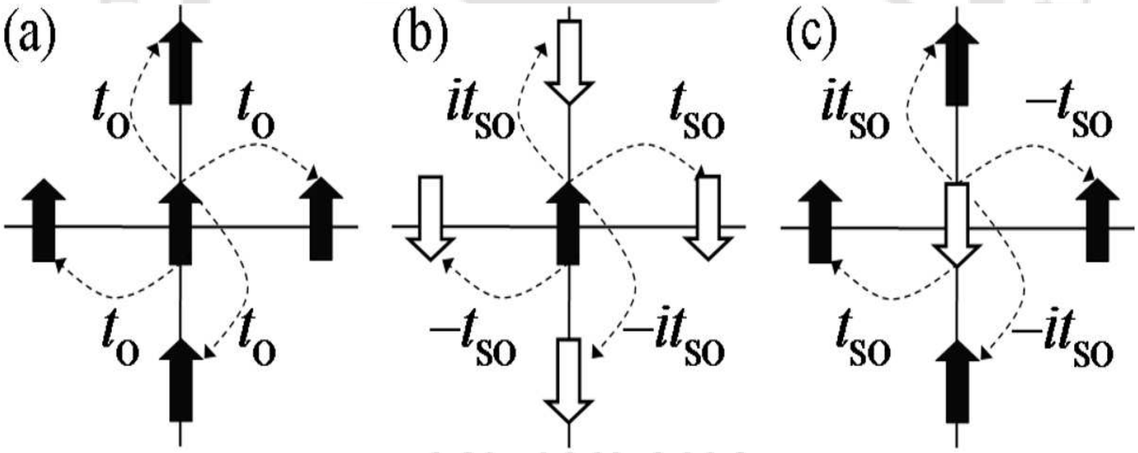

Figure 1.2: (a) The probability amplitude for a spin to hop among any of its nearest neighbor without flipping is proportional to t_O, which is spin independent. (b), (c) The probability of the central electron to flip its spin by hopping among any of its nearest neighbor is proportional to t_{SO}. Courtesy of Ref. [78].

The Rashba Hamiltonian (Eq.(1.9)) is not separable in most situations, especially if there is a confining potential. However, without that, it is possible to diagonalize and solve for the Hamiltonian in 1D and 2D exactly. With a tight binding approximation, the eigenvalues and the eigenvectors for the Hamiltonian (Eq.(1.9)) for the

2D case are,

$$E_{\mathbf{k},\pm} = 2t_O\left(\cos k_x a + \cos k_y a\right) \pm 2t_{SO}\sqrt{\sin^2 k_x a + \sin^2 k_y a} \tag{1.11}$$

$$\Psi_{\mathbf{k},\pm} = \frac{\mathrm{e}^{i\mathbf{k}\cdot(x\hat{x}+y\hat{y})}}{\sqrt{2L_xL_y}}\begin{pmatrix} \pm\frac{\sin k_y a + i\sin k_x a}{\sqrt{\sin^2 k_x a+\sin^2 k_y a}} \\ 1 \end{pmatrix} \tag{1.12}$$

where L_x and L_y are the dimensions of the lattice along x and y axis respectively, the plus sign stands for the up spin and minus for the down spin.

1.2 Discretization scheme for the Hamiltonian

For finite sized systems, it is advantageous to discretize the Rashba Hamiltonian. Say we do it on a square lattice of sides a with $\mathbf{m} = (m_x, m_y)$, collections of points on a square lattice. m_x and m_y are integers. Thus, $\Psi_{\mathbf{m}} = \langle \mathbf{m}|\psi\rangle$ i.e. the representation of the function Ψ in real space, and the matrix element of an operator is defined as $\langle \mathbf{m}|A|\mathbf{m}'\rangle = A_{\mathbf{m}\mathbf{m}'}$.

In finite difference methods, the derivative of a function $f(x)$ on a 1D grid $\{..., x_{m-1}, x_m, x_{m+1}, ...\}$ ($\equiv \{..., (m-1)a, ma, (m+1)a, ...\}$) is evaluated as,

$$\left(\frac{df}{dx}\right)_m = \frac{f_{m+1} - f_{m-1}}{2a} \tag{1.13}$$

where $f_m = f\left(x_m\right)$. Similarly the second derivative is computed as,

$$\left(\frac{d^2f}{dx^2}\right)_m = \frac{f_{m+1} - 2f_m + f_{m-1}}{a^2} \tag{1.14}$$

Thus the matrix elements of the derivative operator, $\frac{d}{dx}$ is written as,

$$\begin{aligned}\left\langle m\left|\frac{d}{dx}\right|n\right\rangle &= \frac{\langle m+1\,|\,n\rangle - \langle m-1\,|\,n\rangle}{2a} \\ &= \frac{\delta_{n,m+1} - \delta_{n,m-1}}{2a} \end{aligned} \tag{1.15}$$

Similarly for a double derivative,

$$\left\langle m\left|\frac{d^2}{dx^2}\right|n\right\rangle = \frac{\delta_{n,m+1} - 2\delta_{n,m} + \delta_{n,m-1}}{a^2} \tag{1.16}$$

It is important to note that the matrix elements depend upon the discretization scheme. If $\frac{d^2}{dx^2}$ is interpreted as, $\frac{d}{dx}\cdot\frac{d}{dx}$ then the result obtained will be different than the alone scheme.

In the second quantized notation, the operator in terms of its matrix element is,

$$\hat{A} = \sum_{m,n} \langle m \,|\, n\rangle\, c^\dagger_m c_n \tag{1.17}$$

using this definition,

$$\frac{d}{dx} = \sum_m \frac{1}{2a}\left(c^\dagger_m c_{m+1} - c^\dagger_m c_{m-1}\right) \tag{1.18}$$

and

$$\frac{d^2}{dx^2} = \sum_m \frac{1}{a^2}\left(c^\dagger_m c_{m+1} - 2c^\dagger_m c_m + c^\dagger_m c_{m-1}\right) \tag{1.19}$$

Thus for a free Hamiltonian $H = H_0 = \frac{\mathbf{p}^2}{2m} = -\frac{\hbar^2}{2m}\left(\frac{d^2}{dx^2} + \frac{d^2}{dy^2} + ...\right)$ is written as,

$$\begin{aligned} H_0 &= 4\frac{\hbar^2}{2ma^2}\sum_m c^\dagger_m c_m - \frac{\hbar^2}{2ma^2}\sum_{m,n} c^\dagger_m c_n \\ &= \epsilon \sum_m c^\dagger_m c_m - t\sum_{m,n} c^\dagger_m c_n \end{aligned} \tag{1.20}$$

with $\epsilon = 4\frac{\hbar^2}{2ma^2}$ and $t = \frac{\hbar^2}{2ma^2}$. The term ϵ is called the onsite term and t is the hopping amplitude.

By following the above discretization scheme, it is straight forward to discretize the Rashba Hamiltonian (Eq.(1.6)), namely,

$$\begin{aligned} H_{sq} &= \sum_{i,\sigma} \epsilon_i c^\dagger_{i\sigma} c_{i\sigma} + t\sum_{\langle ij\rangle,\sigma} c^\dagger_{i\sigma} c_{j\sigma} \\ &+ \alpha \sum_i \left[\left(c^\dagger_{i\uparrow} c_{i+\delta_x\downarrow} - c^\dagger_{i\downarrow} c_{i+\delta_x\uparrow}\right) - i\left(c^\dagger_{i\uparrow} c_{i+\delta_y\downarrow} + c^\dagger_{i\downarrow} c_{i+\delta_y\uparrow}\right)\right] \end{aligned} \tag{1.21}$$

The above equation is derived on a 2D square lattice and will be discussed later (see Eq.(3.6)).

1.3 Junction devices

The geometry and the number of attached leads to the scattering region play an important role in quantum transport. For example, in case of a two terminal system, one can calculate or observe the charge conductance or the spin polarized conductance. However spin Hall effect cannot be studied in a two-terminal device. Since spin-orbit interactions play an important role in this thesis, the spin Hall effect becomes an indispensable study in this regard. Thus in order to observe the spin Hall effect, one needs to resort to multi-terminal devices, such as a four terminal or a six terminal etc. in this section, we shall briefly describe different kinds of multi-terminal devices that are relevant to our thesis.

(i) Two terminal (2T): In 2T setup, a conductor is sandwiched between two contacts. These two contacts have different values of the chemical potential and as a result, current will flow between the two leads. One can measure the charge conductance or the spin polarized conductance as we shall show in Chapter 5 and Chapter 6.

(ii) Four terminal (4T): The four terminal or the cross-shaped junction device is suitable for observing the spin Hall effect and is easy to visualize. In 4T devices, a current is allowed to flow along the longitudinal direction. The transverse leads are voltage probes and hence no charge current flows through them. A spin current can be observed at the transverse leads and hence one can measure the spin Hall conductance. In Chapter 3 we shall show the calculations related to the spin Hall conductance.

(iii) Three terminal (3T): Examples of 3T setup are the Y-shaped or T-shaped devices[79–81]. A charge current is allowed to flow through the main branch of the Y or T shaped devices. One of the arms acts as a voltage probe. Spin Hall effect can be observed between the two arms of the Y or T shaped devices. In Chapter 4 we shall show that the results for spin Hall conductance for Y-shaped devices.

(iv) Six terminal (6T): The six-terminal setup is a standard setup for measuring the Hall resistance[82]. However, one can observe the spin Hall effect as well in case of a 6T device. The 6T Hall bar contains two current electrodes at the ends of the Hall bar, with four potential electrodes along the side of the bar to allow longitudinal and transverse (Hall) voltages measurements. In chapter 7 we shall discuss the 6T setup where we have studied the quantum (charge) Hall and the spin Hall effect.

1.4 Basics of Graphene

Graphene is a one-atom-thick planar sheet of sp^2-bonded carbon atoms densely packed in a honeycomb crystal lattice. Graphene was first experimentally realized only a decade ago by Novoselov et al.[39]. It has attracted a wide attention to be used as a next generation electronic material, due to its exceptional properties including high current density, ballistic transport, chemical inertness, high thermal conductivity, optical transmittance and super hydrophobicity at nanometer scale[83,84].

Carbon has four valence electrons, three of them form tight bonds with the neighbouring atoms in the plane. Their wave functions have the form,

$$\frac{1}{\sqrt{3}}\left(\psi\left(2s\right)+\sqrt{2}\psi\left(\tau_i 2p\right)\right), \qquad (i=1,2,3) \tag{1.22}$$

where $\psi(2s)$ is the $2s$ wave function and $\psi(\tau_i 2p)$ are the $2p$ wave functions of which the axes are in the directions τ_i joining the carbon atom to its three neighbours in the plane. The fourth electron is in the $2p_z$ state. Its nodal plane is the lattice plane and its axis of symmetry perpendicular to it. Since the three electrons forming coplanar bonds do not play any role in its conducting properties, graphene can be considered to have one conduction electron per carbon atom in the $2p_z$ state.

1.4.1 Crystal structure

The carbon atoms in graphene form in a honeycomb lattice due to their sp^2 hybridization. The honeycomb lattice is not a Bravais lattice because two neighbouring sites are not equivalent. Fig.1.3 illustrates that a site on the A sublattice has nearest neighbours (nn) in the directions east, south-west and north-west which belong to the B sublattice, whereas a site on the B sublattice has nn in the directions west, north-east, and south-east which belong to the A sublattice. Both A and B sublattices, however, are triangular Bravais lattices, and one may view the honeycomb lattice as a triangular Bravais lattice with a two-atom basis (A and B). The distance between nn carbon atoms is 1.42 Å,

The primitive lattice vectors of graphene can be written as (Fig.1.3(a)),

$$\mathbf{a}_1=\frac{3a}{2}\left(\hat{x}+\frac{1}{\sqrt{3}}\hat{y}\right); \qquad \mathbf{a}_2=\frac{3a}{2}\left(\hat{x}-\frac{1}{\sqrt{3}}\hat{y}\right) \tag{1.23}$$

where $a=1.42$Å. The reciprocal lattice vectors (Fig.1.3(b)) are given by,

$$\mathbf{b}_1=\frac{2\pi}{3a}\left(\hat{x}+\sqrt{3}\hat{y}\right); \qquad \mathbf{b}_2=\frac{2\pi}{3a}\left(\hat{x}-\sqrt{3}\hat{y}\right) \tag{1.24}$$

The three nearest neighbour vectors in real space are given by,

$$\boldsymbol{\delta}_1=\frac{a}{2}\left(\hat{x}+\sqrt{3}\hat{y}\right); \quad \boldsymbol{\delta}_2=\frac{a}{2}\left(\hat{x}-\sqrt{3}\hat{y}\right); \quad \boldsymbol{\delta}_3=a\hat{x} \tag{1.25}$$

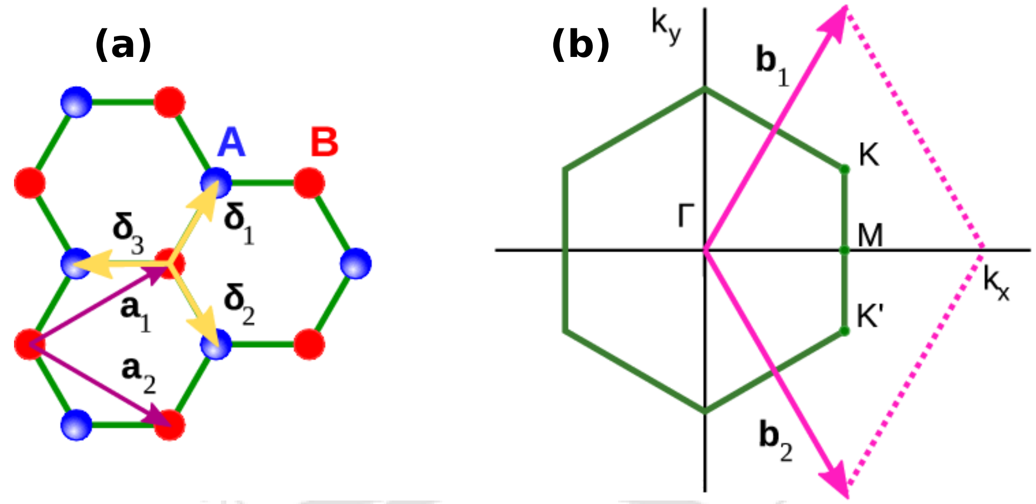

Figure 1.3: (a) Honeycomb lattice structure of graphene. The vectors $\boldsymbol{\delta}_1$, $\boldsymbol{\delta}_2$ and $\boldsymbol{\delta}_3$ connect nn carbon atoms separated by a distance $a = 1.42$ Å. The vectors $\mathbf{a}_1$ and $\mathbf{a}_2$ are the basis vectors. (b) First Brillouin zone (BZ) of the honeycomb lattice. Its primitive lattice vectors are $\mathbf{b}_1$ and $\mathbf{b}_2$. The Dirac points, K and K' are situated at the corners of the BZ.

The positions of the two (non-equivalent) Dirac points K and K', located at the corners of the Brillouin zone (as shown in Fig.1.3(b)) are,

$$\mathbf{K} = \frac{2\pi}{3a}\left(\hat{x} + \frac{1}{\sqrt{3}}\hat{y}\right); \qquad \mathbf{K}' = \frac{2\pi}{3a}\left(\hat{x} - \frac{1}{\sqrt{3}}\hat{y}\right) \tag{1.26}$$

1.4.2 Tight-binding approximation

It was Wallace[85] who developed the tight-binding method for 2D graphite long back. Because the spacing of the lattice planes of graphite is large (3.37Å), compared to the hexagonal spacing of the layer (1.42Å), the interactions among the planes was neglected and it was assumed that conduction takes place in the layers. This is precisely the scenario with graphene.

For the electronic band structure of graphene, we consider a tight binding model with nearest neighbour interaction only. The relevant atomic orbital is the single ($p\sigma$) (or more precisely π) C orbital which is left unfilled by the bonding electrons, and which is oriented normal to the plane of the lattice. This orbital can accommodate two electrons with spin projection ± 1. If we denote the orbital on atom i with spin σ by (i, σ), and the corresponding creation operator by $a^{\dagger}_{i\sigma}(b^{\dagger}_{i\sigma})$ for an atom on the A(B) sublattice, then the nearest neighbour tight binding Hamiltonian has the form,

$$H = -t \sum_{\langle ij \rangle,\sigma} \left(a^{\dagger}_{i\sigma} b^{\dagger}_{j\sigma} + H.c. \right) \tag{1.27}$$

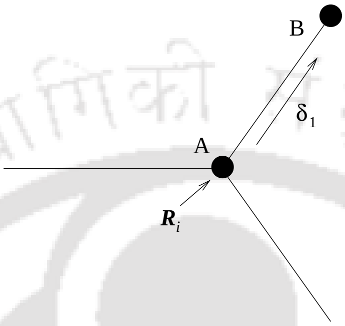

Figure 1.4: Convention for choosing the reference frame for A and B sublattice in graphene. $\boldsymbol{\delta}_1$ connects A to B.

It is convenient to write the tight binding eigenfunctions in the form of a spinor, whose components correspond to the amplitudes on the A and B atoms respectively within the unit cell labeled by a reference point $\mathbf{R}^0_i$. It is a matter of convention how we choose the pair A and B and the point $\mathbf{R}^0_i$, but for definiteness, let us choose B to be separated from A by $\boldsymbol{\delta}_1$ and $\mathbf{R}^0_i$ at the position of A as shown in Fig.1.4. Then the tight binding eigenfunctions have the form (apart from the spin index)

$$\begin{pmatrix} \alpha_{\mathbf{k}} \\ \beta_{\mathbf{k}} \end{pmatrix} = \sum_i e^{i\mathbf{k}\cdot\mathbf{R}^0_i} \begin{pmatrix} a^{\dagger}_i e^{-i\mathbf{k}\cdot\boldsymbol{\delta}_1/2} \\ b^{\dagger}_i e^{i\mathbf{k}\cdot\boldsymbol{\delta}_1/2} \end{pmatrix} \tag{1.28}$$

where $b^{\dagger}_i$ creates an electron on the B atom in cell i. The factor $e^{\pm i\mathbf{k}\cdot\boldsymbol{\delta}/2}$ are the spinor components that are inserted in order to simplify subsequent expressions. The Resulting Hamiltonian in the **k**-representation is purely off-diagonal and has the form,

$$H_{\mathbf{k}} = \begin{pmatrix} 0 & \Delta_{\mathbf{k}} \\ \Delta^*_{\mathbf{k}} & 0 \end{pmatrix}; \qquad \Delta_{\mathbf{k}} = -t \sum_{l=1}^{3} e^{i\mathbf{k}\cdot\boldsymbol{\delta}_l} \tag{1.29}$$

From the explicit expressions for the nearest neighbour vectors $\boldsymbol{\delta}_l$ as given in Eq.(1.25), we obtain,

$$\Delta_{\mathbf{k}} = -te^{ik_xa} \left(1 + 2e^{i\cdot\frac{3k_xa}{2}} \cos\frac{\sqrt{3}}{2}k_ya \right) \tag{1.30}$$

Finally the eigenvalues of H, $\epsilon_{\mathbf{k}}$ are given by,

$$\epsilon_{\mathbf{k}} = \pm\Delta_{\mathbf{k}} = \pm t\left(1 + 4\cos\frac{3k_xa}{2}\cos\frac{\sqrt{3}k_ya}{2} + 4\cos^2\frac{\sqrt{3}k_ya}{2}\right)^{\frac{1}{2}} \tag{1.31}$$

There are certain values of $\mathbf{k}$ for which $\Delta_{\mathbf{k}}$ is zero. Any such value must satisfy the condition,

$$\begin{aligned} \frac{3k_xa}{2} &= 2n\pi, \qquad \cos\frac{\sqrt{3}}{2}k_ya = -\frac{1}{2} \qquad (n \text{ integral}) \qquad (1.32)\\ \text{or} \quad \frac{3k_xa}{2} &= (2n+1)\pi, \qquad \cos\frac{\sqrt{3}}{2}k_ya = +\frac{1}{2} \end{aligned}$$

The first choice takes k_y outside the first Brillouin zone. while the second (with $n = 0$) is satisfied exactly at the corner points $\mathbf{K}$ and $\mathbf{K}'$. These points are called the Dirac points. The characteristic shape of the resulting band structure is displayed in Fig.1.5

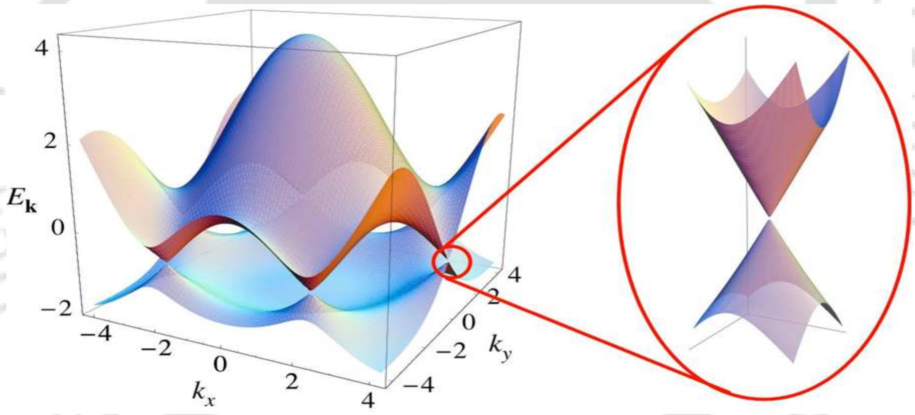

Figure 1.5: Electronic band structure of graphene. Left: energy spectrum (in units of t). Right: enlarged view of the energy bands close to one of the Dirac points. Courtesy of Ref. [40].

1.5 Graphene Nanoribbon

Graphene nanoribbons are elongated strips of graphene which can be obtained by cutting a graphene sheet along a certain direction. Depending on the edge termination type, there are two types of graphene, namely Armchair graphene nanoribbon (AGNR) and Zigzag graphene nanoribbon (ZGNR) as shown in Fig.1.6. Along the double arrow headed straight line, as shown in Fig.1.6, the GNR strips have periodic shapes. In the left figure, the GNR setup has an armchair shape, hence it denotes by AGNR and the right one has a zigzag shape, thus it is called as ZGNR. It should also be noted that the width of the AGNR has a zigzag shape and likewise, a ZGNR has an armchair shape.

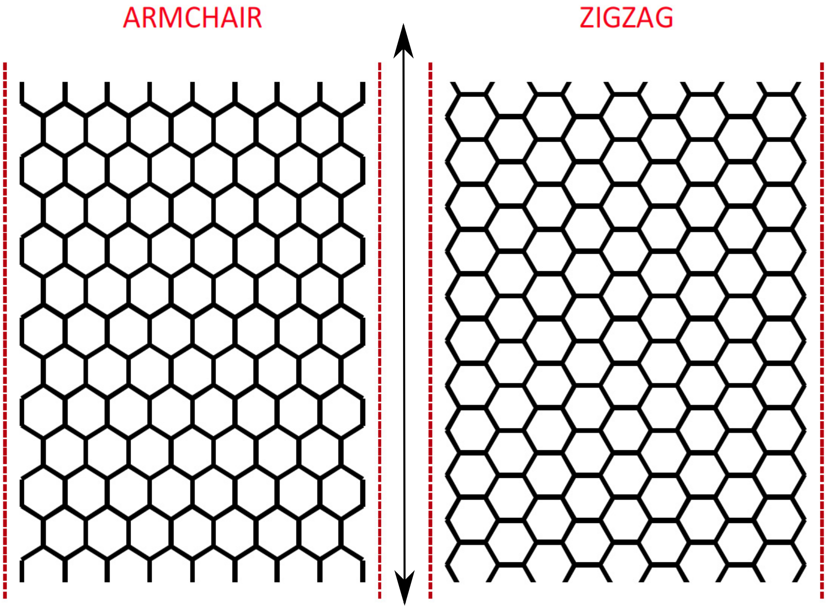

Figure 1.6: Left: Armchair graphene nanoribbon (AGNR). Right: Zigzag graphene nanoribbon (ZGNR) along the directions indicated in the figure by the line with double headed arrow.

The electronic properties of GNRs depend on the geometry of the edges and lateral width of the nanoribbons. Wakabayashi et al.[49] examined analytically that the ZGNRs are always metallic, but the conducting state of the direct energy gap (Δ_a) for AGNRs depend on their width and follow the relation,

$$\Delta_a \sim \begin{cases} 0 & N = 3M-1 \\ -\frac{\pi}{W+\frac{\sqrt{3}}{2}} & N = 3M \\ \frac{\pi}{W} & N = 3M+1 \end{cases} \tag{1.33}$$

where, W is the width of the AGNR and M is an integer. Hence according to Eq.(1.33), AGNRs are always metallic when their width is $N = 3M - 1$, else they are semiconducting in nature.

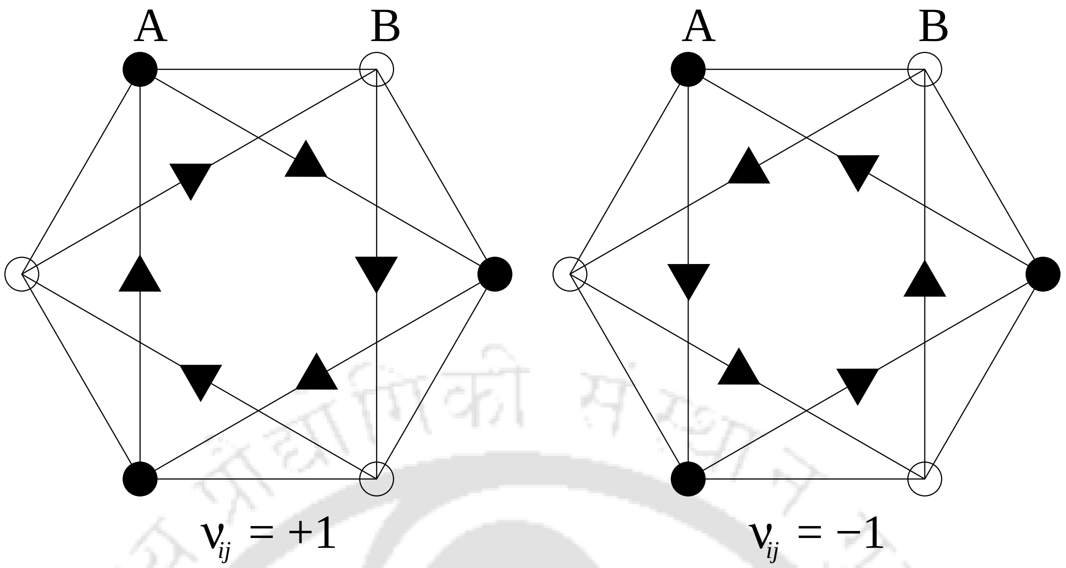

Figure 1.7: The sign structure, ν_{ij} of the next nearest neighbour (*nnn*) hopping term for a honeycomb lattice in the Kane-Mele model. While connecting to the *nnn* site via the *nn* site, a right turn denotes $\nu_{ij} = +1$ and a left one implies $\nu_{ij} = -1$.

1.6 Kane-Mele model

In quantum Hall effect the time reversal (τ) symmetry is broken by a strong perpendicular magnetic field. C. L. Kane and E. J. Mele[51] have shown that the spin-orbit interaction in a single plane of graphene leads to a τ-invariant quantum spin Hall state which has a bulk energy gap, and a pair of gapless spin filtered edge states at the boundary[50]. In their model, the perpendicular component of the spin, S_z is conserved. As a result, this model reduces to two independent copies, one for each spin of a model introduced by Haldane[86], which exhibits an integer quantum Hall effect even in the absence of a magnetic field.

They consider a tight-binding Hamiltonian of graphene, which generalizes the Haldane's model[86] and further includes spins with τ-invariant spin-orbit interactions. The Hamiltonian is written as[50,51],

$$H = t\sum_{\langle ij\rangle} c_i^\dagger c_j + \lambda_\nu \sum_i \xi_i c_i^\dagger c_i + i\lambda_{SO} \sum_{\langle\langle ij\rangle\rangle} \nu_{ij} c_i^\dagger \sigma_z c_j + i\lambda_R \sum_{\langle ij\rangle} c_i^\dagger \left(\mathbf{s} \times \hat{\mathbf{d}}_{ij}\right)_z c_j \quad (1.34)$$

The first two terms are spin independent. The first term denotes the nearest neighbour hopping term on a honeycomb lattice which has a structure of a triangular lattice with two (carbon) atoms per unit cell. This terms yields a Dirac semimetal as is the case for graphene. The second term is a staggered sublattice potential which violates the symmetry under twofold rotations in the plane. This term denotes the asymmetry between A and B sublattices, with ($\xi_i = \pm 1$), each sign for A and B sublattices. This term creates a gap in the spectrum and if the Fermi energy lies in the gap, the system is a trivial band insulator. The third term is the mirror symmetric spin-orbit interaction which involves spin dependent second neighbour hopping. $\nu_{ij} = (2/\sqrt{3})\left(\hat{d}_1 \times \hat{d}_2\right)_z = \pm 1$, where $\hat{d}_1$ and $\hat{d}_2$ are the unit vectors along the two bonds that the electron traverses while making a hop from a site i to next neighbour site j (see Fig.1.7). σ_z is the Pauli matrix. This term is crucial to study of a non-trivial topological state. The fourth term is the nearest neighbour Rashba term, which violates the $z \rightarrow -z$ mirror symmetry and a familiar component for our discussion.

Fig.1.8 shows the typical energy bands obtained by solving the lattice model for finite-sized zigzag strip geometry for a few representative points in the k-space. The trivial insulating and the non-trivial QSH phase are shown in the parameter space defined by λ_R, λ_ν and λ_{SO}. Both phases have a bulk energy gap and edge states, but in case of QSH phase, the edge states traverse the energy gap in pairs[51].

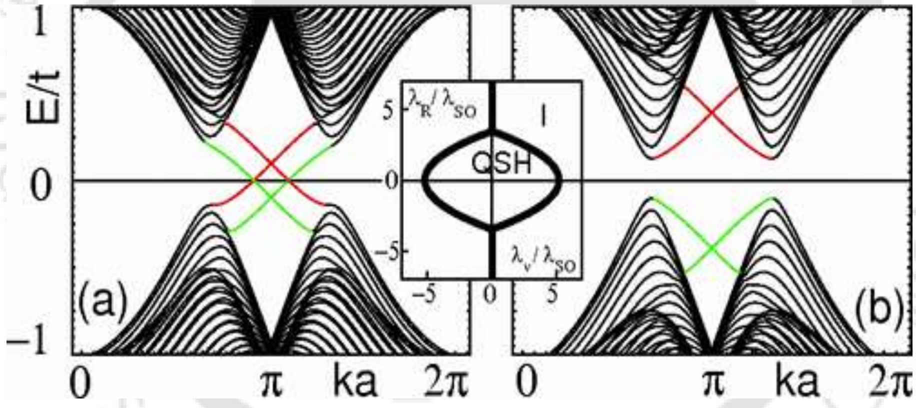

Figure 1.8: Energy bands for a one-dimensional zigzag strip in the (a) QSH phase $\lambda_\nu = 0.1t$ and (b) the insulating phase $\lambda_\nu = 0.4t$. In both cases $\lambda_{SO} = 0.06t$ and $\lambda_R = 0.05t$ The edge states on a given edge cross at $ka = \pi$. The inset shows the phase diagram as a function of λ_ν and λ_R for $0 < \lambda_{SO} \ll t$. Courtesy of Ref. [51].

1.7 Quantum spin Hall effect

The spin Hall (SH) effect can be thought of as the spin counterpart to the classical 'charge' Hall effect. In the SH effect, a transverse spin current flows, say, in the y-direction, due to an applied electric field in the x-direction. In contrast to the Hall effect, which breaks time reversal symmetry due to an applied magnetic field, the SH effect does not break time reversal symmetry. The charge Hall effect at low temperature and large magnetic field leads to its quantum analogue, called the quantum Hall (QH) effect, likewise the intrinsic SH effect of metals and insulators similarly have a quantum version, the quantum spin Hall (QSH) effect. The QSH state can be viewed as two copies of the QH state, one for each spin with opposite Hall conductances.

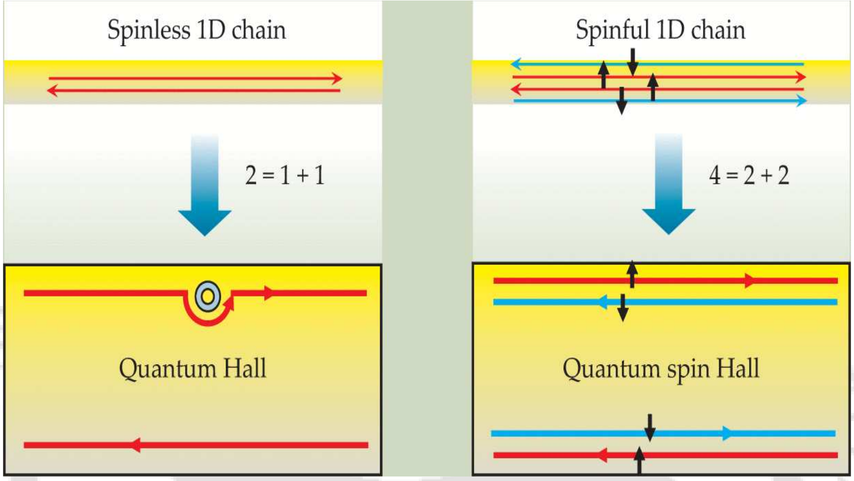

Figure 1.9: Schematic representation of the traffic rule. (left) A spinless 1D system has both a forward and a backward mover. Those two basic degrees of freedom are spatially separated in a QH state, as illustrated by the symbolic equation '2 = 1 + 1'. The upper edge contains only a forward mover and the lower one has an only backward mover. (right) A spinful 1D system has four basic channels, which are spatially separated in a QSH state. The upper edge contains a forward mover with up spin along with a backward mover with down spin at the lower edge. The spatial separation is illustrated by the symbolic equation '4 = 2 + 2'. Courtesy of Ref. [87].

What is quantized in the QSH effect, and in what sense is the QSH state a topological state of matter? These questions can be addressed by looking at whether this state supports stable gapless boundary modes or this state is robust to disorder. In case of QH state, electrons travel only along the edge of the sample (the so-called 'skipping orbits'), and the flow of electrons in mutually opposite directions are spatially separated where they propagated along the top and bottom edges of the sample. Compared with a 1D system (referred to as spinless 1D chain in Fig.1.9) with electrons propagating in both directions, the top edge of the QH bar contains only half the degrees of freedom. This unique spatial separation is shown in Fig.1.9 (left figure) and can be illustrated by the symbolic equation '2 = 1 [forward mover] + 1 [backward mover]'[87]. When an edge-state electron encounters an impurity, it simply takes a detour and still keeps going on in the same direction. That is why the QH effect is topologically robust.

By contrast, the QSH state can be qualitatively understood as two copies of the QH state, with one copy for each spin. Compared with a spinful 1D system, the top edge of a QSH system contains only half the degrees of freedom. This new pattern of spatial separation can be illustrated by the symbolic equation '$4 = 2 + 2$' as shown in Fig.1.9 (right figure), where each 2 corresponds to the spin degrees of freedom. These edge states for different spin species are robust to non-magnetic disorder. The spatial separation is achieved in case of the QSH effect via the TR invariant spin-orbit coupling. Since the QSH state is characterized by a bulk insulating gap and pair of gapless boundary states robust to disorder (with no available states to scatter to), the QSH state is indeed a new topological state of matter.

A topological state of matter is insulating in the bulk but supports gapless boundary states that are robust to disorder. Instead of being characterized by a local order parameter, the bulk is characterized by a topological invariant that, is obtained from integral of a geometric quantity. For example, in the case of the integer QH state, these topological invariants are the TKNN number[88] or the Chern number[89] which is obtained from the integral of the Berry curvature over the first Brillouin Zone. The bulk topological invariant is in turn related to the number of stable gapless boundary states and this emphasizes the bulk-edge correspondence for these classes of materials[90].

In the integer QH state, these invariants denote the number of stable gapless edge states (and hence conducting) and are also the value of the quantized Hall conductance in units of e^2/h. The topological order of the quantum spin Hall phase is characterized by a topological order parameter, known as the Z_2 topological index[51]. The Z_2 group contains only two elements, namely 0 and 1, with 1 corresponding to the topologically non-trivial QSH insulator and 0 corresponding to a topologically trivial insulator with no robust gapless edge states.

In our thesis, we have computed the conductance properties of graphene and its adatom decorated variants using recursive Green's function technique. The method, being completely a real space approach and the fact that we were interested in spintronic applications, computing these invariants are thought to be outside the purview of the methodology employed here. Instead, a $2e^2/h$ plateau in the longitudinal conductance of a two terminal graphene-based device, which is thought to be a signature for a non-trivial topological phase, is computed by us. Even that is shown 'not' to be a smoking gun for the QSH state in chapter 5.

Kane and Mele[50] and Bernevig and Zhang[52] independently proposed two systems to realize the QSH effect. The proposal by Kane and Mele is based on the spin-orbit interaction of graphene and is mathematically motivated by the earlier work of Haldane on the so-called quantum anomalous Hall effect (QAH effect)[86]. The proposal by Bernevig and Zhang is based on the spin-orbit interaction induced by strain in semiconductors. The second proposal has been verified experimentally[91]. However, both the ideas provide the important conceptual framework within which the stability of the QSH state can be investigated.

Let us try to understand the nature of a system consisting of the edge modes and the insulating bulk states. Seshadri et al.[92] in their paper have shown the emergence of these conducting edge states in presence of the intrinsic spin-orbit coupling (λ_{SO} term in Eq.(1.34)). However, it is enough for our purpose to demonstrate a few conditions that imply how these states arise which are propagating only at the edges and non-conducting at the bulk[48].

Nakada et al.[48] gave a derivation of the analytic expressions for the electronic wave functions corresponding to the edge states for a semi-infinite graphene sheet with a zigzag edge, that is ZGNR. The analytic form of the wave function is depicted in Fig.1.10. Considering the translational symmetry, one can construct the analytic

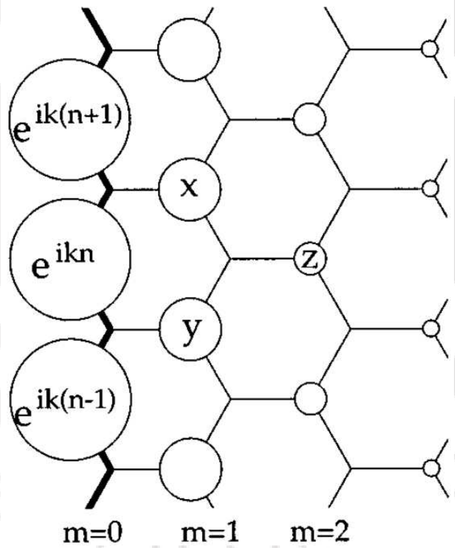

Figure 1.10: Analytic form of the edge states for a semi-infinite graphene sheet with a zigzag edge. The edges are shown by the bold lines. Each site is denoted by a location index, n on the zigzag chain and by a chain order index, m from the edge. Courtesy of Ref. [48].

solutions for the edge states by assuming the Bloch components of the linear combination of atomic orbitals (LCAO) wave function be ..., $e^{ik(n-1)}$, e^{ikn}, $e^{ik(n+1)}$, ... on the consecutive edge sites, where n denotes a site at the edge. The condition for the wave functions to be exact at $E = 0$ is that the total sum of the components of the complex wave function over the nearest neighbour sites should vanish. By applying this conditions, the wave functions at x, y and z (shown in Fig.1.10) are found to be $[-2\cos{(k/2)}]e^{ik(n+1/2)}$, $[-2\cos{(k/2)}]e^{ik(n-1/2)}$ and $[-2\cos{(k/2)}]e^{ikn}$ respectively. Thus the charge density is proportional to $[-2\cos{(k/2)}]^{2m}$ at each of the non-nodal site of the m-th zigzag chain with m increasing from the edge to the bulk. The wave functions would converge in a semi-infinite graphene sheet for $|-2\cos{(k/2)}| \leq 1$. Now one can see that the resultant nonbonding orbital is a wave function, that penetrates inwards from the edges with a decaying amplitude having a damping factor of $-2\cos{(k/2)}$ per zigzag chain. In Fig.1.10 the radius of each circle is proportional to the charge density. This comprehensively shows that even for a pristine graphene (without any intrinsic or Rahba spin-orbit coupling or a staggered sublattice potential), the edge states exist. This is verified by a $2e^2/h$ plateau in the longitudinal conductance of a two terminal graphene junction.

Outline of the thesis

In the following, we present a more elaborate plan of the thesis by including a description of the various problems that have been tackled in the form of different chapters of the thesis. There are a total of seven chapters. We proceed with a brief description in the context of each one by one. Chapter 1 contains an overview of the quantum transport in generic junction devices and graphene.

Chapter 2 deals with *Multi-terminal Landauer-Büttiker formula and Green's function formalism*. This chapter is reserved for the mathematical details used in this thesis. The theoretical framework commonly used to describe transport through these so-called mesoscopic devices is the Landauer-Büttiker approach[1]. In this chapter, we shall give a review of this method that computes the current in terms of transmission probabilities. The transmission coefficients can be calculated via computing the Green's functions[2]. In this chapter, we describe a convenient way to calculate Green's function numerically, which is obtained by using the recursive Green's function technique. For most of our numerical calculations of quantum transport in a variety of junction devices, we have used KWANT package[93]. A brief discussion of the essential features of the package is included. The results for the transport of a two-terminal junction device obtained via the numerical code written by us as a part of a pilot study have been checked with those obtained using KWANT. However, for more complicated geometries, such as GNR, KWANT is easier and efficient to implement.

Chapter 3 includes *effects of disorder on the conductance properties of a four terminal junction device.* We report a thorough theoretical investigation on the quantum transport of a disordered four terminal device in the presence of Rashba spin-orbit coupling (RSOC) in two dimensions. Specifically, we have computed the behaviour of the longitudinal (charge) conductance, spin Hall conductance (SHC) and spin Hall conductance fluctuations as a function of the strength of disorder and Rashba spin-orbit interaction. Both RSOC and disorder are found to have similar effects on the conductance properties, where both cause the longitudinal conductance and SHC diminish, with the SHC, out of the two, being more strongly affected by disorder. Further, we have extended the one parameter scaling theory[94] in presence of RSOC to assess the existence of a phase transition scenario therein.

Chapter 4 investigates *the transport of a three terminal, for example, a Y-shaped junction device.* We have studied spin Hall effect in a three terminal Y-shaped device in presence of tunable spin-orbit (SO) interactions. We have shown possible fabrication techniques for creating different angular separation between the two arms of the Y-shaped device, so as to investigate the effect of angular width on the longitudinal and the (SHC). A smaller angular separation is seen to yield a larger conductance. Also, arbitrary orientations of the spin quantization axes yield interesting three dimensional contour maps for the SHC corresponding to different angular separations of the Y-shaped device. In addition to the SHC demonstrating bounded behaviour for different angular separations, there are distinct symmetry axes about which SHC demonstrates reflection symmetry. The results explicitly show breaking of the spin rotational symmetry. Further, we have carried out a systematic study to compare and contrast between the possible SO terms, such as Rashba and Dresselhaus SO interactions and the interplay of the angular separation of the Y-shaped device therein. Interesting symmetry axes and periodic behaviour of the SHC are noted in this context. Also, the results reveal that the rotational symmetry in spin space is lost owing to the SO couplings present therein.

Chapter 5 deals with quantum transport in graphene and *nonmagnetic adatoms in graphene nanoribbons.* In this chapter, we study the charge and spin transport in two terminal (2T) and four terminal (4T) graphene nanoribbons (GNR) decorated with random Gold (Au) adatoms using a Kane-Mele model. The presence of the (QSH) phase is found to crucially depend on the strength of the intrinsic spin-orbit term, while the plateau in the longitudinal conductance at a $2e^2/h$ value is shown not to be the smoking gun for the QSH phase. Thus the Au adatoms which manage to induce only a small intrinsic spin-orbit coupling cannot guarantee a QSH phase, albeit yielding a $2e^2/h$ plateau in the longitudinal conductance around the zero of the Fermi energy. If other adatoms are capable of inducing larger spin-orbit strengths (we called them hypothetical adatoms), they would ensure both the plateau and the QSH phase as is evident from the presence of the conducting edge states. Motivated by these results, the spintronic applications are explored via computing the spin polarized conductance for both Au and hypothetical adatoms. One of the components of the spin polarized conductance renders dominant contribution owing to a finite width of the GNR in that direction and is shown to possess strikingly similar features with that of the longitudinal conductance. The other two components are finite and hence underscores the relevance of the RSOC in spintronic applications. Moreover, the fluctuations of the spin polarized conductance are shown to be useful quantities as they show specific trends, that is, they enhance with increasing adatom densities. The intrinsic SO coupling is shown to stabilize the QSH phase. Also, we have studied the behaviour of the charge and spin polarized conductances in 2T ZGNR and AGNR with Au adsorbates. Further to compute the spin Hall conductance, we have considered a four terminal GNR decorated with Au and Tl adsorbates. The longitudinal and the spin polarized conductances are compared and contrasted with those obtained for the 2T device.

Chapter 6 describes *the conductance of GNRs in presence of magnetic adatoms.* In this work, we study the charge and spin transport in two and four terminal graphene nanoribbons (GNR) decorated with a random distribution of magnetic adatoms to investigate the transport properties when TRS is explicitly violated. The inclusion of the magnetic adatoms may be included by an external exchange bias in the Kane-Mele Hamiltonian (with the intrinsic SOC being absent for magnetic adatoms). The magnetic adatoms generate only the z-component of the spin polarized conductance via the exchange bias term, while additionally RSOC as in the case of Fe, one is able to create all the three (x, y and z) components. This has important consequences for possible spintronic applications. The charge conductance shows interesting behaviour near the zero of the Fermi energy, where the familiar plateau at $2e^2/h$ vanishes, thereby transforming a quantum spin Hall insulating phase to an ordinary insulator. The local charge current and the local spin current provide an intuitive idea on the conductance features of the system. We have shown that profile of the local charge current flowing in the sample is independent of RSOC, while the three components of the local spin currents are sensitive to the RSOC. A 2T GNR device seems to be better suited for possible spintronic applications. We also study the behaviour of density of states (DOS) to understand the violation of TRS which is found to be fairly similar for 2T and 4T devices.

Since our focus has been studying transport properties of SOC throughout the thesis, we have not included explicitly an external magnetic field, which otherwise is central to the study of quantum Hall effect. Thus for the sake of completeness, we have included an external magnetic field in a six terminal GNR and revisited the familiar Hall effect in **Chapter** 7. The RSOC is found to have a detrimental effect on the width of the Hall plateaus. On a parallel ground, the magnetic field disrupts the familiar antisymmetric feature of the SHC.

Chapter 8 provides the *conclusions* of the thesis. In this chapter, we conclude with a highlight of the results obtained in the thesis.

Chapter 2

Analytic and computational methods

This chapter presents the theoretical formalism for determining the charge and spin-related transport properties of mesoscopic systems. Transport properties of mesoscopic systems have become more important and attractive in the past decades, and several successful theoretical formalisms have been devoted to studying the transport properties, such as, scattering matrix theory (SMT)[95], Green's function formalism[2,96,97], Kubo formula[98], transfer matrix method[99] etc. In the SMT, the transmission function and other transport properties are calculated from the Schrödinger equation in the coherent transport regime. From Fisher-Lee relation[100], the elements of the scattering matrix $\mathcal{S}$ can be obtained from the Green's function.

2.1 Landauer-Büttiker formula

It is well-known that the conductance (G) of a rectangular two-dimensional conductor is directly proportional to its width (W) and inversely proportional to its length (L). Then the conductance, G can be written as,

$$G = \sigma W/L \tag{2.1}$$

where σ is the proportionality constant, called the conductivity, which is a material property of the sample and independent of its dimensions. If this ohmic scaling relation were to hold as the length (L) is reduced, then one would expect the conductance to grow indefinitely. However, experimentally it is found that the measured conductance approaches a limiting value G_c, when the length of the conductor becomes much smaller than the mean free path ($L << L_m$), in other words, the conductor is a ballistic conductor. It is expected that the ballistic conductor must have zero resistance. There are corrections to this law arising from, (i) contact resistance: arises from the interface between the conductor and the contacts[101]; (ii) the conductance does not decrease linearly with width W, it depends on the number of transverse modes in the conductor and goes down in discrete steps as W is increased. The Landauer formula incorporates both of these features, and G is written as,

$$G = \frac{2e^2}{h} MT \tag{2.2}$$

where T is the average probability of an electron injected from one end of the conductor and will transit to other lead and with M being the number of the transverse modes (assuming the leads are ballistic conductors as well). Following Landauer's work, Büttiker proposed a simple and elegant solution to improve the formula. At zero temperature, the current flow takes place entirely due to difference in the electrochemical potential between the leads, namely μ_1 and μ_2, for which the two terminal linear response formula is given by,

$$I = \frac{2e}{h} \overline{T} \left[\mu_1 - \mu_2\right] \tag{2.3}$$

where $\overline{T}$ denotes the product of the number of modes M and the transmission probability per mode T at the Fermi energy. By treating all the probes on the equal footing, Eq.(2.3) can be extended by summing over all the terminals as,

$$I_p = \sum_q \left[\overline{T}_{q \leftarrow p} \mu_p - \overline{T}_{p \leftarrow q} \mu_q\right] \tag{2.4}$$

Let $V_i = \mu_i / e$, Eq.(2.4) can be written in the following form,

$$I_p = \sum_p \left[G_{qp} V_p - G_{pq} V_q\right] \tag{2.5}$$

where,

$$G_{pq} = \frac{2e^2}{h} \overline{T}_{q \leftarrow p} \tag{2.6}$$

The arrows in the subscripts have been inserted just as a reminder that the electron transfer is backwards from the second subscript to the first one. We shall generally write the subscripts without the arrows.

G_{pq} in Eq.(2.5) and Eq.(2.6) must satisfy the following 'sum rule' regardless of the detailed physics, in order to ensure that the current is zero when all the potentials are equal,

$$\sum_q G_{qp} = \sum_p G_{pq} \tag{2.7}$$

Due to the sum rule, Eq.(2.5) can be written as

$$I_p = \sum_p G_{pq} \left[V_p - V_q\right] \tag{2.8}$$

Landauer-Büttiker formalism provides a rigorous framework for the description of the conductance characteristics of the mesoscopic systems as long as the transport is coherent.

2.2 Transmission function and Scattering matrix

In this section, we shall discuss the relationship between the transmission function and the scattering matrix (or in short, the S-matrix) for coherent conductors.

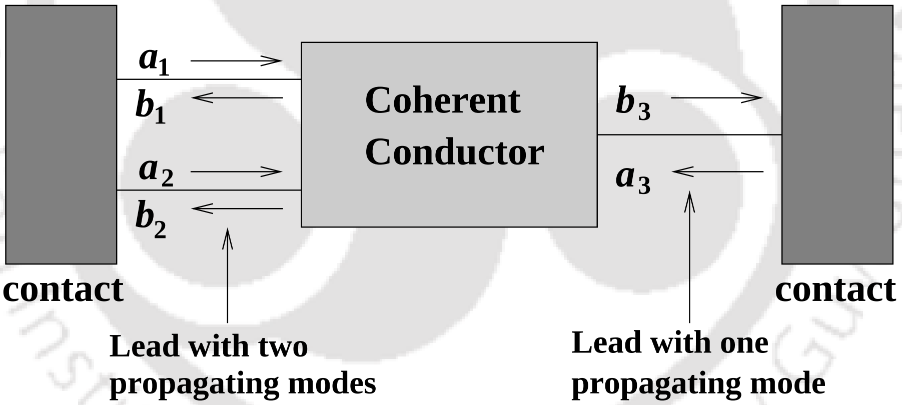

Figure 2.1: A coherent device can be characterized by a scattering matrix at each value of the propagating energy mode. The scattering matrix relates the outgoing mode amplitudes b to the incoming mode amplitudes a.

A coherent conductor can be characterized at each energy by an S-matrix that relates the outgoing wave amplitudes to the incoming wave amplitudes at the different leads. If there is a total of three modes in the leads as shown in Fig.2.1, we can write

$$\begin{pmatrix} b_1 \\ b_2 \\ b_3 \end{pmatrix} = \begin{pmatrix} s_{11} & s_{12} & s_{13} \\ s_{21} & s_{22} & s_{23} \\ s_{31} & s_{32} & s_{33} \end{pmatrix} \begin{pmatrix} a_1 \\ a_2 \\ a_3 \end{pmatrix} \tag{2.9}$$

The above equation can be written in matrix notation as

$$\{b\} = [S]\{a\} \tag{2.10}$$

In order to ensure current conservation, the S-matrix must be unitary and hence it must satisfy the condition,

$$[S]^{\dagger}[S] = \mathcal{I} = [S][S]^{\dagger} \tag{2.11}$$

In principle, one can calculate the S-matrix from the one electron Schrödinger equation if the vector potential $\mathbf{A}$ and the potential energy $U(x,y)$ inside the conductor are known. The main point is that for a coherent conductor, one can define and (if necessary) compute an S-matrix.

The transmission probability T_{nm} is obtained by taking the squared magnitude of the corresponding element of the S-matrix,

$$T_{m\leftarrow n} = |s_{m\leftarrow n}|^2 \tag{2.12}$$

Finally the transmission function $\overline{T}_{pq}(E)$ can be obtained by summing the transmission probability T_{nm} over all modes m in lead q and all modes n in lead p from the following relation,

$$\overline{T}_{p\leftarrow q} = \sum_{m\in q}\sum_{n\in p} T_{n\leftarrow m} = \sum_{m\in q}\sum_{n\in p} |s_{n\leftarrow m}|^2 \tag{2.13}$$

From now on, we shall simply denote the transmission function or the transmission coefficients by T_{pq}.

2.3 Transmission coefficients and the Green's Function

In the Landauer-Büttiker formalism, a central conducting device is connected to perfect leads and its current-voltage characteristics can be expressed in therm of transmission coefficients between those leads. These transmission coefficients are related to the Green's function of the central device. The transmission coefficient between the leads p and q is given by[100],

$$T_{pq} = \mathrm{Tr}\left[\Gamma_p G^r \Gamma_q G^a\right] \tag{2.14}$$

Γ_p are the coupling matrices representing the coupling between the central region and the leads and they are defined by the relation[2],

$$\Gamma_p = i\left[\Sigma_p - (\Sigma_p)^\dagger\right] \tag{2.15}$$

Here Σ_p is the retarded self-energy associated with the lead p. The self-energy contribution is computed by modeling each terminal as a semi-infinite perfect wire[102].

The retarded Green's function, G^r is defined as,

$$G^r = \left(E - H - \sum_p \Sigma_p\right)^{-1} \tag{2.16}$$

where E is the electron Fermi energy and H is the model Hamiltonian for the central conducting region. The advanced Green's function is defined in terms of the retarded one by, $G^a = (G^r)^\dagger$.

2.4 Green's Function formalism

For many years the transport calculations in two terminal ballistic systems have been done via the recursive Green's function method[103,104], and are also applicable for multi-terminal systems; but at a heavy price to be paid in terms of the efficiency of the algorithm, its stability etc. Several methods have been developed to make the recursive Green's function method more suitable for multi-terminal systems, such as optimal block-tridiagonalization scheme[105,106], decimation method[107], circular slicing scheme for a simple four-terminal cross[108], knitting algorithm[109] etc. Here we shall briefly describe the original two-terminal recursive Green's function method.

The recursive Green's function involves a partial inversion of the system Hamiltonian which is actually a block tridiagonal matrix. Here we consider for example a two terminal set up as shown in Fig.2.2.

The matrix representing the retarded Green's function G^r is just the inverse of

$$\mathbf{A} = E\mathbf{I} - \mathbf{H} \tag{2.17}$$

where $\mathbf{I}$ is an identity matrix, which has the same dimension as that of the system Hamiltonian matrix $\mathbf{H}$.

Since the leads are semi-infinite, $\mathbf{A}$ is an infinite dimensional matrix that describes the whole system (leads and the scattering region). We are interested in

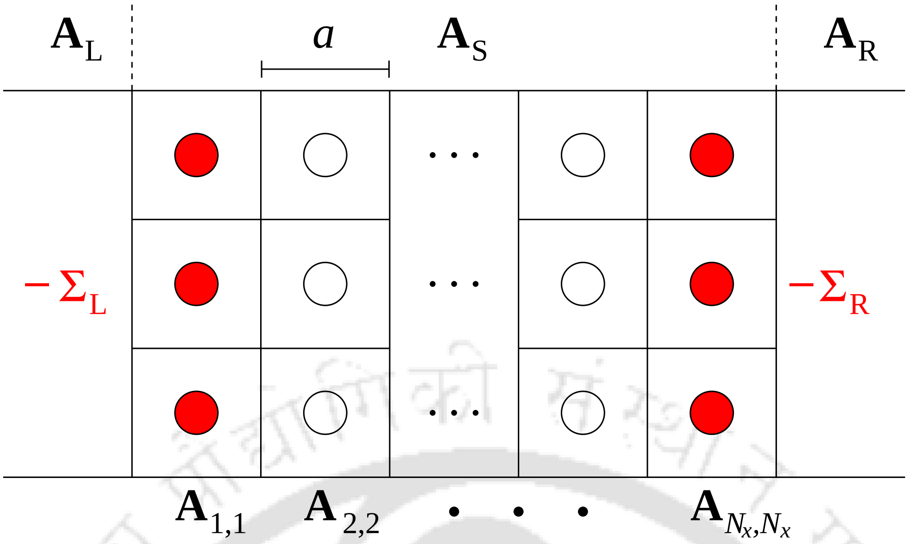

Figure 2.2: Schematic diagram for a two-terminal system discretized on a grid with mesh size a. The system is divided into three areas: a scattering region denoted by the matrix, $\mathbf{A}_S$ and two semi-infinite leads, $\mathbf{A}_L$ and $\mathbf{A}_R$. By grouping the discretized points into vertical slices, $\mathbf{A}_S$ takes the form of a block tridiagonal matrix. Slice i is then represented by the block $\mathbf{A}_{i,i}$. The effects of the semi-infinite leads are added as self-energies $\mathbf{\Sigma}_L$ and $\mathbf{\Sigma}_R$, to the points at the left and right boundaries of the scattering region.

knowing what happens in the central scattering region. In order to do so, we divide the Hamiltonian for the whole system into three parts: the left and right leads, represented by the infinite dimensional matrices $\mathbf{A}_L$ and $\mathbf{A}_R$ respectively, and the scattering region, denoted by $\mathbf{A}_S$ which is a finite sized $(N_x \times N_y)$ matrix, where N_x and N_y are the number of discretized spatial points in the x and y directions of the scattering region (see Fig.2.2). Then we can write the following equation for the whole system as,

$$\begin{bmatrix} \mathbf{A}_L & \mathbf{A}_{LS} & 0 \\ \mathbf{A}_{SL} & \mathbf{A}_S & \mathbf{A}_{SR} \\ 0 & \mathbf{A}_{RS} & \mathbf{A}_R \end{bmatrix} \begin{bmatrix} \mathbf{G}^r_L & \mathbf{G}^r_{LS} & \mathbf{G}^r_{LR} \\ \mathbf{G}^r_{SL} & \mathbf{G}^r_S & \mathbf{G}^r_{SR} \\ \mathbf{G}^r_{RL} & \mathbf{G}^r_{RS} & \mathbf{G}^r_R \end{bmatrix} = \begin{bmatrix} \mathbf{I}_L & 0 & 0 \\ 0 & \mathbf{I}_S & 0 \\ 0 & 0 & \mathbf{I}_R \end{bmatrix} \tag{2.18}$$

Matrices labeled A_j where $j = L, S, R$ have dimensions $N_j \times N_j$ where $N_S = N_x \times N_y$. The matrices labeled A_{jS} where $j = L, R$ have dimensions $N_j \times N_S$. At the end of the calculations we shall let $N_L \to \infty$ and $N_R \to \infty$ to obtain a continuous spectrum of the eigenvalues for A_L and A_R[2].

The matrices $\mathbf{A}_{Sj}$ are written as,

$$\mathbf{A}_{Sj} = \mathbf{A}^{\dagger}_{jS} = -\mathbf{H}_{Sj} = t\mathbf{I} \tag{2.19}$$

They result from the discretization and couple the scattering region to the left lead ($j = L$) and right lead ($j = R$). Since there is no direct coupling between the left and right leads, $\mathbf{A}_{LR} = \mathbf{A}_{RL} = 0$; Eq.(2.18) gives nine matrix equations from which we can isolate a finite matrix equation for $\mathbf{G}_S^r$,

$$\left(\mathbf{A}_S - \sum_j \mathbf{\Sigma}_j\right) \mathbf{G}_s^r = \mathbf{I} \tag{2.20}$$

whose dimension is the number of the spatial points in the scattering region. Here

$$\mathbf{\Sigma}_j = \mathbf{A}_{Sj} \mathbf{A}_j^{-1} \mathbf{A}_{jS} \tag{2.21}$$

is the self-energy contribution from the lead j. The same procedure stated above can be applied for any lead connecting to the system. Therefore Eq.(2.20) holds for multi-terminal systems where j will run over all leads.

The leads are assumed to be translationally invariant. Hence the self-energy matrix $\mathbf{\Sigma}_j$ can in most cases be worked out analytically[2]. In the next section, we have shown an example of the calculation of the self-energy of a lead. To simplify the notations we will from now on refer to $\mathbf{A}_S$ and $\mathbf{G}_S^r$ as simply $\mathbf{A}$ and $\mathbf{G}^r$. For a two terminal system, we order the matrix elements of $\mathbf{A}$ in such a way that each diagonal block $\mathbf{A}_{i,i}$ represents a vertical slice at i in the scattering region (Fig.2.2). With this ordering the self-energies from the left and right leads add only to the first and last diagonal blocks respectively, that is, $\mathbf{A}_{1,1}$ and $\mathbf{A}_{N_x,N_x}$. This is important because the block tridiagonal form is then preserved, enabling us to use the recursive algorithm.

2.5 Evaluation of the self-energy

For the semi-infinite leads as shown in Fig.2.2, the translational invariance is preserved in the x-direction. The wave function amplitude at any arbitrary site, m of the leads can be written as,

$$\phi_m \propto e^{ik_x m_x a} \sin\left(k_y m_y a\right) \tag{2.22}$$

Where a denotes the lattice constant and (m_x, m_y) are the position coordinates of the mth site in two dimensions. The tight binding energy in a square lattice is of the form,

$$E = 2t_L\left[\cos\left(k_x a\right) + \cos\left(k_y a\right)\right] \tag{2.23}$$

t_L denotes the hopping energy of the electrons in the leads. In Eq.(2.23), k_x is continuous, while k_y has discrete values given by,

$$k_y(i) = \frac{i\pi}{(M+1)a} \tag{2.24}$$

Here $i = 1, 2, 3, ..., M$. M is the total number of transverse channels in the leads, and in our case $M = N_y$. The self-energy matrices are constructed in the reduced Hilbert space of the conductor itself. These matrices have non-zero elements only for the sites on the edge layer of the sample that couple to the leads and are given by [2],

$$\Sigma_{L(R)}(m,n) = \frac{2}{M+1}\sum_{k_y} \sin\left(k_y m_y a\right)\Sigma\left(k_y\right)\sin\left(k_y n_y a\right), \tag{2.25}$$

$\Sigma\left(k_y\right)$ is the self-energy of each transverse channel and for any value of k_y it becomes,

$$\Sigma\left(k_y\right) = \frac{t_C^2}{t_L^2}\left[E - \epsilon\left(k_y\right) - i\sqrt{4t_L^2 - \left(E - \epsilon\left(k_y\right)\right)^2}\right] \tag{2.26}$$

with $\epsilon\left(k_y\right) = 2t_L\cos\left(k_y\right)$, when the energy lies within the band, that is, $|E-\epsilon\left(k_y\right)| < 2t_L$, and

$$\Sigma\left(k_y\right) = \frac{t_C^2}{t_L^2}\left[E - \epsilon\left(k_y\right) \mp \sqrt{\left(E - \epsilon\left(k_y\right)\right)^2 - 4t_L^2}\right] \tag{2.27}$$

when the energy lies outside the band. Here the negative sign appears for $E > \epsilon(k_y) + 2|t_L|$ and positive holds for $E > \epsilon(k_y) - 2|t_L|$. This self energy can be used in Eq.(2.16) in order to calculate the conductance.

2.6 The recursive Green's Function algorithm for two-terminal systems

The recursive Green's function algorithm focuses on finding either the diagonal blocks or selected block columns of an inverted block tridiagonal matrix. This method is sometimes called partial inversion since only part of the Green's function is calculated. For example, in order to calculate the charge density, one needs the first and last columns of the full Green's function.

The algorithm is divided into three parts. In Fig.2.3, we show schematically the working algorithm for a simple 3 × 3 example system.

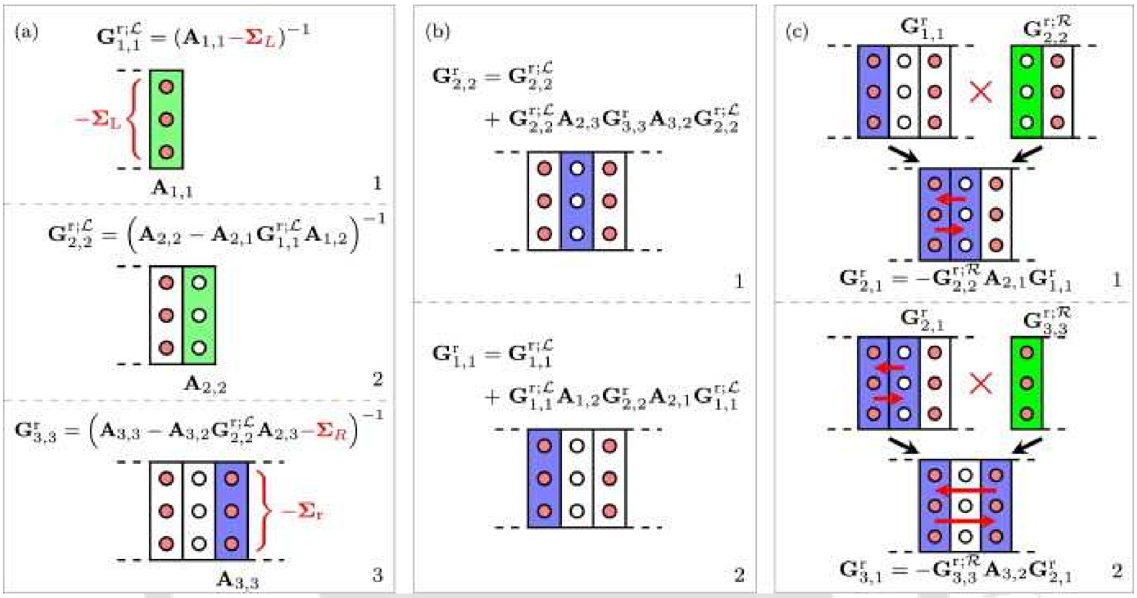

Figure 2.3: Schematic diagram showing the recursive Green's function method applied to a 3 × 3 two dimensional example system. (a) Forward algorithm using Eqs.(2.28), (2.29), (2.30). (b) The backward algorithm, using Eq.(2.31). (c) The first column of the full Green's function is calculated using Eq.(2.33). Courtesy of Ref. [110].

(i) The first part is the so called forward algorithm and is demonstrated in Fig.2.3. This part uses the same method outlined above where the effects of the semi-infinite leads are incorporated through the self-energy term into the scattering region. We begin by dividing the system into vertical slices. The first slice, already containing the self-energy of the left lead, is inverted and added to the next slice to the right. This procedure is continued until we reach the last slice. The procedure can be summarized as,

$$\text{First slice:} \quad \mathbf{G}^{r;\mathcal{L}}_{1,1} = (\mathbf{A}_{1,1} - \boldsymbol{\Sigma}_L)^{-1} \tag{2.28}$$

$$i\text{-th slice:} \quad \mathbf{G}^{r;\mathcal{L}}_{i,i} = \left(\mathbf{A}_{i,i} - \mathbf{A}_{i,i-1}\mathbf{G}^{r;\mathcal{L}}_{i-1,i}\mathbf{A}_{i-1,i}\right)^{-1} \quad (i = 2, \ldots, N_x - 1) \tag{2.29}$$

$$\text{last slice:} \quad \mathbf{G}^{r;\mathcal{L}}_{N_x,N_x} = \left(\mathbf{A}_{N_x,N_x} - \mathbf{A}_{N_x,N_x-1}\mathbf{G}^{r;\mathcal{L}}_{N_x-1,N_x}\mathbf{A}_{N_x-1,N_x} - \boldsymbol{\Sigma}_R\right)^{-1} \tag{2.30}$$

Since the last slice contains the self-energy of the right lead, the Green's function of the last slice is exact, that is, $\mathbf{G}^{r}_{N_x,N_x} = \mathbf{G}^{r;\mathcal{L}}_{N_x,N_x}$. Above we applied the algorithm from the left to right and we used the notation $\mathcal{L}$ to mark that the above Green's function to be a left-connected Green's functions. The algorithm can also be applied from the right to left, which would produce right-connected Green's function marked with $\mathcal{R}$. These right connected Green's function will play a role in the last part of the algorithm.

(ii) The second part is called the backward algorithm and computes the diagonal blocks of the full Green's function. From the forward algorithm we obtained the last block on the diagonal of the full Green's function. Using a discrete version of the Dyson equation we can couple it to the left connected Green's function $\mathbf{G}^{r;\mathcal{L}}_{N_x-1,N_x-1}$ of the adjacent slice on the left. This produces diagonal block number $N_x - 1$ of the full Green's function. We then continue this procedure until we have calculated all the diagonal blocks:

$$\mathbf{G}^{r}_{i,i} = \mathbf{G}^{r,\mathcal{L}}_{i,i} + \mathbf{G}^{r;\mathcal{L}}_{i,i}\mathbf{A}_{i,i+1}\mathbf{G}^{r}_{i+1,i+1}\mathbf{A}_{i+1,i}\mathbf{G}^{r;\mathcal{L}}_{i,i}, \quad i = N_x - 1, ..., 1 \tag{2.31}$$

In Fig.2.3(b) we use the backward algorithm on our example system.

(iii) Finally, the third part calculates the off-diagonal blocks. It uses the Dyson equation to couple together the exact diagonal blocks with left or right connected Green's functions to produce the off-diagonal blocks or above the diagonal line.

$$\mathbf{G}^{r}_{i-1,j} = -\mathbf{G}^{r;\mathcal{L}}_{i-1,i-1}\mathbf{A}_{i-1,i}\mathbf{G}^{r}_{i,j}, \quad 1 < i \leq j \leq N_x \tag{2.32}$$

$$\mathbf{G}^{r}_{i+1,j} = -\mathbf{G}^{r;\mathcal{R}}_{i+1,i+1}\mathbf{A}_{i+1,i}\mathbf{G}^{r}_{i,j}, \quad N_x - 1 \geq i \geq j \geq 1 \tag{2.33}$$

In Fig.2.3(c) we apply Eq.(2.33) to calculate the first column of the Green's function of our example system.

Using the above technique we calculate the two-terminal conductance for a scattering region having the dimension of a 16×16 square lattice (with two semi-infinite leads) in presence of an onsite (potential) disorder as shown in Fig.2.4 for example. The disorder is assumed from a random rectangular distribution centered at the zero energy. In the absence of disorder, the conductance increases in discrete steps as we increase the Fermi energy for $E < 0$, and for $E > 0$, it decreases again in discrete steps showing the quantum nature of the system. That is conductance is only possible when the system offers an energy mode to conduct. As the disorder is introduced, the step-like feature is lost and also the overall magnitude of the conductance decreases with increasing strength of disorder owing to the scattering effects. The behaviour of the normalized conductance is symmetric as a function of the Fermi energy irrespective of the disorder strength. This is shown in Fig.2.4. Further, the discrete steps in the conductance properties get washed out owing to the availability of additional (localized) modes contributed by the random disorder,

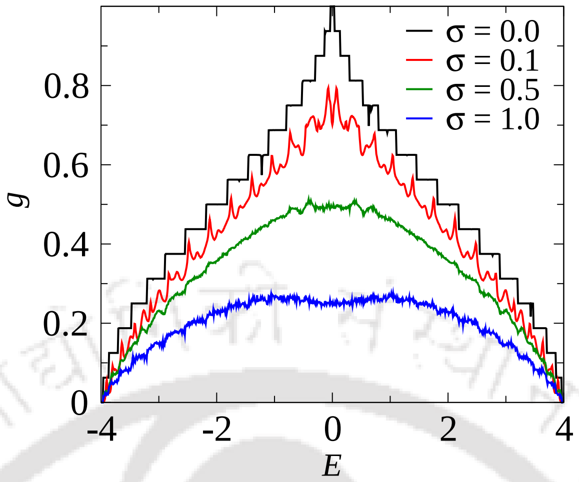

Figure 2.4: The normalized two-terminal conductance, g is plotted as a function of the Fermi energy, E for different strengths of disorder, σ. With increasing the disorder strength, the conductance decreases.

2.7 Kwant: a package for computing quantum transport

To calculate the transmission probability for complex geometries, and to facilitate efficient calculations, the Kwant package[93] is used. Kwant is a free (open source) Python package for numerical calculations on tight binding models with a strong focus on quantum transport. It is designed to have flexible and easy to use features. Though Kwant can calculate the transmission coefficients through the RGF technique (described earlier), but it also uses highly efficient and robust algorithms that allow one to significantly outperform the most commonly used recursive Greens function methods. Apart from the transmission coefficients, Kwant can calculate a variety of quantities, for example, band structure of leads, local density of states, local currents and much more.

In our earlier works, we have used the recursive Green's function algorithm as discussed above. However, since the package, Kwant is easy to implement and computationally highly efficient, for most of our thesis work Kwant package is used. In the following, we have shown the behaviour of normalized conductance as a function of the Fermi energy for a 16 × 16 square shaped two terminal scattering device. The result obtained via the numerical code build by us and that from Kwant code are plotted as shown in Fig.2.5.

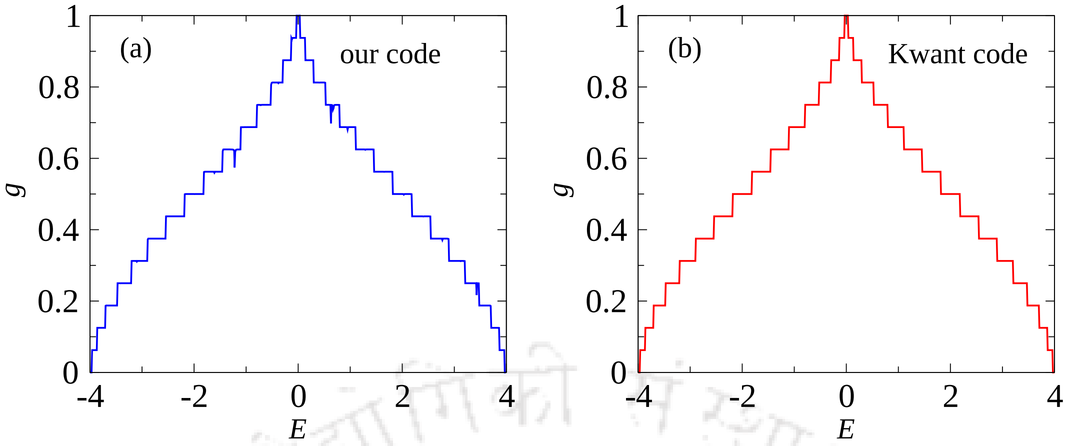

Figure 2.5: The normalized conductance g is plotted as a function of the Fermi energy E. (a) Generated via our code. (b) Generated from Kwant package. Both the plots are quiet in good agreement.

2.8 Non-equilibrium Green's function

Up to now what we have discussed was based on equilibrium Green's function formalism. On the other hand, the non-equilibrium Green's function (NEGF) formalism provides a microscopic theory for quantum transport including interactions. In the absence of external fields, the NEGF method reduces to the equilibrium Green's function method. NEGF can be applied to both extended and finite systems and it can handle strong external fields nonperturbatively. The electron-electron interactions are taken by infinite summations. The NEGF theory was developed by Keldysh[111] and, in a slightly different form, independently by Kadanoff and Baym[112]. In the last decade, the NEGF method has been developed to investigate and predict transport properties of nanoscale materials as well as the operation and the performance of nanoscale devices. The NEGF method has been implemented via many computer packages with different sophisticated levels, such as, combined with density-functional calculations[113], or based on effective physical models[114–116]. However, many technical and physical issues still need to be solved to improve the effectiveness and the performance of such computational tools in various applications.

Since we did not consider any kind of external interactions such as electron-electron interactions etc., the implementation of NEGF is beyond the scope of this thesis.

Chapter 3

Disorder effect in a four terminal Rashba coupled junction device

As we have discussed earlier, spintronics or spin-based electronics focuses on transportation of electron spins in a variety of semiconducting materials[25,37,117]. The prospects of obtaining a dissipationless spin current along with a large number of possible applications have generated intense activities from both the theoreticians and the experimentalists.

While there were early attempts of injecting spin-polarized charge carries (from ferromagnetic metals) in non-magnetic semiconductors (thereby converting them to dilute magnetic semiconductors), they have yielded very limited success. However the recent discovery of intrinsic spin Hall effect (SHE) in p-type semiconductors, that originate from an effective magnetic field that causes the up and down spin electrons to drift in opposite directions has contributed immensely to the ongoing experimental work on spin manipulation phenomena in real materials[37]. In two-dimensional electron gases (2DEG), one can hope to realize some of the interesting physics in this regard in presence of Rashba spin-orbit coupling (RSOC)[38].

In this chapter, we shall concentrate on the Hall effect (for both charge and spin) induced by RSOC in a four terminal junction device. As these devices are intrinsically disordered, we incorporate random potential disorder and investigate how the conductance properties of the disordered system are renormalized in presence of RSOC. The existing work on the subject of the interplay of disorder and RSOC on the conductance properties of such junction devices is limited and not beyond controversy[118–120].

In a simple language, the existence of RSOC distinguishes the up and down spin electrons and hence a potential gradient is generated, which causes the opposite spins to drift towards the mutually opposite transverse direction. Thus an accumulation of spins can be observed along the edges of the sample, which yields SHE. In experiments, such accumulation of spins could be optically detected by using the Kerr rotation spectroscopy[121,122].

The spin polarization in a two-dimensional electron gas (2DEG) is spatially resolved using the low-temperature scanning Kerr rotation microscopy[123]. A linearly polarized beam is directed at the sample through an objective lens. The rotation of the polarization axis of the reflected beam provides a measure of the electron spin polarization. Fig.3.1 shows that the electron polarization is localized at the two opposite edges of the sample as seen from (A) spin density and (B) reflectivity. Plots obtained by the Kerr rotation measurement.

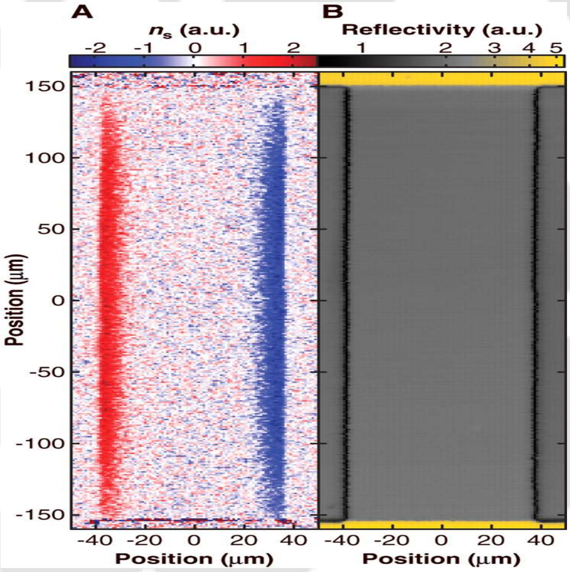

Figure 3.1: (A and B) Two-dimensional images of the spin density n_s and the reflectivity R, respectively, for the unstrained GaAs sample measured at $T = 3$ K and $E = 10$ mVμm^{-1}. Opposite spins are seen to accumulate at the two edges. Courtesy of Ref. [121].

Now, as disorder is mostly an inextricable component in real systems, we seek to study the effect of disorder on the spin Hall conductance properties of disordered samples. The issue is particularly relevant because of a number of reasons. On one hand, there are studies that claim that SHE can be strongly suppressed by disorder effects[124] signaling the onset of spin relaxation and diffusion[125], while the other school of thought says that since the spins are tightly locked with their momenta (in presence of RSOC), SHE should be resilient to a disorder potential[126]. Also, there are suggestions of the emergence of a metallic behaviour at a certain critical disorder strength in the presence of RSOC, which however vanishes (as it should be) with the vanishing of the Rashba coupling[118]. Therefore the scenario warrants a more complete study to settle some of the crucial issues in these regards.

Also the universal charge conductance fluctuation[127] is one of the most striking quantum transport features in mesoscopic physics, which arises as a consequence of quantum interference when the inelastic diffusion length exceeds sample dimensions. It is well known that the conductance fluctuations are of the order of e^2/h and are universal features of quantum transport in the low-temperature limit. In particular, they are independent of both the degree of disorder and the sample size at zero temperature.

Analogously one can study the fluctuations in spin Hall conductance and it is found that there exist a universal spin Hall conductance fluctuations, which has a finite value, independent of other system details. However, this fluctuation is a function of the spin-orbit interaction strength[128–130]. In this chapter, we study the variation of spin Hall conductance fluctuation as a function of the disorder strength and the strength of RSOC in order to observe the universality and independent nature of spin Hall conductance fluctuations.

Motivated by the preceding discussion, we aim to investigate in a four terminal junction device the spin Hall conductance, the usual charge conductance (referred to as the longitudinal conductance), the universal spin Hall conductance fluctuation (the corresponding root mean square value of which being 0.36 $\left(\frac{e}{8\pi}\right)$), which is independent of other parameters of the Hamiltonian and is thus attributed as '*universal*'[128].

Further, we have critically examined the suggestion of the onset of a metallic regime at a certain critical disorder strength for a given value of the spin orbit coupling parameter via investigating the behaviour of the longitudinal conductance as pointed out by Sheng et. al[118]. Their claim is that there is possibility of a metal to an insulator transition in 2D, as the spin-orbit coupling vanishes, the critical disorder strength vanishes too, thereby yielding an absence of a metal insulator transition in two dimensions in the absence of RSOC, a result that is well known.

While we are thoughtful about the applicability of a one parameter scaling theory[94] in presence of RSOC, however, went ahead assuming it is at least applicable for a particular value of the spin-orbit coupling parameter. We do not find any convincing evidence in a Rashba coupled disordered four terminal junction or at best the results do not help in arriving at unambiguous inferences about it. Our inference on the 'possible' absence of an emerging metallic phase is justified as the Rashba term preserves the time reversal symmetry, an essential ingredient for the current 'echo' associated with the quantum interference effects that give rise to weak localization. An external magnetic field would have radically modified these arguments.

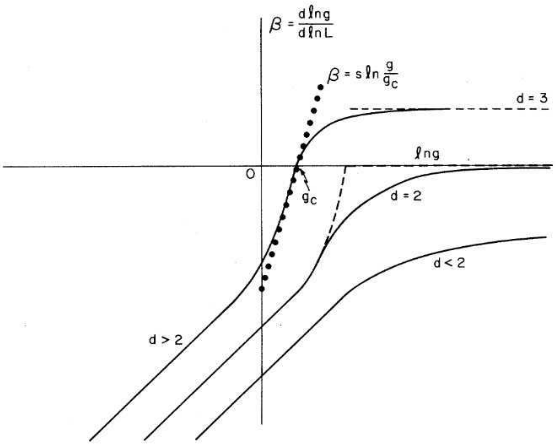

Figure 3.2: Plot of $\beta(g)$ vs ln$g$ for $d > 2$, $d = 2$, $d < 2$. $G(L)$ is the normalized 'local conductance'. The approximation $\beta = s\ \ln(g/g_c)$ is shown for $d > 2$ as the solid-circled line; this unphysical behaviour necessary for a conductance jump in $d = 2$ as shown by the dashed line. Courtesy of Ref. [94].

For a hypercube in d-dimensions, the linear dimension, L is proportional to the conductivity, G at zero temperature. The dependence is expressed as,

$$G(L) = \sigma L^{d-2} \tag{3.1}$$

The proportionality constant, σ is the conductance of the sample which has the dimension of e^2/h and is independent of the spatial dimension of the sample. For an experimentalist, G is an important quantity to obtain, while theorists are interested in computing σ. Something interesting happens in two dimensions, where G becomes numerically equal to σ.

The dimensionless conductance of a hypercube will be of interest in the scaling theory of localization and a useful quantity in this regard is defined as,

$$g(L) \equiv \frac{G(L)}{\frac{e^2}{h}} \tag{3.2}$$

The one-parameter scaling theory of localization says that the dimensionless conductance solely determines the conductivity behaviour of a disordered system. Suppose we fit n^d identical blocks of length L into a hypercube of linear dimension nL, where each block has the same impurity concentration and the system is considered to be in the ballistic regime. The conductance of the hypercube, $G(nL)$ is then related to the conductance of each block, $g(L)$ by the relation,

$$g(nL) = f(n, g(L)) \tag{3.3}$$

f is an appropriate functional. This is the one-parameter scaling assumption, the conductance of each block solely determines the conductance of the larger block.

In the scaling theory, proposed by Abrahams et al.[94](popularly referred to as the '*gang of four*'), the logarithmic derivative of the conductance with respect to the system size is defined by a single quantity, usually denoted by β, which depends only on the conductance itself and not individually on energy, system size and disorder.

Weak localization in two-dimensional systems can be best characterized by the relation[94],

$$\beta = \frac{d \ln g(L)}{d \ln L} \tag{3.4}$$

where, $g(L)$ is the charge conductance and L is the length of the conductor. Fig.3.2 shows the $\beta(g)$ vs $\ln g(L)$ plot. For the dimensions, $d = 1$ and $d = 2$, $\beta(g)$ is always negative implying an insulating behaviour that is all states are localized even at an infinitesimal value of disorder. In $d = 3$, there is a critical point, g_c, above which the system is diffusive (leading to a conducting behaviour), and below the critical point, the system is insulating. For 2D (and lower dimensions), the trajectory never crosses (or meets) the x-axis and that means that a two-dimensional electronic system is never metallic even in presence of small disorder. Since in this chapter we are dealing with the 2D system, the current situation demands a detailed analysis of the metal-insulator transition in presence of Rashba interaction.

We organize this chapter as follows. The theoretical formalism leading to the expressions for the spin Hall and longitudinal conductances using Landauer Büttiker formula are presented in the next section. After that, we include an elaborate discussion on the results obtained for the longitudinal conductance, spin Hall conductance and fluctuation in the spin Hall conductance that is helpful in depicting the interplay of disorder strength and RSOC parameter in details.

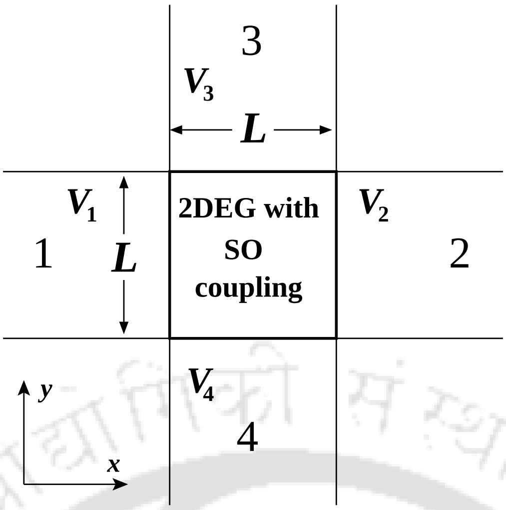

Figure 3.3: Cross-shaped device with four semi-infinite metallic leads. The spin-orbit coupling exists in the central region only, and the effect of the semi-infinite leads is treated exactly through the self-energy terms.

3.1 Theoretical formulation

3.1.1 System and the Hamiltonian

In order to observe the spin Hall effect, we choose a four-probe measuring set-up as shown in Fig.3.3. Here the four ideal (disorder free) semi-infinite leads are attached to the central conducting region which in our case is a square lattice with Rashba spin-orbit interaction. An unpolarized charge current is allowed to pass through the longitudinal leads along lead-1 and lead-2 (see Fig.3.3) inducing spin Hall current in the transverse directions that are along lead-3 and lead-4. The discrete spectrum of the longitudinal region is assumed to be described within the framework of tight-binding approximation assuming only nearest-neighbor hopping. The Hamiltonian for the entire system can be represented by a sum of three terms, which are,

$$H = H_{sq} + H_{leads} + H_{coupling} \tag{3.5}$$

The first term represents the Hamiltonian for the system with a square lattice geometry with Rashba spin orbit interaction and is defined by,

$$
\begin{aligned}
H_{sq} = \sum_{i,\sigma} \epsilon_i c^\dagger_{i\sigma} c_{i\sigma} + t \sum_{\langle ij \rangle,\sigma} c^\dagger_{i\sigma} c_{j\sigma} + \\
\alpha \sum_{i} \Big[\Big(c^\dagger_{i\uparrow} c_{i+\delta_x\downarrow} - c^\dagger_{i\downarrow} c_{i+\delta_x\uparrow} \Big) \\
-i \Big(c^\dagger_{i\uparrow} c_{i+\delta_y\downarrow} + c^\dagger_{i\downarrow} c_{i+\delta_y\uparrow} \Big) \Big]
\end{aligned}
\tag{3.6}
$$

Here, ϵ_i is the random on-site potential energy chosen from a uniform rectangular distribution ($-W$ to W), $c_i^\dagger$ and c_i correspond to the creation and annihilation operators respectively, for an electron at the site i of the conductor. Here $t = \frac{\hbar}{2m^* a_0^2}$ (m^*: effective mass and a_0: lattice constant) is the hopping integral, α is the Rashba coupling strength. $\delta_{x,y}$ are the unit vectors along x, y directions.

The four metallic leads attached to the conductor are considered to be semi-infinite and ideal. Thus the leads are described by a similar non-interacting single particle Hamiltonian as written below,

$$
H_{leads} = \sum_{i=1}^{4} H_i, \tag{3.7}
$$

where,

$$
H_i = \epsilon_L \sum_n c_n^\dagger c_n + t_L \sum_{\langle mn \rangle} c_m^\dagger c_n \tag{3.8}
$$

Similarly the conductor-to-lead coupling is described by the following Hamiltonian,

$$
H_{coupling} = \sum_{i=1}^{4} H_{coupling,i} \quad , \tag{3.9}
$$

where,

$$
H_{coupling,i} = t_C \left[c_i^\dagger c_m + c_m^\dagger c_i \right] \tag{3.10}
$$

In the above expression, ϵ_L and t_L denote site energies and nearest-neighbor hopping between the sites at the leads. The coupling between the conductor and the leads is defined by the hopping integral t_C. In Eq.(3.10), i and m belong to the boundary sites of the square lattice and leads, respectively. The summation over i accounts for the four attached leads.

3.1.2 Formulation of longitudinal and spin Hall conductances

For the four-probe case, where pure spin current is expected to flow through the transverse leads, due to the flow of charge current through the longitudinal leads, the longitudinal and spin Hall conductances are defined as[131],

$$G_L = \frac{I_2^q}{V_1 - V_2} \tag{3.11}$$

and

$$G_{SH} = \frac{\hbar}{2e}\frac{I_3^s}{V_1 - V_3} = \frac{\hbar}{2e}\frac{I_3^{\uparrow} - I_3^{\downarrow}}{V_1 - V_3} \tag{3.12}$$

where I_2^q and I_3^s are the charge and spin currents flowing through the lead-2 and lead-3 respectively. V_m is the potential at the m-th lead. $I_3^{\uparrow}$ and $I_3^{\downarrow}$ are the up and down spin currents flowing in lead-3.

The calculation of charge and spin currents is based on the Landauer-Büttiker multi-probe formalism[132]. The charge and spin currents flowing through the lead m with potential V_m, can be written in terms of spin resolved transmission probability as[81]

$$I_m^q = \frac{e^2}{h} \sum_{n \neq m, \sigma, \sigma'} \left(T_{nm}^{\sigma\sigma'} V_m - T_{mn}^{\sigma'\sigma} V_n \right) \tag{3.13}$$

$$I_m^s = \frac{e^2}{h} \sum_{n \neq m, \sigma'} \left[\left(T_{nm}^{\sigma'\sigma} - T_{nm}^{\sigma'-\sigma} \right) V_m + \left(T_{mn}^{-\sigma\sigma'} - T_{mn}^{\sigma\sigma'} \right) V_n \right] \tag{3.14}$$

The spin current through lead m can be written in a more compact form, such as,

$$I_m^s = \frac{e^2}{h} \sum_{n \neq m} \left[T_{nm}^{out} V_m - T_{mn}^{in} V_n \right] \tag{3.15}$$

where, we have defined two useful quantities as follows,

$$T_{pq}^{in} = T_{pq}^{\uparrow\uparrow} + T_{pq}^{\uparrow\downarrow} - T_{pq}^{\downarrow\uparrow} - T_{pq}^{\downarrow\downarrow} \tag{3.16}$$

$$T_{pq}^{out} = T_{pq}^{\uparrow\uparrow} + T_{pq}^{\downarrow\uparrow} - T_{pq}^{\uparrow\downarrow} - T_{pq}^{\downarrow\downarrow} \tag{3.17}$$

Physically the term $\frac{e^2}{h} \sum\limits_{n \neq m} T_{nm}^{out} V_m$ in Eq.(3.15) is the total spin current flowing from the m-th lead with potential V_m to all other n leads, while the term $\frac{e^2}{h} \sum\limits_{n \neq m} T_{mn}^{in} V_n$ refers to the total spin current flowing into the m-th lead from all other n leads maintained at potential V_n.

For the sake of completeness, we shall re-run a portion of the formalism that computes the conductance through the knowledge of the transmission coefficient.

The zero temperature conductance, $G_{pq}^{\sigma\sigma'}$ that describes the spin resolved transport properties, is related to the spin resolved transmission coefficient as[1,133],

$$G_{pq}^{\sigma\sigma'} = \frac{e^2}{h} T_{pq}^{\sigma\sigma'}(E) \tag{3.18}$$

The transmission coefficient appearing above can be calculated in terms of the Green's function by the relation[100,134],

$$T_{pq}^{\sigma\sigma'} = \mathrm{Tr}\left[\Gamma_{\mathrm{p}}^{\sigma} \mathrm{G_R} \Gamma_{\mathrm{q}}^{\sigma'} \mathrm{G_A}\right] \tag{3.19}$$

Γ_p^σ's are the coupling matrices that represent the coupling between the central region and the leads, and they are defined by the relation[2],

$$\Gamma_p^\sigma = i\left[\Sigma_p^\sigma - (\Sigma_p^\sigma)^\dagger\right] \tag{3.20}$$

Here Σ_p^σ is the retarded self-energy associated with the lead p. The self-energy contribution is computed by modeling each terminal as a semi-infinite perfect wire[102].

The retarded Green's function, G_R is computed as

$$G_R = \left(E - H - \sum_{p=1}^{4} \Sigma_p\right)^{-1} \tag{3.21}$$

where E is the electron energy and H is the Hamiltonian for the central conducting region. The advanced Green's function is obtained from the retarded one by the relation,

$$G_A = G_R^\dagger \tag{3.22}$$

This energy, E appearing in Eq.(3.18) and Eq.(3.21) is the Fermi energy, E_F at $T = 0$. Thus E depends on the density of the charge carriers in the scattering region. It may be noted that the biasing energy, E controls the density of the charge carriers flowing through the conducting region. Thus E plays the same role of the Fermi energy of the system. Hence throughout the thesis, whenever we refer to the conductance (G) plots as a function of energy, we imply Fermi energy.

Now, following the spin Hall phenomenology, the net charge currents through lead-3 and lead-4 is zero that is, $I_3^q = I_4^q = 0$, because of the transverse leads are voltage probes in our set-up. On the other hand, as the currents in various leads depend only on voltage differences among them, we can set one of the voltages as zero without any loss of generality. Here we set $V_2 = 0$. Finally, if we assume that the leads are connected to a geometrically symmetric ordered bridge, so, $\frac{V_3}{V_1} = \frac{V_4}{V_1} = \frac{1}{2}$. Now from Eq.(3.15) and Eq.(3.12) we can write the expression of spin Hall conductance as,

$$G_{SH} = \frac{e}{8\pi}\left(T_{13}^{out} + T_{43}^{out} + T_{23}^{out} - T_{34}^{in} - T_{31}^{in}\right) \tag{3.23}$$

Similarly, from Eq.(3.11) and Eq.(3.13), the expression of longitudinal conductance can be written as,

$$G_L = \frac{e^2}{h}\left(T_{21} + \frac{1}{2}T_{32} + \frac{1}{2}T_{42}\right) \tag{3.24}$$

We define the spin Hall conductance fluctuation as,

$$\Delta G_{SH} = \sqrt{\langle G_{SH}^2\rangle - \langle G_{SH}\rangle^2} \tag{3.25}$$

where $\langle ... \rangle$ denotes averaging over an ensemble of samples with different configurations with disorder strength W.

3.2 Results and discussion

We have investigated the interplay of disorder (W) and ROSC (α) on the experimentally measurable quantities such as longitudinal conductance (G_L), spin Hall conductance (G_{SH}) and spin Hall conductance fluctuation (ΔG_{SH}). The results are likely to be relevant for systems with spin-orbit interactions and since the disorder is an indispensable ingredient in crystal lattices, a competition between W and α will reveal whether they help each other or hinder with regard to the conductance properties of junction devices. An important question in this regard is whether there is any shift in the localization phenomenon in two dimensions induced by the RSOC[118]. More concretely, is there a transition to a metallic state at some critical value of the strength of RSOC?

Before we start computing the physical quantities, we briefly describe the values of different parameters used in our calculation. Throughout our work, we have considered lattice constant, $a = 1$, system size, $L = 20$, onsite term, $\epsilon = \epsilon_L = 0$, hopping term, $t = t_L = t_C = 1$. All the energies are measured in the unit of t. Further we choose a unit where $c = h = e = 1$. The longitudinal conductance, G_L is measured in unit of $\frac{e^2}{h}$. The spin Hall conductance, G_{SH} is measured in unit of $\frac{e}{8\pi}$. It is of relevance to mention here that we have considered bigger system sizes as well for our computation of the conductance properties, however, they do not yield any new information than those required for our purpose. Hence we have decided to show all our numerical computation for $L = 20$. The above inference is supported by Fig.3.4 which shows the longitudinal conductance and the spin Hall conductance as a function of the lateral dimension, L of the system.

The random onsite disorder is modeled by a rectangular distribution of the form,

$$P(\epsilon_i) = \frac{1}{2W} \quad \text{where,} \quad -\mathrm{W} \leq \epsilon_\mathrm{i} \leq \mathrm{W} \tag{3.26}$$

Here W has the dimension of energy and hence is expressed in terms of the hopping energy, t. All the results obtained below are averaged over 10000 disorder configurations.

To remind ourselves we have compared all of the above quantities at a fixed value of energy, namely $E = -2t$. However, it should be noted that G_{SH} has an antisymmetric nature as a function of E (Fermi energy) and hence as a result at $E = 0$, G_{SH} identically vanishes[135,136].

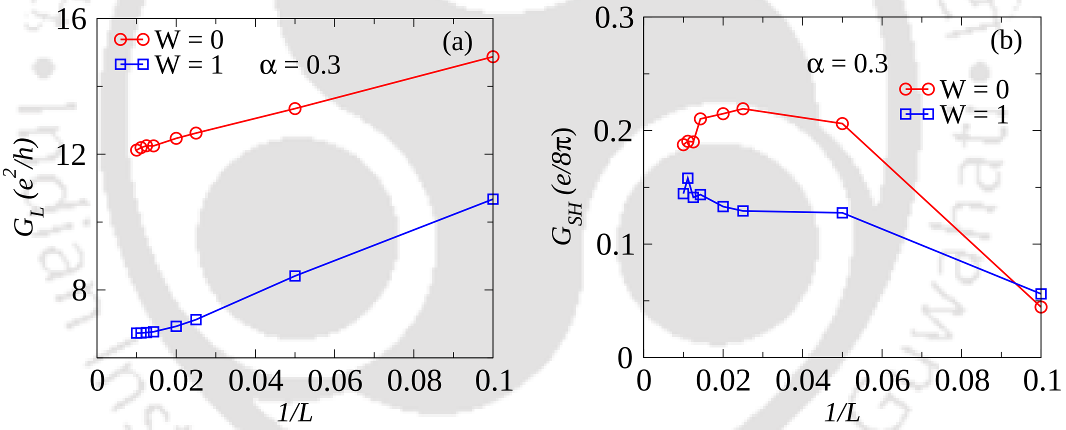

Figure 3.4: The effect of the system length (lateral dimension), L on the conductance properties is plotted at Fermi energy, $E = -2t$ in presence of Rashba SOC with $\alpha = 0.3$. (a) Longitudinal conductance, G_L. (b) Spin Hall conductance, G_{SH}. The width of the system is kept fixed at $10a$ (a: lattice spacing). The variations in the longitudinal and the spin Hall conductances are suppressed for $L \geq 20$. The plots are shown for the disorder free case ($W = 0$) and in presence of disorder ($W = 1$).

There is another small point that deserves a mention. We have investigated G_L, G_{SH} and ΔG_{SH} both over a small range of the RSOC, that is with $[0 : 1]$ and also over a much broader range, namely up to $\alpha = 8$. Of course, the former is a subset of the latter, but the behaviour of the physical quantities under consideration show qualitatively different behaviour in the two regimes and thus warrant separate discussion.

3.2.1 Longitudinal conductance

The longitudinal conductance, G_L is plotted as a function of the Fermi energy, E in the absence and also in presence of disorder with disorder strength, $W = 1$ as shown in Fig.3.5. The Rashba SOC strength is taken as, $\alpha = 0.5$. Both the plots are symmetric as a function of the Fermi energy. In the presence of disorder, G_L decreases significantly.

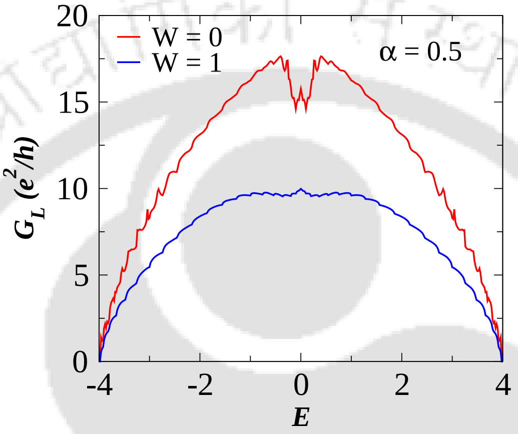

Figure 3.5: The longitudinal conductance, G_L (in units of e^2/h) is plotted as a function of the Fermi energy E (in units of t) for a fixed RSOC strength, $\alpha = 0.5$. The disorder free case is denoted by red colour. The other curve (blue) corresponds to a disorder strength, $W = 1$ (in units of t).

In a tight binding model for a two dimensional square lattice, the energy band width (BW) is 8 (-4 to 4 in units of t). Here we set range for the disorder strength to be the interval $\left[0, \frac{BW}{2}\right]$ that is $[0, 4]$, while for the RSOC strength, α to be in $[0, BW]$ or $[0, 8]$.

The variation of G_L as a function of W for different α is shown in Fig.3.6. In this figure we have considered for $\alpha = 0.1$, 0.3 and 1.0. As expected, G_L falls off with disorder. However the fall off at lower values of α (e.g. $\alpha = 0.1$ and 0.3) at large disorder is more than the corresponding values at large α (e.g. $\alpha = 1$). The trend was reverse at lower values of disorder where there is a crossover at $W \approx 1.5$. For example, $G_L = 2.5$ (in units of $\frac{e^2}{h}$) at $W \approx \frac{BW}{2} (= 4)$ for $\alpha = 1$ while the corresponding value is almost 1.2 for $\alpha = 0.1$.

The inference that can be drawn is larger RSOC aides in enhancing the conductance values at larger disorder. However, whether this enhancement has got anything to do with a transition to a conducting phase is yet to be seen.

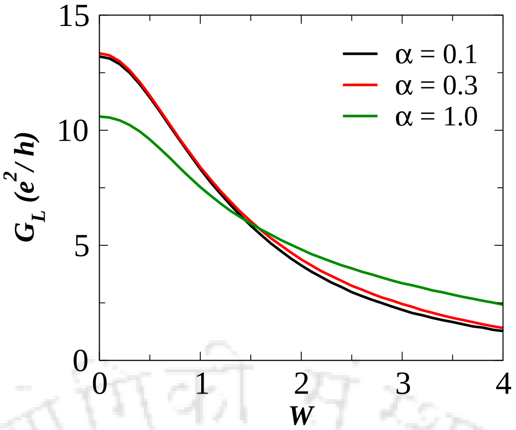

Figure 3.6: The longitudinal conductance, G_L (in units of e^2/h) is plotted as a function of disorder strength W (in units of t) for different RSOC strengths, α. Here we consider lower values of α, namely α in the region $[0:1]$. The plots cross at $W \approx 1.5$. All data in this figure and all subsequent figures averaged over 10000 disorder configuration.

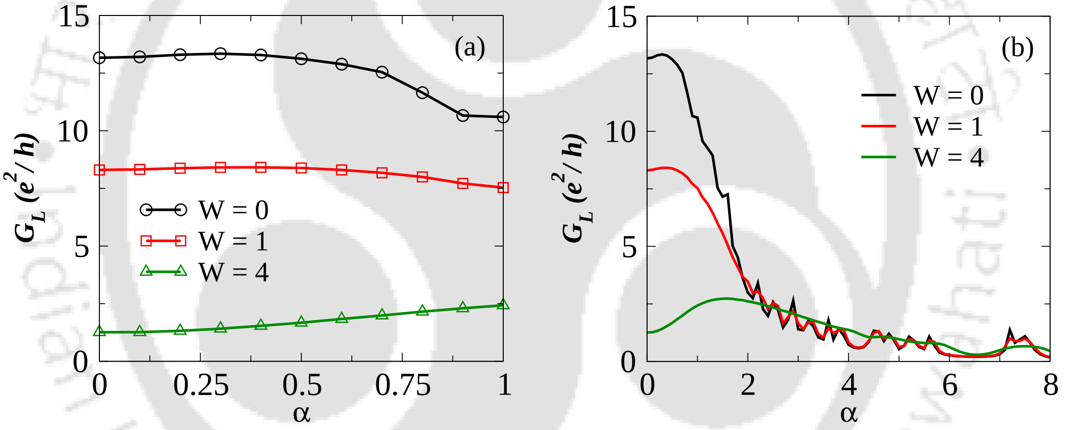

Figure 3.7: (a) G_L is plotted as a function of RSOC strength α (in units of t) for different disorder strengths (W). Here α is varied between $[0:1]$. G_L has weak dependence at lower values of α. (b) G_L is plotted as a function of RSOC strength, α for different disorder strengths, W. Here we take the range of α as $[0 : BW]$ (BW : Band width = 8(in units of t)). G_L decreases with increasing the strength of RSOC.

The variation of G_L as a function of RSOC strength, α for different disorder strengths are shown in Fig.3.7. In Fig.3.7(a), initially α is varied over a small range, namely $[0:1]$. We observe that in this regime, G_L is not strongly dependent on α for the values of disorder that we have considered, namely $W = 1$ and 4. The disorder free case is included for comparison.

However Fig.3.7(b) shows G_L being plotted for a much wider range of α, namely $\alpha = 0$ to $BW(= 8)$. In this figure, the longitudinal conductance decreases with increasing α and at higher values of α, G_L becomes vanishingly small. Thus in this

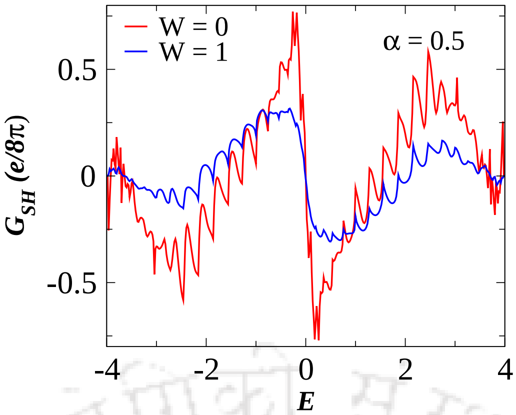

Figure 3.8: The spin Hall conductance, G_{SH} (in units of $e/8\pi$) is plotted as a function of the Fermi energy E (in units of t) for a fixed RSOC strength, $\alpha = 0.5$ in the absence of disorder denoted by red color. The other curve (blue) is for the case of disorder strength, $W = 1$. Clearly, the spin Hall conductance is antisymmetric.

regime, α destroys longitudinal conductance just as the disorder does. Physically, this means that large values of α denote strongly correlated hopping anisotropies, where the hopping strengths are all different along $\pm x$ and $\pm y$ directions (see Eq.(3.6)). This emulates disorder effects for the charge carriers where they see a different environment with regard to hopping to neighbouring sites.

3.2.2 Spin Hall conductance

The behaviour of the spin Hall conductance, G_{SH} is plotted as a function of the Fermi energy as shown in Fig.3.8. Here we fixed the Rashba SOC strength at, $\alpha = 0.5$. Both in absence and presence of disorder, G_{SH} is antisymmetric as a function of the Fermi energy about $E = 0$, which says that G_{SH} vanishes at $E = 0$. The antisymmetric nature of G_{SH} is due to the electron-hole symmetry of the system. The overall magnitude of G_{SH} decreases in presence of disorder.

We study the spin Hall conductance, G_{SH} as defined by Eq.(3.12) in presence of disorder, W and spin-orbit coupling, α. Fig.3.9 shows the variation of G_{SH} as a function of disorder strength, W for different values of α. Overall, G_{SH} decreases with increasing disorder strength for the same reason as mentioned earlier. For $\alpha = 0.1$ and 0.3, G_{SH} starts from positive values and subsequently vanishes as we increase W. While for $\alpha = 1.0$, G_{SH} starts from a negative value and vanishes at large W. There is a difference with the corresponding data for the longitudinal conductance, G_L which remains finite at large disorder.

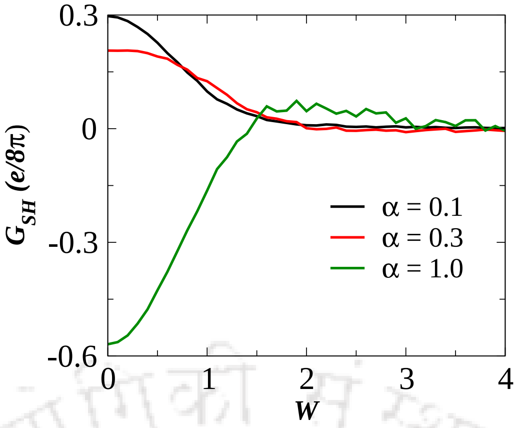

Figure 3.9: The spin Hall conductance, G_{SH} (in units of $e/8\pi$) is plotted as a function of disorder strength, W for different RSOC strengths, α. G_{SH} decreases as the disorder strength, W is increased.

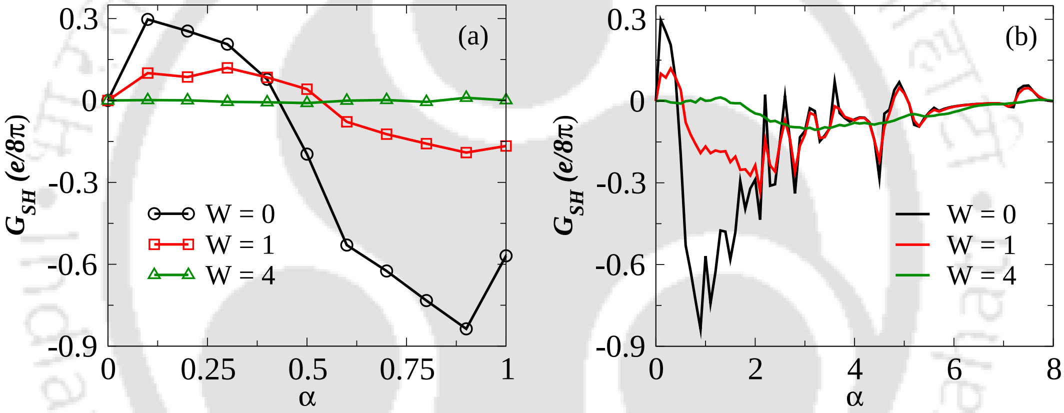

Figure 3.10: Spin Hall conductance, G_{SH} is plotted as a function of RSOC strength α for $W = 0$, 1 and 4. (a) α is varying from [0 : 1]. (b) α is varying over a much wider range, that is between [0 : 8].

Fig.3.10 shows the variation of G_{SH} as a function of α for different values of W. In Fig.3.10(a), we have plotted G_{SH} for a small range of α, namely between [0 : 1]. As expected, for the pure case ($W = 0$), G_{SH} has a maximum value (in magnitude). As disorder is introduced, the spin Hall conductance decreases. In Fig.3.10(b), G_{SH} is plotted for a wider range of α. It is in tune with the results for longitudinal conductance that at higher values of α, G_{SH} becomes almost zero. However G_{SH} seem to be strongly affected by disorder. At $W = 4$, for all values of α, $G_{SH} \approx 0$.

It has been proved that for an infinite system, the spin Hall conductance is strictly zero in presence of RSOC for any non-vanishing disorder strength[137]. The vanishing of SHC originates from the stationary nature of the system in presence of an applied electric field[138]. Here we have considered a central scattering region

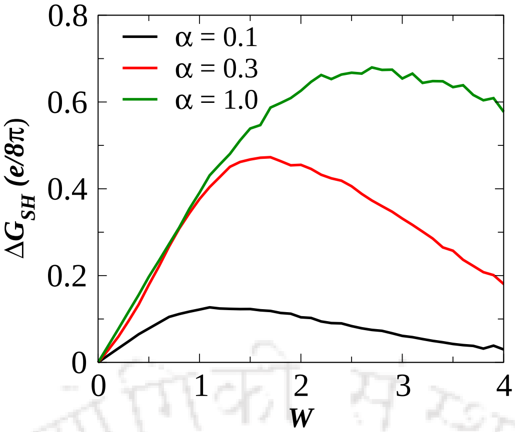

Figure 3.11: (a) ΔG_{SH} (in units of $e/8\pi$) is plotted as a function of disorder strength W for different RSOC strengths, α. ΔG_{SH} shows a non monotonic behaviour with disorder, W.

which is a square with system size, $L = 20$ and thus we can say that the non-zero SHC is an artifact of finite-size effects. However, since experiments on coherent quantum transport would invoke finite-size systems and hence their corresponding effects will be present and one would get a non-zero signal for the SHC.

3.2.3 Spin Hall conductance fluctuation

As said earlier, the spin Hall conductance fluctuation attains a finite constant value which is independent of material properties. It is thus of importance to see how this otherwise constant value responds to disorder and RSOC.

In Fig.3.11(a), ΔG_{SH} (in unit of $\frac{e}{8\pi}$) is plotted as a function of W for different values of α. As we increase α the fluctuation also increases. For each value of α and at lower values of W, it may be noted that ΔG_{SH} increases linearly, and hence it reaches a maximum value. Beyond this, ΔG_{SH} decreases with increasing W, yielding a non-monotonic behaviour[128].

Fig.3.12 shows the variation of ΔG_{SH} as a function of α for different values of the disorder strength. In Fig.3.12(a), for small disorder values, that is, $W = 0.5$ and 1, ΔG_{SH} tends to saturate at values, namely 0.2 and 0.4 respectively. As we increase the disorder strength, the fluctuation also increases and the corresponding plot shows the absence of any saturation upto $W = 4$. In Fig.3.12(b), we have shown the variation of ΔG_{SH} for a wider range of α, which shows a non-monotonic behaviour, beyond $\alpha \approx 1$ and ultimately vanishing at large values of α, albeit not without fluctuation. Further the plots corresponding to lower values of disorder (e.g. $W = 0.5$ and 1, as compared to $W = 1$) show suppressed fluctuations.

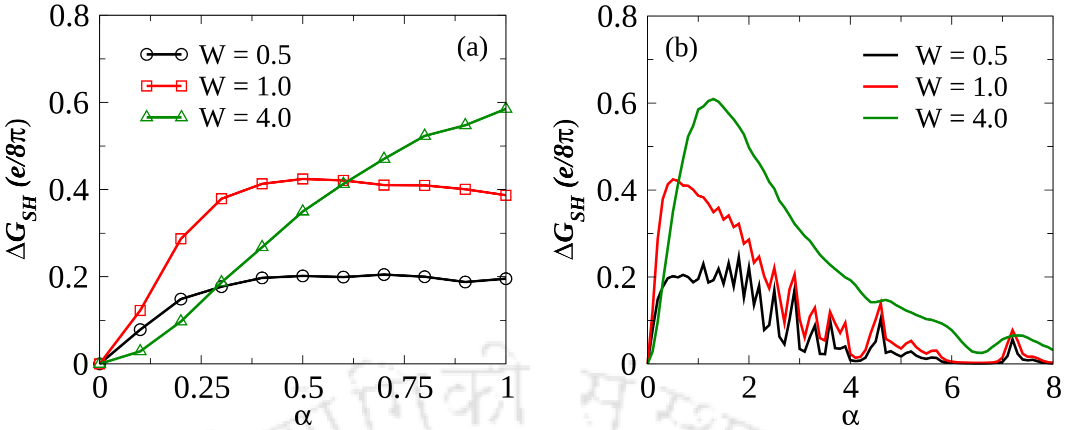

Figure 3.12: (a) ΔG_{SH} is plotted as a function of RSOC strength α for $W = 0.5$, 1 and 4 for a small range of α, that is between $[0 : 1]$. (b) ΔG_{SH} is plotted as a function of RSOC strength α for a much wider range, namely between $[0 : 8]$.

It may be noted that in the fluctuation in spin Hall conductance as a function of the strength of RSOC or disorder, we did not find any '*universal*' value. Hence ΔG_{SH} depends on the disorder strength, W and the strength of the RSOC, α.

3.2.4 One parameter scaling theory

It may be noted that the following observations were made in Fig.3.7, that the longitudinal conductance, G_L is seen to increase at larger disorder $\left(W \sim \frac{B}{2}\right)$ as α increases. At $\alpha = 1$, G_L is greater than that corresponding to other lower values of α. This enhancement in conductance whether signals a transition to a metallic phase as hinted in Ref.[118] is to be assessed. To arrive at a conclusion we perform a one parameter scaling theory[94]. For that, we study the variation of β as a function of $1/G_L$ in presence of RSOC and random onsite disorder. The results are shown in Fig.3.13. In Fig.3.13(a), β is plotted as a function of $1/G_L$ for two different disorder strengths, namely, $W = 1$ and 3, where we have assumed a very low value for α, such as 0.05. To ascertain whether the same scenario persists at a different RSOC strength, we have considered a somewhat larger value of $\alpha(= 1.0)$ in Fig.3.13(b). In both Fig.3.13, the maximum of β attain values close to zero, however there is no crossing of the dashed line ($\beta = 0$) in Fig.3.13. β becoming positive would have indicated a transition to a metallic phase as the conductance directly scaling with system size is a typical signature for the presence of extends states and hence metallic behaviour. Hence we disagree on the onset of a metallic regime at a certain critical disorder strength for a given value of the spin-orbit coupling parameters as suggested by Sheng et. al.[118].

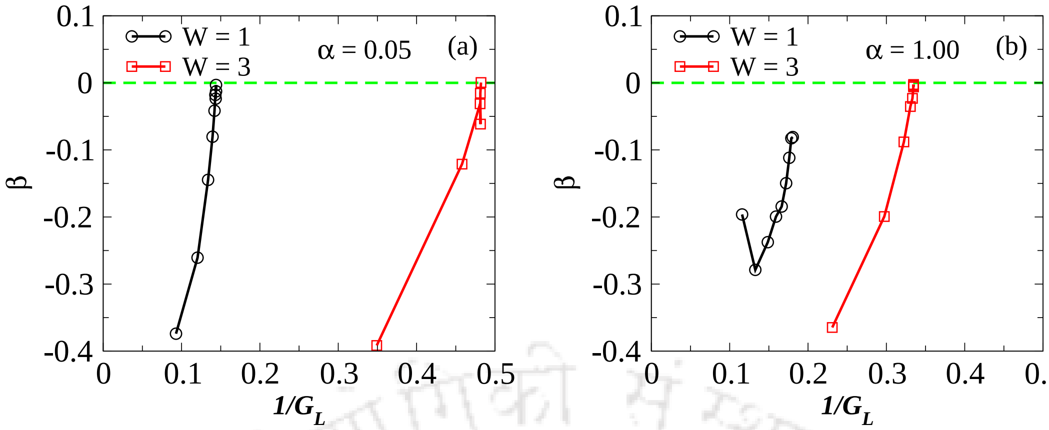

Figure 3.13: β is plotted as a function of $1/G_L$. (a) $\alpha = 0.05$, (b) $\alpha = 1.0$. In both the figures, the strengths of disorder, W are 1 and 3. The plots do not cross the dashed line ($\beta = 0$) and always remain negative.

3.3 Conclusion

In summary, in the present work, we have studied the interplay of random onsite disorder, W and the strength of RSOC, α on the conductance properties of a four-probe junction device. Both these factors destroy the longitudinal (G_L) and spin Hall conductances (G_{SH}) for the parameter regime that we have considered in our work, namely $0 \leq W \leq \frac{BW}{2}$ and $0 \leq \alpha \leq BW$ (BW: bandwidth $= 8t$). For lower values of α ($0 \leq \alpha \leq 1$), G_L shows weak dependence on α and vanishes at large values of α. Further, G_L diminishes as the disorder is increased: larger α registers a higher conductance at strong disorder ($W = 4$).

The spin Hall conductance, G_{SH} is more strongly affected by disorder (than G_L) which vanishes at $W \approx 1.5$ and again a larger α yields larger conductance at low disorder. Further G_{SH} shows an antisymmetric behaviour for $0 \leq \alpha \leq 1$, while it vanishes at larger α, albeit with some fluctuations. These fluctuations remain even after the configuration averaging being done over 10000 disorder realizations.

Further, the spin Hall conductance fluctuations, ΔG_{SH} do not have a universal nature and shows strong dependencies on W and α, all the while remaining lower than its universal value $\frac{e}{8\pi}$.

Finally, we do not get any convincing evidence for a RSOC induced transition to a metallic state and we feel that it is a physically meaningful result as the RSOC does not break the time reversal symmetry, a crucial condition for the weak localization to occur, which however could have been a different scenario if an external magnetic field would have been present.

Chapter 4

Conductance characteristics of a Y-shaped junction

After prediction and detection of the spin Hall effect[121,122,139,140] (SHE), the spin-dependent electronic transport has been a central focus of investigation in mesoscopic physics because of its possible applications to spintronics[25,141]. Generation of dissipationless spin current[37] is one of the features that is believed to be crucial in this respect. In early attempts, generation of spin-polarized currents were obtained by attaching ferromagnetic metallic contacts to the semiconductors[25,33]. But, the efficiency of the spin injection from a ferromagnet into a semiconductor is poor because of the conductivity mismatch[26] between the two. This drawback can be overcome by producing spin-polarized current intrinsically. Here comes the role of spin-orbit (SO) interaction. A strong spin-orbit scattering generates spin-polarized electrons intrinsically[27].

Geometry of the scattering region plays a crucial role in order to study effects of spin-polarization in presence of spin-orbit interaction. Four terminal junction devices have been studied in the last chapter, where unpolarized charge current is driven through the longitudinal leads attached to a semiconducting region with SO coupling induces a pure spin current at the transverse voltage probes without accompanying any charge current[142,143]. In particular, three terminal structures such as T-shaped[144], Y-shaped[81,145–147] devices have also been studied in presence of spin-orbit interaction. In a three terminal structure, one terminal acts as an input to the device, through which unpolarized charge current is injected into the device. The other two terminals act as outputs through which the spin-polarized currents flow out of the device.

Recent studies show that a Y-shaped zigzag graphene nanoribbon junction can be used to manipulate and detect spins using the valley-valve effect[79]. A Y-shaped multi-walled carbon nanotube can also have novel electrical switching behaviour, where any one of the three branches of the Y-junction can be used for modulating the electrical current flow through the other two branches[80]. Further, a three terminal ballistic junction with Y geometry can be used as an extremely compact multi-logic gate, the functionality of which may be tuned by means of a gate voltage[148].

Since a three terminal structure is a suitable candidate for studying the SHE, in this chapter, we have studied the behaviour of a special type of three terminal device with Y-shaped structure. Since the angular separation between the arms of the Y-shaped geometry can be relevant parameter for studying SHE, we have considered different angles as shown in Fig.4.1. Also because the rotational symmetry is broken in spin space in presence of the spin-orbit interaction, the spin quantization axes also play an important role in the context of SHE. Motivated by these, we have studied the effects of the angular variation and orientation of the spin quantization axes on the spin Hall conductance of such a Y-shaped junction with tunable SO interactions.

In general, two types of spin-orbit coupling terms can be present in semiconductor heterostructures. One of them is the Dresselhaus spin-orbit coupling (DSOC) which originates from the inversion asymmetry of the zinc blende type of structures[28] . The other is the Rashba spin-orbit coupling (RSOC) which originates due to the effective electric field originating from the asymmetry of the potential as has been highlighted in previous chapter[29]. The Dresselhaus term is found to be dominant in large bandgap materials and the strength can be controlled easily by tunning the quantum well width[30]. On the other hand, the Rashba term is dominant in narrow-gap systems where the strength of the Rashba term can be controlled by external gate voltages[31,32,149]. The interplay of both types of spin-orbit coupling on the conductance characteristics of nanostructures has been investigated both theoretically[118,135,150,151] and experimentally[152,153].

We organize this chapter as follows. In the following section, we present a prescription of fabricating a Y-shaped device. The theoretical formalism leading to the expression for the spin Hall conductance using Landauer-Büttiker formula are presented in the next section. Hence we include an elaborate discussion of the results obtained for the spin Hall conductance in presence of the SO interaction. We have included an interesting comparison for the conductance properties in presence of Rashba vis-a-vis Dresselhaus SO interactions. We finally conclude with a highlight of our main results.

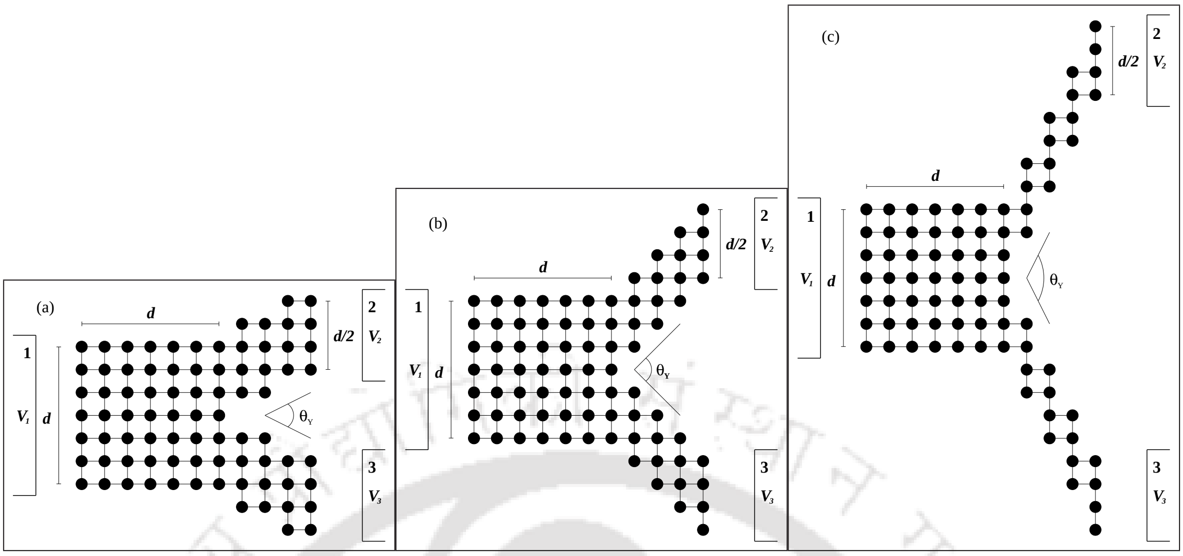

Figure 4.1: Y-shaped three terminal junction devices with three different angles (θ_Y). V_1, V_2 and V_3 are the applied voltages at the three terminals. The leads are not shown in the figure.

4.1 Fabrication of Y-shaped devices

We begin our discussion by a prescription of fabricating a Y-shaped junction device which should be interesting from an experimental perspective.

We choose a three-probe measuring set-up as shown in Fig.4.1 to observe the spin Hall effect. Here the three ideal semi-infinite leads are attached to the central conducting region, which in our case is the Y-shaped device having a square lattice geometry and includes spin-orbit interaction. The leads denoted by 1, 2 and 3 are semi-infinite in nature. The voltages applied to the leads are V_1, V_2 and V_3 respectively. The width of the scattering region is d, while the arms has width $d/2$ (see Fig.4.1). In this chapter, we have taken three Y-shaped devices by changing the angular separation between the two arms of the Y, and call it θ_Y as shown in Fig.4.1.

Fig.4.2 provides a technique of how one can fix the angle, θ_Y. According to Fig.4.1, θ_Y is twice the angle as shown in Fig.4.2. For the Y-shape shown in Fig.4.1(a), we add the lattice sites in the arms of Y as depicted in Fig.4.2(a). First, we add three sites along x-axis with a spacing 'a' and then add another site along y-axis just above the third site along the x direction. We repeat the same procedure to build up the rest of the arm of the Y-geometry. Since we need three sites along x-axis and two sites along y-axis we call it a (3,2) scheme. The calculation of the angle in now straightforward from the geometry. From Fig.4.2, b is the base of the

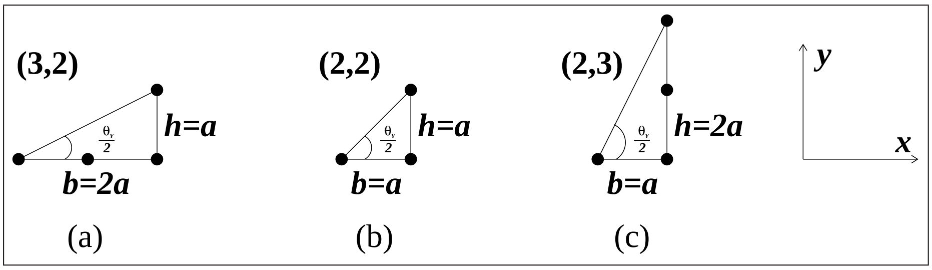

Figure 4.2: Measurement of the angle between the two arms of the Y-shaped device is shown. b is the base of the triangle and h is the height. a is the lattice constant. According to Fig.4.1, this angle is half of θ_Y as depicted in the given figure.

triangle and h is the height. In the (3,2) scheme, $b = 2a$ and $h = a$. Hence, the angular separation between the arms of the Y will be twice the calculated angle and is, $\theta_Y = 2\tan^{-1}\frac{a}{2a} = 53.13°$. Similarly, corresponding to $\theta_Y = 90°$, we need the (2,2) scheme, for which two sites along x-axis and one site along y-axis above the second site along x are required, as shown in Fig.4.2(b). In the given case, $\theta_Y = 2\tan^{-1}\frac{a}{a} = 90°$. To obtain an angle, θ_Y greater than 90°, we adopt (2,3) scheme as shown in Fig.4.2(c). Here, $\theta_Y = 2\tan^{-1}\frac{2a}{a} = 128.87°$. We are going to consider only these three geometries for computing the conductance spectra in this chapter, however, it is possible to generate a number of other values for the angular separation, θ_Y by following the prescription given above.

4.2 Theoretical formulation

4.2.1 System and Hamiltonian

The single particle Hamiltonian in presence of both Rashba and Dresselhaus spin-orbit interaction in a two-dimensional electron system is given by,

$$H = \frac{\mathbf{p}^2}{2m^*} + \frac{\alpha}{\hbar}\left(\sigma_x p_y - \sigma_y p_x\right) + \frac{\beta}{\hbar}\left(\sigma_x p_x - \sigma_y p_y\right) \tag{4.1}$$

where $\mathbf{p}$ $(= p_x,\ p_y)$ is the two dimensional momentum operator, m^* is the effective mass, σ_x and σ_y are the components of the Pauli matrices. α and β respectively denote the Rashba and Dresselhaus spin-orbit coupling strengths.

We now discretize the Hamiltonian (Eq.(4.1)) via a tight binding approximation with the nearest neighbour hopping on a two-dimensional square lattice. The resulting Hamiltonian becomes,

$$\begin{aligned} H &= \epsilon \sum_{i,\sigma} c^{\dagger}_{i\sigma} c_{i\sigma} + t \sum_{\langle ij \rangle,\sigma} c^{\dagger}_{i\sigma} c_{j\sigma} \\ &+ V_R \sum_i \left[\left(c^{\dagger}_{i\uparrow} c_{i+\delta_x\downarrow} - c^{\dagger}_{i\downarrow} c_{i+\delta_x\uparrow} \right) - i \left(c^{\dagger}_{i\uparrow} c_{i+\delta_y\downarrow} + c^{\dagger}_{i\downarrow} c_{i+\delta_y\uparrow} \right) \right] \\ &+ V_D \sum_i \left[(-i) \left(c^{\dagger}_{i\uparrow} c_{i+\delta_x\downarrow} + c^{\dagger}_{i\downarrow} c_{i+\delta_x\uparrow} \right) + \left(c^{\dagger}_{i\uparrow} c_{i+\delta_y\downarrow} - c^{\dagger}_{i\downarrow} c_{i+\delta_y\uparrow} \right) \right] \end{aligned} \tag{4.2}$$

Here ϵ is the on-site potential and $t = \hbar^2/2m^*a^2$ is the hopping strength, $V_R = \alpha/a$ and $V_D = \beta/a$ are the Rashba and Dresselhaus coupling strengths respectively, a being the lattice constant. $\delta_{x/y}$ is the unit vector along x/y direction.

It is assumed that the Rashba and Dresselhaus SO interactions are present only in the Y-shaped device. The leads are metallic and semi-infinite in nature. The leads are free from any kind of SO interactions so as to avoid any kind of spin flips at the boundaries.

4.2.2 Formulation spin Hall conductance

Since the rotational symmetry in spin space is lost in presence of spin-orbit interaction, the quantization axes of the spin play a vital role in measuring spin current. Hence we choose the spin quantization axis along an arbitrary direction, say $\hat{\mathbf{u}}$, denoted by $\hat{\mathbf{u}} = \sin\theta\cos\phi, \sin\theta\sin\phi, \cos\theta$, where θ and ϕ are the usual spherical angles.

Now we proceed to evaluate the expression for spin Hall conductance. In order to get a pure spin current, we treat terminal 2 as a voltage probe (Fig.4.1). As a result a pure spin current will flow through terminal 2, due to the flow of charge current between terminals 1 and 3. For the three terminal Y-shaped geometry, the longitudinal and spin Hall conductances are defined as[131],

$$G_L = \frac{I^q_3}{V_3 - V_1} \tag{4.3}$$

$$G_{SH} = \frac{\hbar}{2e} \frac{I^s_2}{V_2 - V_1} \tag{4.4}$$

where I^q_3 and I^s_2 are the charge and spin currents flowing through the lead-3 and lead-2 respectively. V_m is the potential at the m-th lead.

The calculation of the electric and spin currents is based on the Landauer-Büttiker multi-probe formalism[132]. For completeness, we re-iterate the main working formulae for our numeric computation of the conductance. The charge and spin currents flowing through lead m ($m = 1, 2, 3$) with potential, V_m can be written in terms of the spin resolved transmission probability as[81],

$$I_m^q = \frac{e^2}{h} \sum_{n \neq m, \sigma, \sigma'} \left(T_{nm}^{\sigma\sigma'} V_m - T_{mn}^{\sigma'\sigma} V_n \right) \tag{4.5}$$

and,

$$\begin{aligned} I_m^s &= \frac{e^2}{h} \sum_{n \neq m, \sigma'} \left[\left(T_{nm}^{\sigma'\sigma} - T_{nm}^{\sigma'-\sigma} \right) V_m + \left(T_{mn}^{-\sigma\sigma'} - T_{mn}^{\sigma\sigma'} \right) V_n \right] \\ &= \frac{e^2}{h} \sum_{n \neq m} \left[T_{nm}^{out} V_m - T_{mn}^{in} V_n \right] \end{aligned} \tag{4.6}$$

where, we have defined two useful quantities as in the following,

$$\begin{aligned} T_{pq}^{in} &= T_{pq}^{\uparrow\uparrow} + T_{pq}^{\uparrow\downarrow} - T_{pq}^{\downarrow\uparrow} - T_{pq}^{\downarrow\downarrow} \\ T_{pq}^{out} &= T_{pq}^{\uparrow\uparrow} + T_{pq}^{\downarrow\uparrow} - T_{pq}^{\uparrow\downarrow} - T_{pq}^{\downarrow\downarrow} \end{aligned} \tag{4.7}$$

Physically, the term $\frac{e^2}{h} \sum_{n \neq m} T_{nm}^{out} V_m$ is the total spin current flowing out from the m-th lead with potential V_m to all other n leads, while the term $\frac{e^2}{h} \sum_{n \neq m} T_{mn}^{in} V_n$ is the total spin current flowing into the m-th lead from all other n leads having potential V_n.

Now following the spin Hall phenomenology in our set-up, since lead-2 is a voltage probe, $I_2^q = 0$. Also, as the currents in various leads depend only on voltage differences among them, we can set one of the voltages to zero without any loss of generality. Here we set $V_1 = 0$ and $V_3 = 1$. With the help of these conditions, from Eq.(4.5), one can determine the voltage, V_2 as,

$$V_2 = \frac{T_{23}}{T_{12} + T_{32}} \tag{4.8}$$

Further, the spin current flowing through terminal 2 (from Eq.(4.6)) is,

$$I_2^s = \frac{e^2}{h} \left[\left(T_{12}^{\text{out}} + T_{32}^{\text{out}} \right) V_2 - T_{23}^{\text{in}} \right] \tag{4.9}$$

Finally, from Eq.(4.3) and Eq.(4.4)the expressions for the longitudinal and spin Hall conductances become,

$$G_L = \frac{e^2}{h}\left[(T_{13}+T_{23}) - \frac{T_{23}T_{32}}{T_{12}+T_{32}}\right] \tag{4.10}$$

$$G_{SH} = \frac{e}{4\pi}\left[\left(T_{12}^{\text{out}}+T_{32}^{\text{out}}\right) - T_{23}^{\text{in}}\frac{T_{12}+T_{32}}{T_{23}}\right] \tag{4.11}$$

Eqs.(4.11) are the working formulae required to obtain the conductance properties for our Y-shaped device.

4.3 Results and discussion

We have investigated the effects of the angle variation of the Y-shaped junction in presence of Rashba and Dresselhaus SO couplings on the experimentally measurable quantities, namely the longitudinal conductance (G_L) and spin Hall conductance (G_{SH}). We have also studied the effect of the orientation of the quantization axis of spin on the spin Hall conductance.

We briefly describe the values of different parameters used in our calculation. Throughout our work, we have considered for the Y-shaped system, $d = 20$ in units of the lattice spacing 'a' which is taken to be unity (see Fig.4.1), onsite term, $\epsilon = 0$, hopping term, $t = 1$. All the energies are measured in the unit of t. Further we choose a unit where $c = h = e = 1$. The longitudinal and spin Hall conductances are measured in units of e^2/h and $\frac{e}{4\pi}$ respectively. For most of our numerical calculations, we have used KWANT[93].

From the experimental perspective, we now include a brief discussion on the realistic values of the SO couplings, observed in materials. In GaAs, the effective mass, $m^* = 0.067m_0$ and the lattice constant, $a = 0.5653$ nm. With these values, the hopping integral becomes $t \simeq 1.8$ eV (from the discussion following Eq.(4.2)). Also in InAlAs/InGaAs it is found that the Rashba parameter is, $\alpha \sim 0.67 \times 10^{-11}$ eV-m[31,152]. Then in our case, $V_R = \alpha/a \simeq 0.01$ eV. Since we are denoting all the energy units in terms of t, $V_R/t \simeq 0.006$. Which is pretty small. However, recently, in topological insulators such as Bi_2Se_3, the Rashba coupling parameter is found out to be $\sim 4 \times 10^{-10}$ eV-m[154], polar semiconductor such as BiTeI shows a bulk Rashba coupling parameter $\sim 3.85 \times 10^{-10}$ eV-m[155]. With such high values of α, one gets $V_R/t \simeq 0.4$, which may be considered to order of unity and precisely similar in magnitude to what has been used in our work. In fact, we have considered the Rashba and Dresselhaus coupling parameters in the interval $[0:1]$. In fact, there are recent proposal to enhance the value of the Rashba coupling in InAs nanowire by a factor of 2 by using a doubly gate device and a factor by 6 via gating through a solid electrolyte, polyethylene oxide (PEO). In the electrolyte gating, the Rashba coupling strength is achieved upto, $\alpha \sim 0.5 - 3 \times 10^{-11}$ eV m[149].

Further, in this work, we have taken three different angles for the Y-shaped device, such as θ_Y values to be less than, equal to and greater than 90°. in particular, we have considered, $\theta_Y = 53.13°$, $90°$ and $128.87°$ as elaborated earlier.

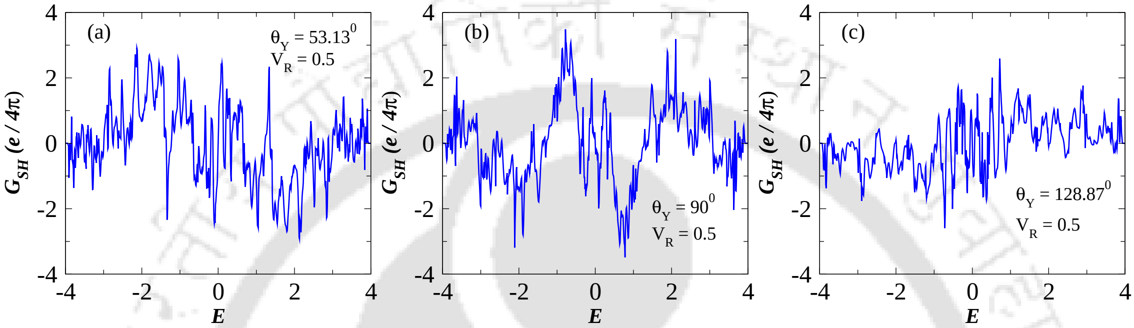

Figure 4.3: (a) G_{SH} is plotted as a function of energy, E for three different values of θ_Y in presence of RSOC. (a) $\theta_Y = 53.13°$, (b) $\theta_Y = 90°$ and (c) $\theta_Y = 128.87°$.

The effect of the angular separation between the arms of the Y-shaped device on the spin Hall conductance, G_{SH} is shown in Fig.4.3. Here G_{SH} is plotted as a function of energy, E in presence of RSOC. G_{SH} is antisymmetric as a function of E, an important feature of the spin Hall conductance[118,134,135]. It can be noticed that for different values of θ_Y the variation of G_{SH} is different, all the while retaining the antisymmetric character.

We study the behaviour of the spin Hall conductance as a function of the spin quantization axes parameter, θ and ϕ. In Fig.4.4, we show the variation of G_{SH} as a function of the spin quantization axes in presence of Rashba SO coupling with strength, $V_R = 0.5$ for three different angles of the Y-shaped device. We set the Fermi energy to be at $E = -2t$. The nature of G_{SH} for the three plots in Fig.4.4 are clearly distinct from one another though the RSOC strength is the same. This is because of the difference in the angle, θ_Y, which introduces different scattering environment for the electrons.

In Fig.4.4(a), G_{SH} shows a reflection symmetry along the $\theta = \phi$ and $\theta = -\phi$ lines for $\theta_Y = 53.13°$. The color map in Fig.4.4(a) can be divided into four regions, namely I. ($\theta : 0° - 180°$, $\phi : 0° - 180°$), II. ($\theta : 0° - 180°$, $\phi : 180° - 360°$), III. ($\theta : 180° - 360°$, $\phi : 0° - 180°$) and IV. ($\theta : 180° - 360°$, $\phi : 180° - 360°$). At the center of the each region, G_{SH} has a periodic behaviour (circular patches) which

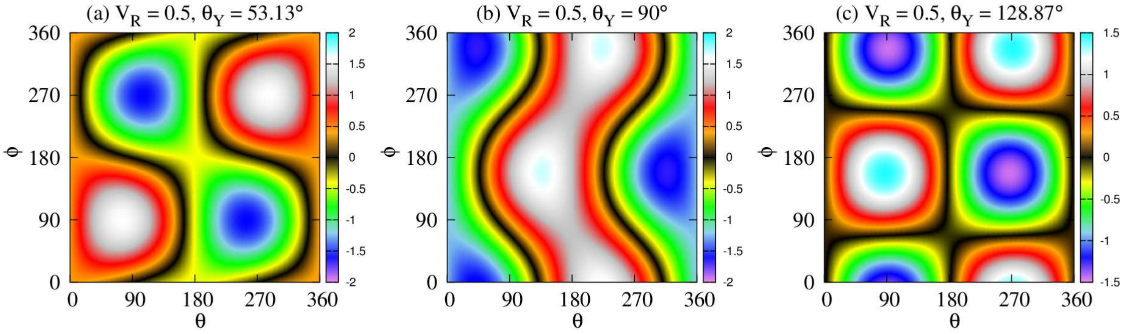

Figure 4.4: Spin Hall conductance, G_{SH} is plotted as a function of the parameters describing the spin quantization axes, namely θ and ϕ for a Fermi energy $E = -2t$ in presence of Rashba spin-orbit coupling with strength, $V_R = 0.5$.

can be seen from the coloured circles. This is reminiscent of the phase space plot for a simple harmonic oscillator. Here G_{SH} shows bounded trajectories as the spin quantization axis orientation changes. Further G_{SH} vanishes along the path that resembles the letter ‘S’ as shown in the figure.

In Fig.4.4(b), G_{SH} shows a different behaviour as a function of θ and ϕ for $\theta_Y = 90°$. For fixed values of ϕ, for lower values of θ, G_{SH} starts form negative values. It gradually increases to zero as θ increases. Finally in the vicinity of $\theta = 180°$, G_{SH} becomes positive emphasizing a spin rotational broken symmetry state. A different symmetry axis, namely, along the line $\phi \sim 180°$ emerges here.

For $\theta_Y = 128.87°$, the behaviour of G_{SH} is again different from the previous two plots as shown in Fig.4.4(c). Here we get few bounded regions and each region is separated by zero G_{SH} as shown by the dark black line. Along the three lines, namely $\theta = 0°$, $\theta = 180°$ and $\theta = 360°$, the value of G_{SH} is zero. An additional observation is that the magnitude of the spin Hall conductance is lower than the previous two cases. It is interesting to note that how the patterns in Fig.4.4 changes as the separation angles, θ_Y is varied. Intuitively, computing G_{SH} at an arbitrary angle (θ, ϕ) may be relevant where spin currents can be obtained for a particular orientation of the spin quantization axis.

It may also be interesting to look at different segments of the colour maps in Fig.4.4. For $\theta = 0°$ and $\theta = 180°$, G_{SH} is constant along the ϕ-direction. It may be noted that these are actually due to the spin current I_2^s, corresponding to the case when the spins are polarized along the positive and negative z-directions. While analyzing the polar angle dependencies of G_{SH}, in the range $0° < \theta < 180°$, for the azimuthal angle, ϕ to be such that it is in the range $0° < \phi < 180°$ and

$180^\circ < \phi < 360^\circ$, we find that the SHC satisfies the following symmetry relations.

$$\begin{aligned} G_{SH}(\theta = 90^\circ, \phi = 0^\circ) &= -G_{SH}(\theta = 90^\circ, \phi = 180^\circ) \\ G_{SH}(\theta = 90^\circ, \phi = 90^\circ) &= -G_{SH}(\theta = 90^\circ, \phi = 270^\circ) \\ G_{SH}(\theta = 0^\circ, \forall\phi) &= -G_{SH}(\theta = 180^\circ, \forall\phi) \end{aligned} \tag{4.12}$$

These features are true for all of the colour maps shown in Fig.4.4. Also, it can be noted that in Fig.4.4(a), G_{SH} becomes maximum (magnitude wise) in the two regions, one in the range $0^\circ < \phi < 180^\circ$ and the other in $180^\circ < \phi < 360^\circ$. However, for other values of the angular separation, θ_Y, the maximum value of G_{SH} occurs at different values of the angles θ and ϕ. Clearly, this is an effect which pertains to the geometry of the Y-shaped device.

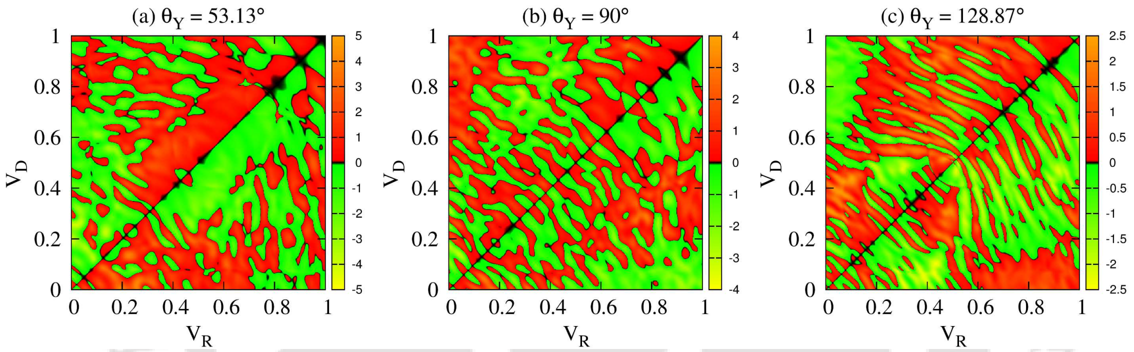

Figure 4.5: Spin Hall conductance, G_{SH} is plotted as a function of the spin-orbit interaction strengths, V_R and V_D for a Fermi energy $E = -2t$. A distinct (and familiar) antisymmetric behaviour is noted.

Let us now study the behaviour of spin Hall conductance as a function of Rashba and Dresselhaus spin-orbit interaction strengths, V_R and V_D respectively. In this case, we set the spin quantization axis along z direction, that is, we fixed (θ, ϕ) at $\theta = 90^\circ$ and $\phi = 0$. Fig.4.5 shows the variation of G_{SH} as a function of V_R and V_D. It may be noted that along the $V_R = V_D$ line, G_{SH} is zero, as seen by the black line and the behaviour of G_{SH} is antisymmetric with respect to the $V_R = V_D$ line. This behaviour is expected, because for $V_R = V_D$, a unitary transformation of the type, $\sigma_x \to \sigma_y$, $\sigma_y \to \sigma_x$ and $\sigma_z \to -\sigma_z$, the Rashba and the Dresselhaus terms get interchanged. Since the above transformations are pertaining only to the spin degree of freedom, G_{SH} will identically vanish corresponding to $V_R = V_D$ for the spin to be polarized along the z-axis and this feature arise because of this symmetry, one can also say that the z-component of the transverse spin current is conserved for $V_R = V_D$.

For the three different angles, θ_Y, there is an interesting feature if we look at the order of magnitude of G_{SH}. For $\theta_Y = 53.13°$, G_{SH} has the maximum value, while G_{SH} is minimum for $\theta_Y = 128.87°$. This is because of different values of θ_Y, causes different scattering environment for the electrons flowing through the leads 2 and 3. In this regard, the positions of the nearest neighbouring sites also play an important role. Since we are measuring the spin current at terminal 2, for a lower θ_Y, electrons reach terminal 2 more easily in comparison to larger values of θ_Y. In other words, the probability of getting scattered towards terminal 2 will be less for larger values of θ_Y. This explains G_{SH} to be small for $\theta_Y = 128.87°$ compared to $\theta_Y = 53.13°$ and $\theta_Y = 90°$.

The results discussed above have relevance to the spintronic applications, A larger angular separation impedes the usage of the Y-shaped system to have potential usage as a spintronic device.

Motivated by the experiments done on semiconductor quantum wells[156], where the realistic values of the ratio, γ $(= V_R/V_D)$ was discussed to be in the range $\sim 1.5 - 2.5$, we have studied the variation of G_{SH} as a function of V_R with $V_D = 0$ and vice versa to understand the effects of solely one type of SO interaction.The different parameters are taken as, $E = -2t$, $\theta_Y = 90°$ and the spin quantization is aligned along the z-axis $(\theta = 90°, \phi = 0)$ as shown in Fig.4.6(a) . There is a nice symmetry (differing by a negative sign) among the behaviour of SHC for the Rashba and Dresselhaus interactions. Also in Fig.4.6(b), we plot G_{SH} as a function of γ for a fixed V_D, that is, $V_D = 0.5$. For $V_R = V_D$, that is, $\gamma = 1$, $G_{SH} = 0$ as explained earlier. G_{SH} is seen to oscillate about its zero value. These oscillations are due to the finite-size effects, mainly originating from the presence of a finite number of open channels in the leads and may be due to the spin precession effect[157]. The latter manifests slow oscillations with large amplitudes.The qualitative behaviour of G_{SH} as presented in Fig.4.6 remains unchanged for a different θ_Y or for other values of the Fermi energy.

Now we focus on calculating the longitudinal conductance, G_L. If we look at the final expression for G_L (Eq.(4.11)), one can find that G_L is independent of the polar angles (θ, ϕ), since G_L is expressed in terms of the total transmission coefficients. Hence there is no variation of G_L as a function of (θ, ϕ). However, The variation of the longitudinal conductance G_L as a function V_R and V_D can be computed and are shown by the color plots in Fig.4.7. The variations of G_L in Fig.4.7 are completely different from one another, for different values of the angular separation, θ_Y. As we increase θ_Y, G_L decreases. This feature will be explained shortly.

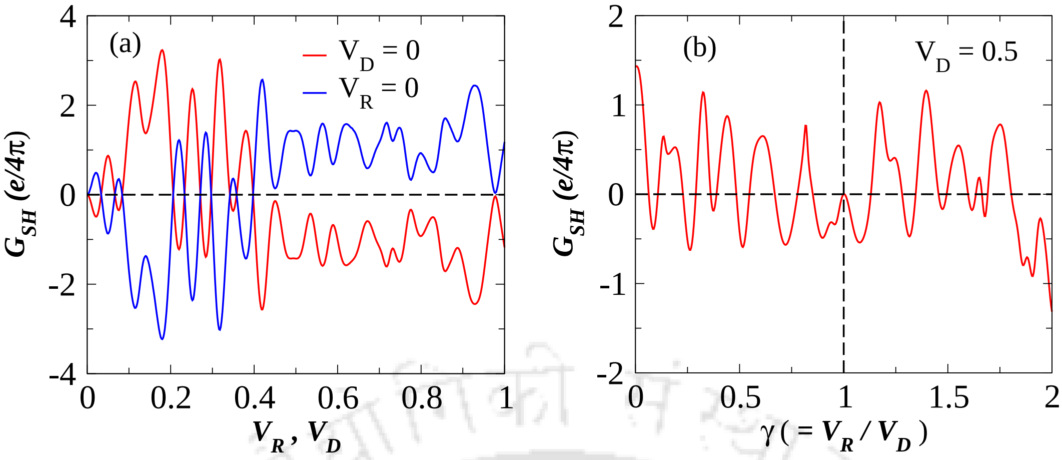

Figure 4.6: (a) Spin Hall conductance, G_{SH} is plotted as a function of V_R (red curve) and V_D (blue curve). (b) G_{SH} is plotted as a function of the ratio, γ $(= V_R/V_D)$. For $\gamma = 0$, G_{SH} is zero. The angular separation θ_Y is taken to be 90° here.

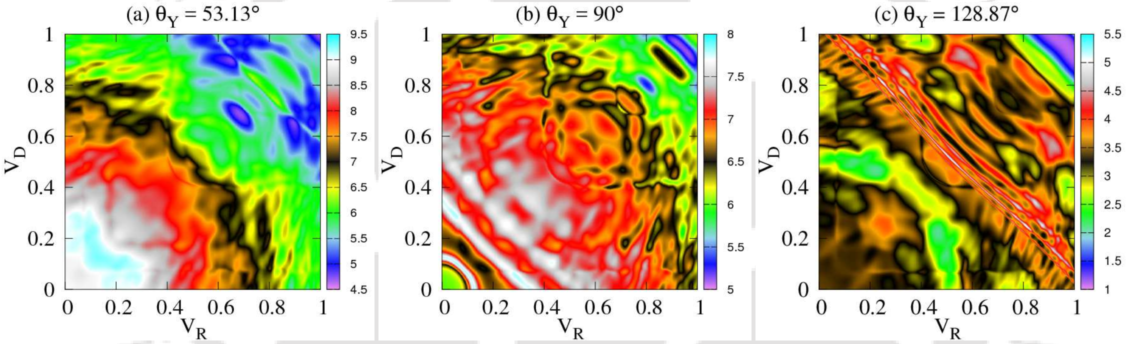

Figure 4.7: Longitudinal conductance, G_L is plotted as a function of the spin-orbit interaction strengths, V_R and V_D for a Fermi energy, $E = -2t$.

Fig.4.8 shows the variation of the longitudinal conductance as a function of the Fermi energy, E for three different angles of the Y-shaped device. In Fig.4.8(a), for $\theta_Y = 90°$, G_L, on an average, except for some fluctuations, shows step-like nature in absence of the RSOC, thereby demonstrating the discreteness of the energy states available for conduction. Another important observation is that the magnitude of G_L at $E = 0$ decreases with increase in the value of θ_Y. This can be explained in the following way. G_L is measured at terminal-3 and the charge current, I_3^q is flowing between terminals 3 and 1. Now it is easily understandable that as we increase the angle between terminal-1 and terminal-3, electrons are likely suffered more scattering in reaching terminal-3. Accordingly, G_L decreases as θ_Y is increased.

Fig.4.8(b) shows the variation of G_L as a function of E in presence of RSOC with $V_R = 0.5$. Here though the step-like nature is lost, but the decreasing trend of G_L persists with increasing θ_Y. An interesting observation from Fig.4.8(b) is that, for

$\theta_Y = 90°$, the longitudinal conductance vanishes at $E = 0$. This can be explained from the definition of G_L as given in Eq.(4.3) and Eq.(4.5). Since we have assumed the voltage at terminal-3, that is, $V_3 = 1$ and the voltage at terminal-1, $V_1 = 0$, by Eq.(4.3) G_L is the charge current flowing through terminal-3. It is clear that there is a vanishing of the charge current, I_3^q owing to the cancellation of the two given terms, in Eq.(4.5).

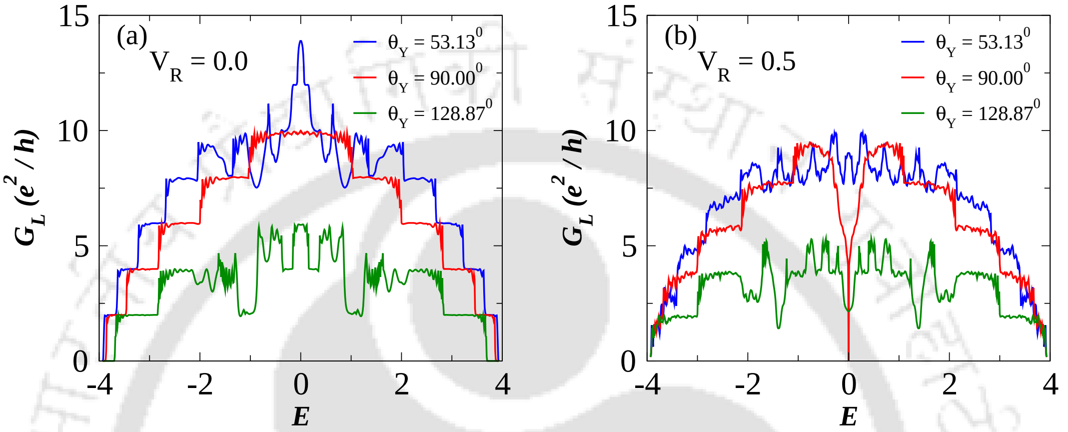

Figure 4.8: (a) G_L is plotted as a function of energy, E for three different angle of the Y-shaped device when RSOC is absent. G_L shows step-like nature. (b) G_L is plotted as a function of E in presence of RSOC with strength $V_R = 0.5$. The step-like nature of G_L is partially lost.

4.4 Conclusion

In summary, in the present chapter, we have studied the effect of the angular separation of a three terminal Y-shaped junction device in presence of Rashba and Dresselhaus spin-orbit couplings on the spin Hall conductance by Landauer-Büttiker formalism. A prescription for the fabrication of the Y-shaped structures with different angular separation is presented. In presence of RSOC, the colour maps of the spin Hall conductance show interesting features as a function of the parameters denoting the spin quantization axes (θ, ϕ) for three different angular separations of the Y-shaped device. Interesting symmetry axes and periodic behaviour of G_{SH} are noted in the same context. A lower angular separation yields a larger G_{SH} owing to enhanced spin Hall current. The results reveal that the rotational symmetry in spin space is lost owing to the SO couplings present therein. A comparison between RSOC and the SO interaction of the other kind, that is, the Dresselhaus SO interaction is made via studying the behaviour of G_{SH}. G_{SH} is antisymmetric in nature with respect to the $V_R = V_D$ line and for $V_R = V_D$, G_{SH} is exactly zero, results that are expected. The colour plots of G_L as a function of V_R and V_D are different for different values of θ_Y, and the value of G_L is larger for smaller θ_Y. The colour plots are symmetric along the $V_R = V_D$ line. The longitudinal conductance is also symmetric as a function of the Fermi energy about $E = 0$.

We believe that with the advent of improved fabrication technologies, our studies of SHE in three terminal Y-shaped junction devices can be experimentally achievable and should be instrumental in designing newer spintronic devices.

Chapter 5

Non-magnetic Adatoms in Graphene Nanoribbons

In chapters 3 and 4, we have discussed the longitudinal and spin Hall conductances for a four terminal and a three terminal (Y-shaped) device respectively. The non-zero spin Hall conductance induced by the (Rashba) spin-orbit coupling emphasizes their utility as possible spintronic devices. Interesting interplay between spin-orbit coupling, disorder and other device parameters (such as the angular separation for a Y-shaped device in chapter 4) are investigated in details. Without a closer look at the graphene-based devices, the above studies will remain incomplete.

Successful fabrication of graphene[39] has attracted a wide attention in both experimental and theoretical investigations. It has several interesting transport properties[40], such as unconventional quantum Hall effect[39,41,42], half-metallicity[43,44] and high carrier mobility[45,158]. These features make graphene a promising candidate for applications in nanoelectronics and spintronic devices. On a parallel front, Kane and Mele[50,51] predicted that quantum spin Hall (QSH) state can be observed in presence of intrinsic spin-orbit coupling (SOC) which can be created by a complex next nearest hopping that differentiates a left hop from a right one. The proposal of such symmetry allowing hopping term has triggered an enormous study on topologically nontrivial electronic materials[52–55]. However, as said earlier, the QSH effect in clean graphene is not observed experimentally owing to its vanishingly small intrinsic spin-orbit coupling (SOC) strength[56,57], whereas in strained semiconductors, such as CdTe/HgTe quantum wells, the QSH effect has been observed[58]. The theoretical proposal by Bernevig, Hughes and Zhang[159] and subsequent experimental demonstration of a QSH phase[91] in this regard have initiated intense scientific research. However, we shall skip this discussion in our thesis and focus mainly of graphene.

It was theoretically proposed that adsorption of heavy adatoms such as Indium (In^{49}), Thallium (Tl^{81}), Gold (Au^{79}) etc. can enhance or induce intrinsic SOC or Rashba SOC in graphene[59–61,160]. While the intrinsic SOC is crucially required for the predicted QSH effect, Rashba SOC is believed to be detrimental to it. Adatoms such as In or Tl can open up a significant topologically nontrivial gap, different theoretical studies have confirmed that the two systems (that is In and Tl decorated graphene) are indeed stable topological insulators[59,61,62]. On the other hand, Au-like adatoms induce Rashba SOC which dominates over the intrinsic SOC and QSH effect will likely to lose in the competition. Therefore it will be relevant to study the transport properties of Au adatom decorated graphene to illustrate the validity of the above scenario. Moreover, owing to the presence of Rashba SOC induced by Au adatoms features of the spin polarized conductance may provide additional clues on the topological phase. It is important to understand the role of the intrinsic spin-orbit coupling in stabilizing the QSH phase in this regard. The QSH phase which is usually identified by the presence of a plateau of finite ($2e^2/h$) value for the longitudinal conductance in a two terminal system may not yield a robust signature for the presence of the QSH phase. The reason for this could be the absence of the conducting edge states that are protected by time reversal symmetry along with an insulating bulk. Other adatoms with larger intrinsic spin-orbit strengths may ensure both the plateau and the conducting edge states.

The electronic, structural, and magnetic properties of transition metals adsorbed on graphene sheets[65,161,162] and graphene nanoribbons (GNR)[163–166] have been studied extensively, which are mostly based on ab-initio density-functional theory (DFT). However, there are very few studies on the spin dependent transport of Au decorated adatoms that discuss the spin Hall effect and features like nonlocal resistance etc[167]. For a recent review, see Ref. [168].

It is helpful to recapitulate that the electronic properties of GNRs depend on the geometry of the edges and the lateral width of the nanoribbons[48], and according to the edge termination type, mainly there are two kinds of GNR, namely armchair graphene nanoribbon (AGNR)and zigzag graphene nanoribbon (ZGNR). The ZGNRs are always metallic with zero bandgaps, while the AGNRs are metallic when the lateral width $N = 3M - 1$ (M is an integer), else the AGNRs are semiconducting in nature[49] with a finite band gap.

Since Rashba SOC is the key factor for the spin polarized transport, in this chapter our aim will be on the exploration of spin dependent transport properties of Au decorated adatoms in GNRs and comment on the presence of the QSH phase

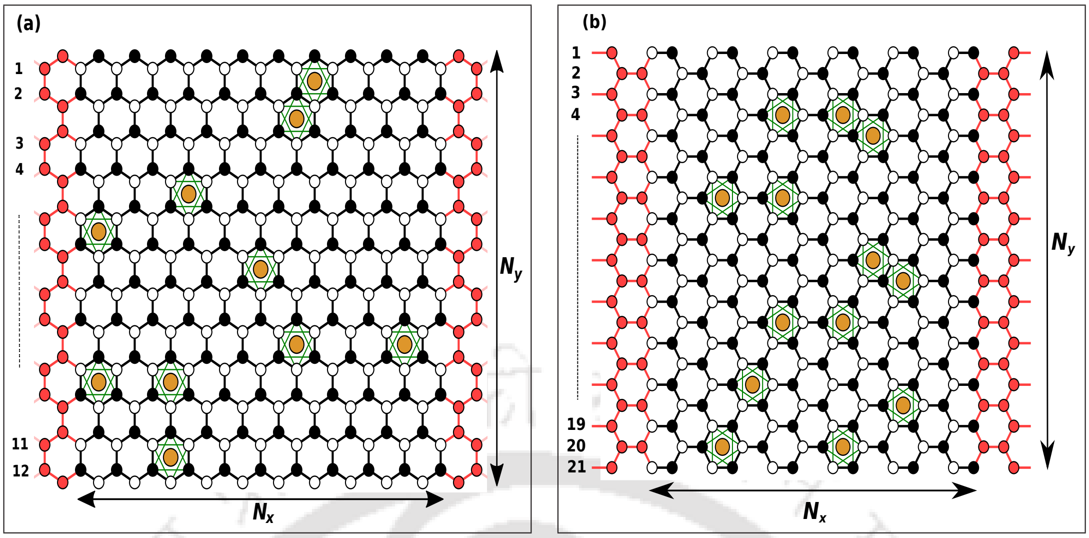

Figure 5.1: Schematic view of a two terminal Au adatom decorated graphene nanoribbon. (a) ZGNR and (b) AGNR. The black and white circles represent the A and B sublattices of graphene. The golden circles are the Au adatoms. The green line is for the next nearest neighbour hopping, which represents the intrinsic SOC, while the black lines surrounding the Au atoms correspond to nearest neighbour hopping and Rashba SOC. Rest of the black lines contain only nearest neighbour hopping.

therein. This is particularly important owing to a vanishingly small intrinsic SOC, a crucial ingredient for the observation of the QSH phase.

We organize this chapter as follows. In the following section, we present for completeness, the theoretical formalism leading to the expressions for the charge and spin polarized conductances using the well-known Landauer-Büttiker formula. After that, we include an elaborate discussion of the results. Here we have tried to resolve few queries, such as whether the QSH state exists in Au decorated adatoms, how the spin polarized conductance behave in the above system and so on. We have also included an interesting comparison for the conductance properties for the case of AGNR vis-a-vis that of ZGNR.

5.1 Theoretical formulation and model

To begin with, we describe the geometry of the system and make our notations clear. We consider a graphene sheet adsorbed with Au atoms, which prefer to reside at the center of the carbon rings[59] where it can interact only with the surrounding six-nearest carbon atoms and can enhance the intrinsic SOC or induce Rashba SOC. The effective tight-binding Hamiltonian for graphene with such adatoms is given by[50,59,62],

$$
\begin{aligned}
H = -t \sum_{\langle ij \rangle} c_i^\dagger c_j + i\lambda_{SO} \sum_{\langle\langle ij \rangle\rangle \in \mathcal{R}} \nu_{ij} c_i^\dagger s^z c_j \\
+ i\lambda_R \sum_{\langle ij \rangle \in \mathcal{R}} c_i^\dagger \left(\mathbf{s} \times \hat{\mathbf{d}}_{ij} \right)_z c_j - \mu \sum_{i \in \mathcal{R}} c_i^\dagger c_i
\end{aligned} \tag{5.1}
$$

where $c_i^\dagger = \begin{pmatrix} c_{i\uparrow}^\dagger & c_{i\downarrow}^\dagger \end{pmatrix}$ is the creation operator of electrons at site i. The first term is the nearest neighbour hopping term, with a hopping strength, $t = 2.7$ eV. The second term is the local intrinsic spin-orbit coupling term enhanced by the adatoms residing on the set of hexagons $\mathcal{R}$ that are inhabited by the Au adatoms. λ_{SO} is the strength of the intrinsic SOC. The third term is the nearest neighbour Rashba term which explicitly violates the inversion symmetry, that is $z \to -z$ symmetry. The last term is the on-site potential, μ of the carbon atoms in the hexagons hosting adatoms, which describe the chemical potential that screens charge from the adatoms.

It may be noted that we have used both α and V_R in earlier chapters to denote the strength of RSOC, however, to keep harmony with the symbols used by various authors for the parameters of the Kane-Mele model, this and in the subsequent chapters, we have used λ_R to denote RSOC.

5.1.1 Two terminal (2T) GNR: formulation of charge and spin polarized conductances

We define the charge and spin polarized conductances as follows,

$$
G = \frac{I^q}{V_L - V_R} \qquad G_\alpha^s = \frac{\hbar}{2e}\left[\frac{I^\alpha}{V_L - V_R}\right] \tag{5.2}
$$

where I^q is the charge current flowing from the left lead to the right lead and I^α $(\alpha = x, y, z)$ is the spin current polarized in a particular direction, α and flowing from left lead to right lead. V_i is the potential at the i-th lead.

Following the Landauer-Büttiker formula[1,133], the charge and spin currents can be calculated from the following expression[168,169],

$$
I_p^\alpha = \frac{e^2}{h} \sum_q \mathrm{Tr}\left[\hat{\sigma}_\alpha \Gamma_\mathrm{q} \mathcal{G}_\mathrm{R} \Gamma_\mathrm{p} \mathcal{G}_\mathrm{A}\right] (\mathrm{V_p} - \mathrm{V_q}) \tag{5.3}
$$

where, $\hat{\sigma}_\alpha = (\sigma_0, \sigma_x, \sigma_y, \sigma_z)$. σ_0 is a 2×2 identity matrix and $\sigma_x, \sigma_y, \sigma_z$ are the Pauli matrices. The σ_0 term in Eq.(5.3) gives the usual charge current, while those with the Pauli matrices yield the spin currents polarized in different directions that is (x, y and z).

Further we define the fluctuations in the spin polarized conductance as,

$$\Delta G_{\alpha}^{s} = \sqrt{\langle (G_{\alpha}^{s})^{2} \rangle - \langle G_{\alpha}^{s} \rangle^{2}} \tag{5.4}$$

where $\langle ... \rangle$ denotes averaging being done over an ensemble of samples with different distributions of adatoms for a particular adatom density n_{ad}.

Fig.5.1 shows the geometry used for the calculations of charge and spin polarized conductances. Fig.5.1(a) is the setup corresponds to a ZGNR while Fig.5.1(b) represents that of an AGNR. The length and the width of these systems can be determined as shown in the given figure (Fig.5.1). The systems, for example in Fig.5.1(a), have a width, $N_y = 12$ and a length, $N_x = 21$. Thus we can denote the zigzag setup by N_xZ-N_yA = 21Z-12A. Likewise we may denote the armchair setup by 12A-21Z (see Fig.5.1(b)).

The black and white circles stand for the A and B sublattices of graphene. The golden circles are the Au adatoms. The green line is for the next nearest neighbour hopping, which represents the intrinsic SOC, while the black lines surrounding the Au adatoms correspond to the nearest neighbour hopping and the Rashba SOC. Rest of the black lines denote only nearest neighbour hopping. The leads are semi-infinite in nature, attached at both ends and are denoted by red color. The leads are considered to describes by a pure tight binding graphene lattice and hence are free of any kind of SOC.

5.1.2 Four terminal (4T) GNR: formulation of longitudinal and spin Hall conductances

In order to observe the spin Hall conductance, a charge current is allowed to flow between terminals 1 and 2, and a spin current is observed to flow along the transverse direction of the rectangular sample, that is, between terminals 3 and 4 as shown in Fig.5.2.

In case of a four terminal device, the longitudinal and spin Hall conductances are defined as follows,

$$G_L = \frac{I_2^q}{V_1 - V_2} \quad G_{SH}^{\alpha} = \frac{\hbar}{2e}\left[\frac{I_3^{\alpha}}{V_1 - V_2}\right] \tag{5.5}$$

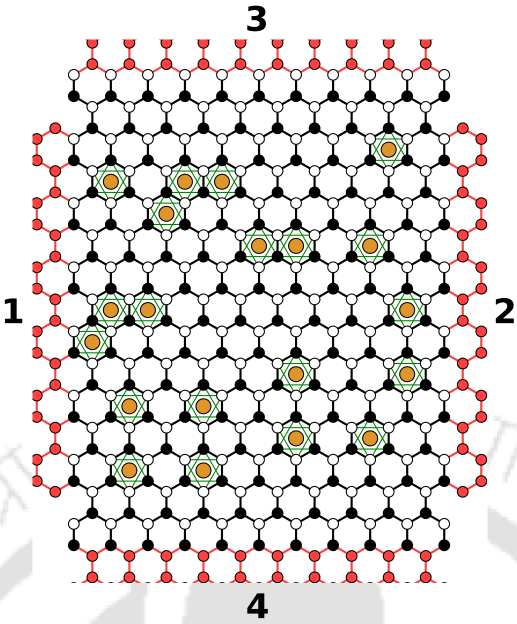

Figure 5.2: Schematic view of a four terminal Au adatom decorated graphene nanoribbon. The black and white circles represent the A and B sublattices of graphene. The golden circles are the Au adatoms. The green line is for the next nearest neighbour hopping, which represents the intrinsic SOC, while the black lines surrounding the Au atoms correspond to nearest neighbour hopping and Rashba SOC. Rest of the black lines contain only nearest neighbour hopping. The leads are attached at the four sides, which are denoted by red color and are semi-infinite in nature. The leads are free of any kind of SOC.

where I_2^q is the charge current flowing through terminal 2 and I_3^α $(\alpha = x, y, z)$ is the spin current polarized in a particular direction, α and flowing through terminal 3. V_i is the potential at the i-th lead.

Since leads 3 and 4 are voltage probes, we can consider, $I_3^q = I_4^q = 0$. On the other hand, as the currents in various leads depend only on voltage differences among them, we can set one of the voltages to zero without any loss of generality. Here we set $V_2 = 0$.

5.2 Results and Discussions

We have investigated the effect of the conducting edges of AGNR and ZGNR in presence of intrinsic and Rashba SOC induced by the adatoms on the experimentally measurable quantity, namely the two terminal charge conductance (G) and spin polarized conductance (G_α^s, $\alpha = x, y, z$).

5.2.1 Two terminal (2T) conductance

Before embarking on the results, we briefly describe the values of different parameters used in our calculation. Throughout our work, we take the ZGNR setup as 89Z-48A and the AGNR setup as 48A-89Z (see Fig.5.1). All the energies are measured in unit of t. The charge conductance is measured in units of e^2/h and the spin polarized conductance is measured in units of $e/4\pi$. Also the lattice constant, a is taken to be unity. All the measurable quantities are averaged over 100 independent random-adatom configurations for different adatom concentrations, n_{ad}. In this work, we have considered three different Au adatom concentrations, namely, $n_{ad} = 0.1, 0.2$ and 0.3. For most of our numerical calculations we have used KWANT[93].

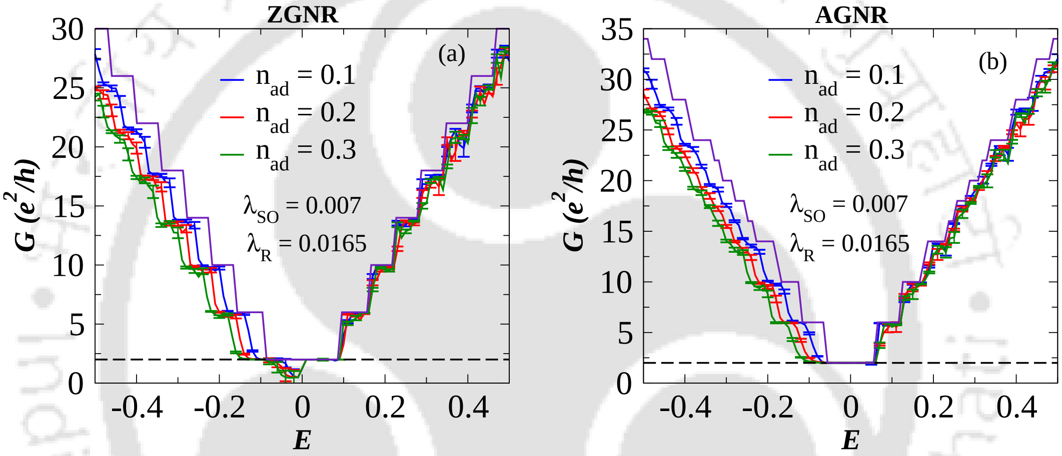

Figure 5.3: G is plotted as a function of Fermi energy in case of Au adatoms, where $\lambda_{SO} = 0.007$, $\lambda_R = 0.0165$ and $\mu = 0.1$ for (a) ZGNR case and (b) AGNR case. The $2e^2/h$ plateau is missing in the ZGNR setup but is present in the AGNR case. Clean limit (violet) are included for comparison. The $2e^2/h$ plateau is present in the clean limit.

The signature for the topological insulator or the QSH phase is that there exists a $2e^2/h$ conductance plateau and the system conducts via the edge states only, while the system in bulk remains insulating in nature. Fig.5.3 shows the variation of the conductance as a function of the Fermi energy, E with Au adatoms for three different adatom densities, namely $n_{ad} = 0.1, 0.2$ and 0.3. From the first-principles calculations[59,167], we use the following parameters: $\lambda_{SO} = 0.007$, $\lambda_R = 0.0165$ and $\mu = 0.1$ (all in units of hopping t). Thus with $t = 2.7$ eV, $\lambda_{SO} = 0.0189$ eV and $\lambda_R = 0.04455$ eV. The dotted black line corresponds to $2e^2/h$ conductance.

For the ZGNR setup as shown in Fig.5.3(a), around the zero of the Fermi energy, there is a dip in the conductance spectrum to a value close to zero. On the other hand, for the AGNR setup (Fig.5.3(b)), a $2e^2/h$ conductance plateau occurs around the zero of the Fermi energy.

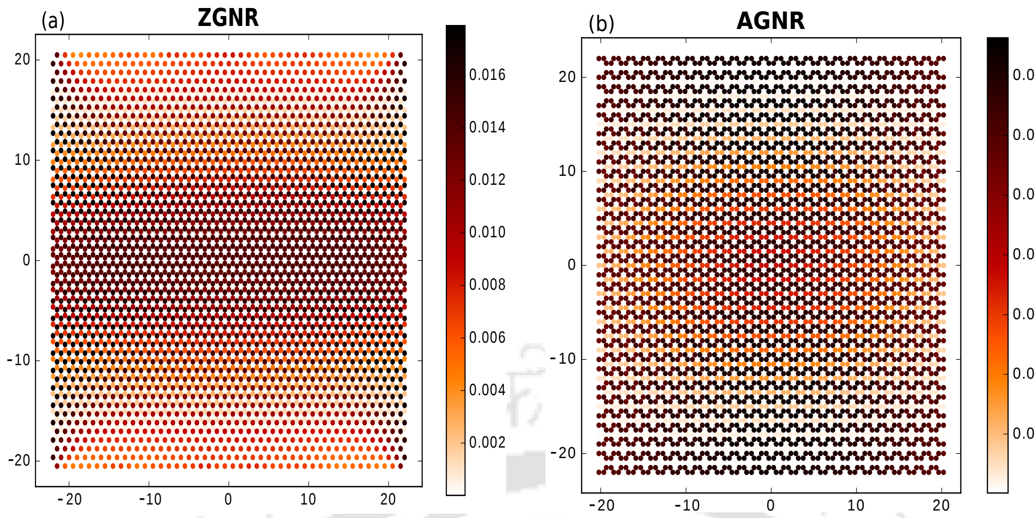

Figure 5.4: LDOS plot for (a) ZGNR and (b) AGNR in case of Au adatoms. Adatom concentration is taken to $n_{ad} = 0.3$. In both the figures, the system is conducting on the whole.

This leads to a straightforward question, that in case of AGNR setup, can the Rashba SOC (which is a dominant contribution here) stabilize the QSH phase. To answer that question, we plot the space-resolved density of states (LDOS) for the ZGNR and AGNR setup as shown in Fig.5.4(a) and Fig.5.4(b) respectively, where the bulk states yield non-vanishing contributions and hence are conducting. As said earlier, it confirms that Rashba SOC is detrimental for observing the QSH effect, which is revealed in our results for the case of Au adatoms.

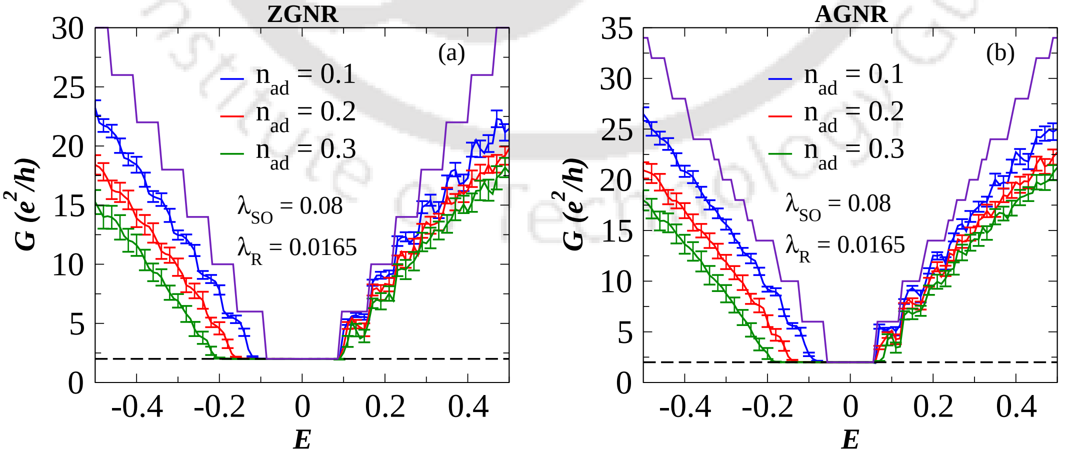

Figure 5.5: Conductance G is plotted as a function of Fermi energy with $\lambda_{SO} = 0.08$ for (a) ZGNR and (b) AGNR. Rest of the parameters are same as in case of Au adatom. A $2e^2/h$ conductance plateau occurs in both the cases. Clean limit (violet) are included for comparison.

Thus the $2e^2/h$ plateau in the conductance behaviour does not guarantee the presence of a non-trivial topological state[170]. This is one of the interesting results of this chapter.

Hence it boils down to the fact that by some means if we are able to enhance the intrinsic SOC by one order of magnitude compared to the value present in the Au decorated graphene, there could be a way to restore the QSH effect. In Fig.5.5, we show the variation of conductance as a function of Fermi energy for the following parameters: $\lambda_{SO} = 0.08$, $\lambda_R = 0.0165$ and $\mu = 0.1$, that is all the other parameters are same as in case of Au adatom, except for the intrinsic SOC. Clearly the $2e^2/h$ conductance plateau re-emerges for the ZGNR setup (Fig5.5(a)) as well as in case of AGNR (Fig5.5(b)).

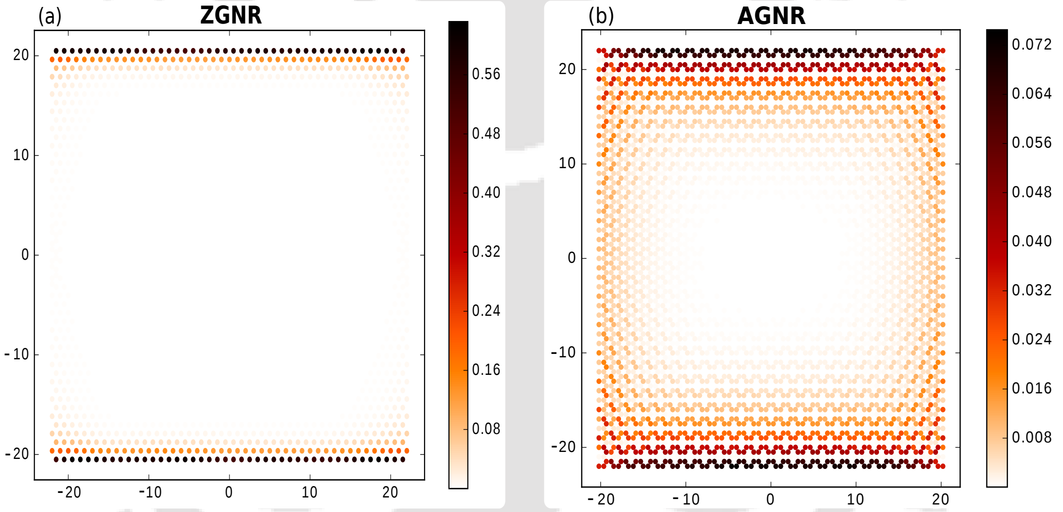

Figure 5.6: LDOS plots for (a) ZGNR and (b) AGNR case with $\lambda_{SO} = 0.08$ and other parameters same as that of Au adatom for adatom density, $n_{ad} = 0.3$. Edge states are again conducting with an insulating nature for the bulk states.

The LDOS plots yielding edge states and an insulating bulk also support our claim as shown in Fig5.6(a) and Fig5.6(b). We also note that there is a certain threshold value required for the intrinsic SOC to recover the QSH effect. The threshold is independent of the system size, at least for the few system dimensions checked by us. Specifically, it is observed that when the strength of the intrinsic SOC has the same order of magnitude as that of the chemical potential, the bulk states become insulating in nature and the edge states start to conduct.

Having discussed the QSH phase, we wish to focus on the spintronic applications. Without applying an external magnetic field, spin polarized conductance can be achieved if a Rashba SOC is present in a system. In pristine graphene, though the

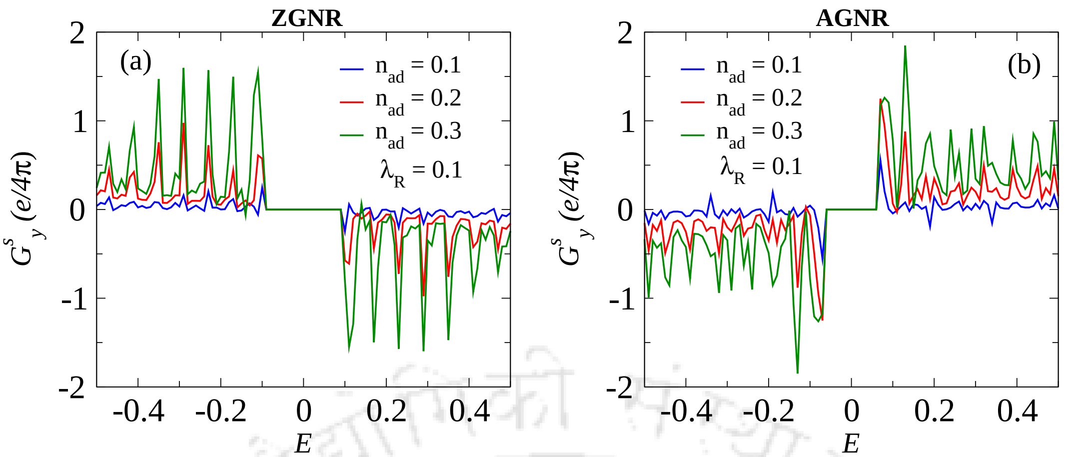

Figure 5.7: The y-component of the spin polarized conductance, G^s_y is plotted as a function of the Fermi energy for $\lambda_R = 0.1$ for (a) ZGNR and (b) AGNR). Magnitude of G^s_y increases with increasing adatom density. The antisymmetry feature about the zero of the Fermi energy for both to be noted. Further, ZGNR and the AGNR have opposite signs for G^s_y with respect to each other.

strength of Rashba SOC is very weak, still it can cause non-vanishing spin polarized conductance. It has been shown that the y-component of spin polarized conductance, G^s_y can be achieved in graphene nanoribbons[171]. Zhang et al.[172,173] shown that the x and z component of the spin polarized conductances (G^s_x, G^s_z) are zero for an ideal graphene nanoribbon because of the longitudinal mirror symmetry of an infinite system[171]. Adsorption of Au adatoms onto GNR breaks this longitudinal mirror symmetry and one can expect a small but non-zero G^s_x and G^s_z. However owing to the finite width of the GNR, the longitudinal mirror symmetry about the y-axis is broken, which is why G^s_y survives. Motivated by this, we study the behaviour of spin polarized conductance in presence of Au adatoms.

We begin our study for the spin polarized conductance by taking a hypothetical adatom which induces Rashba SOC among the neighbouring carbon atoms surrounding by the adatoms. Specifically, we take the strength of the Rashba SOC, $\lambda_R = 0.1$ which is one order of magnitude higher than that of Au adatoms. Fig.5.7 shows the variation of the y-component of the spin polarized conductance $\left(G^s_y\right)$ as a function of the Fermi energy for three different adatom concentrations, namely $n_{ad} = 0.1, 0.2$ and 0.3. Fig.5.7(a) is the result for the ZGNR case and Fig.5.7(b) for the AGNR.

We find a few interesting features in the variation of G^s_y. The spin polarized conductance is anti-symmetric about $E = 0$, which is owing to the electron-hole symmetry[135,171]. Also for $E < 0$, G^s_y is positive (negative) for the ZGNR (AGNR)

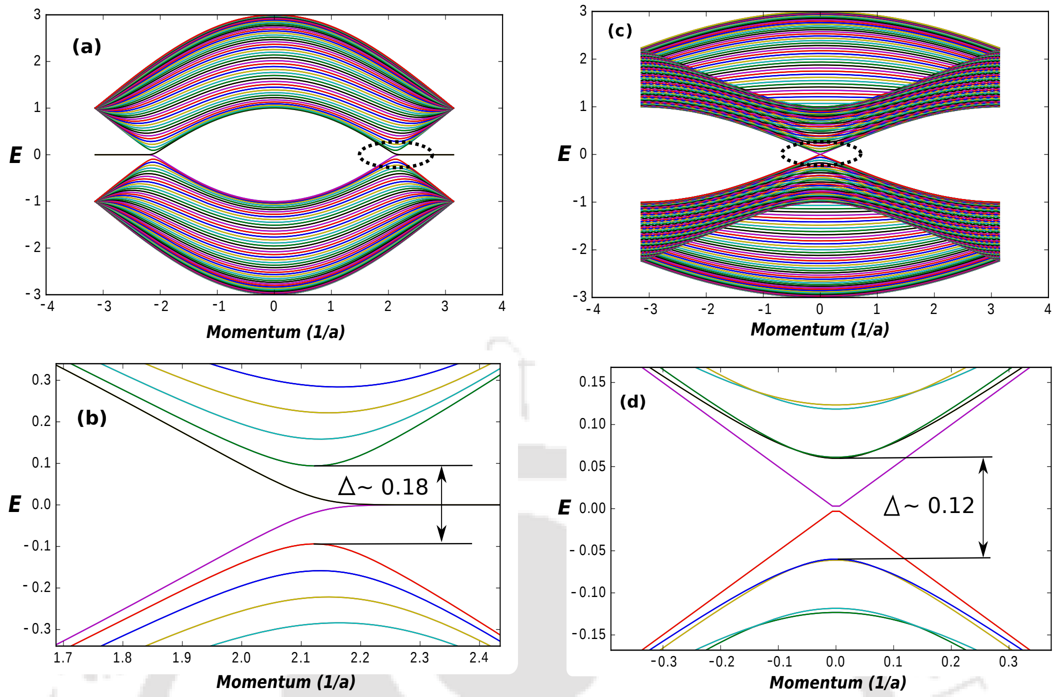

Figure 5.8: (a) Band structure of the ZGNR lead. (b) a closer view of ZGNR band structure denoted by the dotted ellipse. (c) and (d) are the band structure for the AGNR case. (b) and (d) show the single channel transmission. Further, the widths of the energy range over which G_y^s is zero is shown by Δ which is larger in ZGNR ($\Delta \sim 0.18$) compared to AGNR ($\Delta \sim 0.12$).

setup. The AGNR setup is basically the $\pi/2$ rotated version of the ZGNR setup about the z-axis. Under a $\pi/2$ rotation about z-axis, the Hamiltonian for the Rashba SOC changes its sign. Specifically, if we define a Rashba Hamiltonian H_R by, $H_R = \sigma_x p_y - \sigma_y p_x$, then $H_R \xrightarrow{\pi/2 \text{ rotation}} -H_R$. This explains the sign difference between the ZGNR and the AGNR setup. Clearly, the magnitude of the G_y^s increases as we increase the adatom density. The spike-like features originate due to the finite number of modes available for transmission in the leads.

Another important point to be noted here, that there is a finite region about the zero energy, where the spin polarized conductance is strictly zero. For the ZGNR case, the width of the region (in units of t) is $\Delta = 0.18$ and for the AGNR case, it is $\Delta = 0.12$. This can be understood from the band structures of the leads corresponding to the ZGNR and AGNR setup as shown in Fig.5.8. Fig.5.8(a) is the band structure for the ZGNR lead and Fig.5.8(b) is a closer view of the region denoted by the dotted ellipse in Fig.5.8(a). Plots in the right panel are for the AGNR lead. There are only two bands in the energy spectrum within the interval, Δ. In other words, this interval corresponds to single channel transmission. Spin polarization is not possible if there is a single channel transmission[171,174]. Also, this single channel transmission corresponds to the $2e^2/h$ plateau as shown in Fig.5.5.

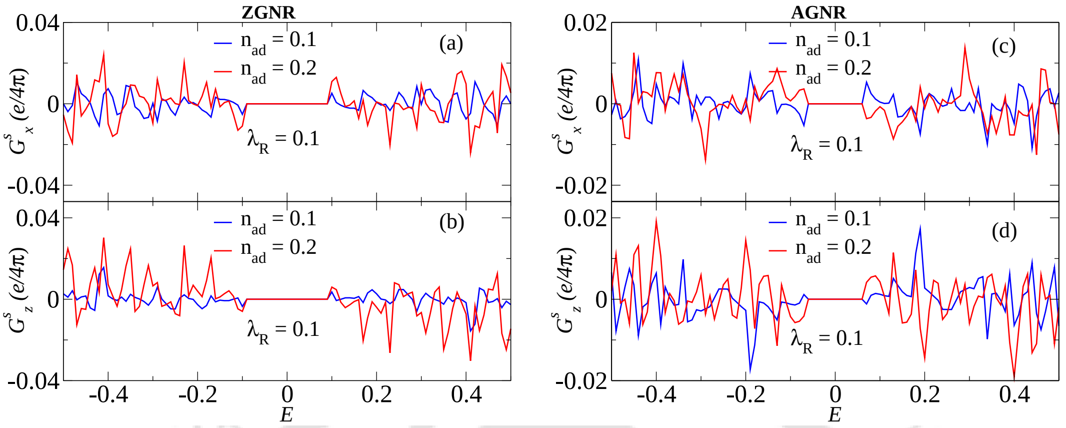

Figure 5.9: x and z-component of the spin polarization are plotted as a function of the Fermi energy for (a) and (b) ZGNR case and (c) and (d) AGNR case with $\lambda_R = 0.1$. Only two different adatom density, namely $n_{ad} = 0.1, 0.2$ are shown for clarity of presentation. The antisymmetric nature about $E = 0$ can be noted.

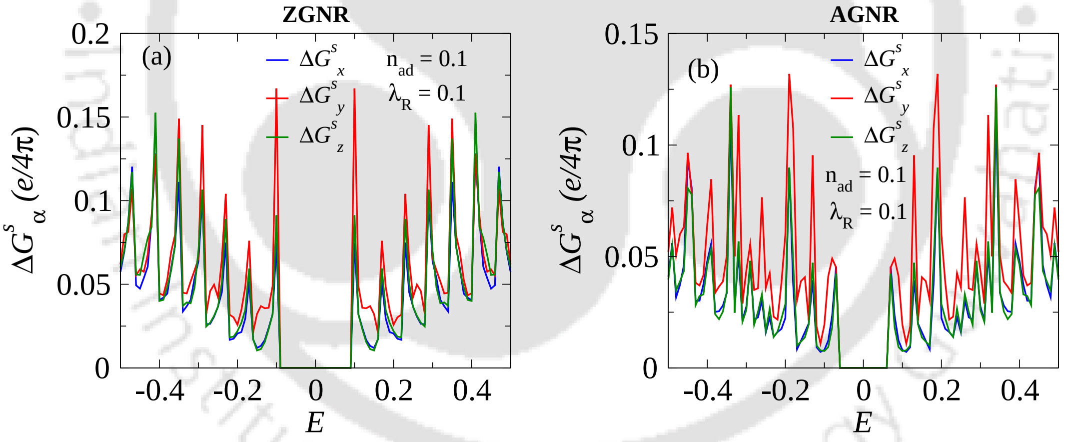

Figure 5.10: The fluctuations in the spin polarized conductance, G^s_α ($\alpha = x, y, z$) is plotted as a function of the Fermi energy for $n_{ad} = 0.1$ and $\lambda_R = 0.1$ in case of (a) ZGNR and (b) AGNR.

As we introduce the random distribution of adatoms in the graphene nanoribbon, we effectively break the longitudinal mirror symmetry in the system. So it is expected that we should have a non-zero G^s_x and G^s_z. Fig.5.9 shows the variation of G^s_x and G^s_z as a function of the Fermi energy for two different adatom densities, namely $n_{ad} = 0.1$ and 0.2. Fig.5.9(a) stands for the ZGNR setup while Fig.5.9(b) denotes the AGNR. Certainly, by destroying the longitudinal mirror symmetry we are able to generate a non-zero G^s_x and G^s_z. However, the order of magnitude for the

x and z-components are two orders of magnitude smaller than the y-component of the spin polarized conductance.

A notable feature of Fig.5.9 is the fluctuations present in the spin polarized conductance. These fluctuations are due to the finite size effects originating from the finite number of conducting modes present in the leads. As coherent transport involves mesoscale and nanoscale devices, the finite size effects are indispensable and hence fluctuations persist.

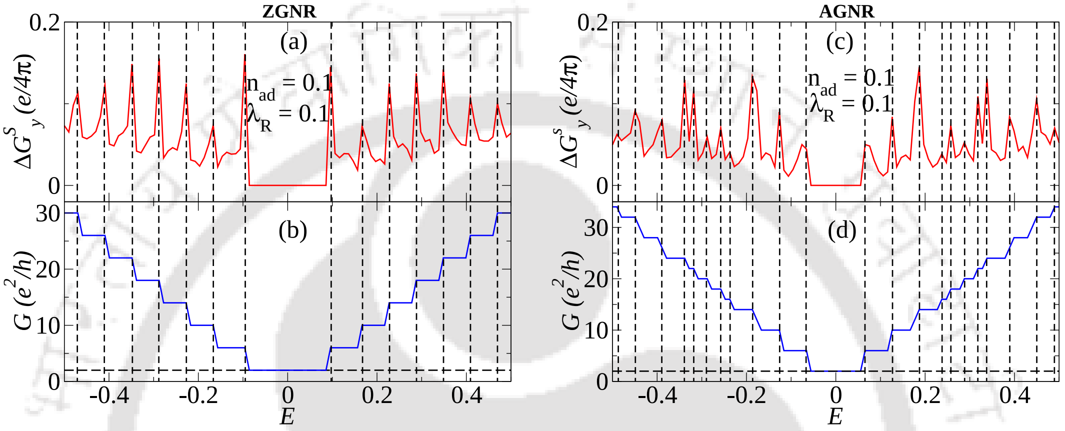

Figure 5.11: ΔG^s_y is plotted as a function of the Fermi energy for (a) ZGNR case and (c) AGNR case with $\lambda_R = 0.1$ and adatom density, $n_{ad} = 0.1$. Charge conductance, G is plotted as a function of E in the clean limit for (b) ZGNR case and for (d) AGNR case. Vertical dotted lines are shown for comparison. The peaks in ΔG^s_y are accompanied by the steps seen in G.

Since we are considering an average over a finite number of random configurations (we use 100 configurations here) in order to calculate the spin polarized conductance, it is relevant to study the fluctuations in G^s_α ($\alpha = x, y, z$). Fig.5.10 shows the fluctuations in the spin polarized conductance, ΔG^s_α as a function of the Fermi energy. Though we did not find any similarity in the behaviour among the three components of the spin polarization, however, the nature of fluctuations of these three components are exactly the same. The spikes in these fluctuation spectra can be understood if we take a look at Fig.5.11, where the variation of ΔG^s_y is shown for the ZGNR case in Fig.5.11(a) and for the AGNR case in Fig.5.11(c). In the lower panel, we plot the variation of the charge conductance, G for the ZGNR case in Fig.5.11(b) and for the AGNR case in Fig.5.11(d) in the clean limit, that is, where the system is free from any kind of spin-orbit interaction. In this limit, G shows a step-like behaviour as expected. The frequency of the steps occurring in the conductance spectra depends on the number of modes available to the system for conduction for a given energy range. For each step-like feature in G, there is a peak in ΔG^s_y. Thus we can say that, whenever a mode opens at a particular energy, the fluctuation in ΔG^s_y shoots up and thus there is a spike.

Apart from a trivial sign of the values of the spin polarization, the qualitative behaviour corresponding to the ZGNR and AGNR setups are almost same. Hence, from now on, for brevity, we shall focus on the ZGNR setup only.

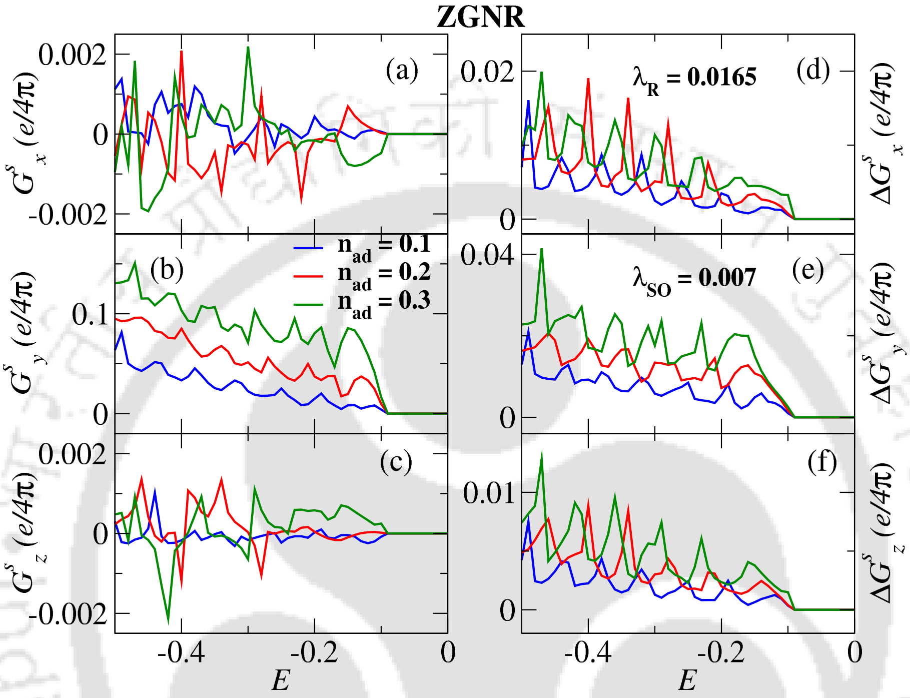

Figure 5.12: (a-c) All the three components of spin polarized conductance and (d-f) their corresponding fluctuations are plotted as a function of Fermi energy for the ZGNR case only in case of Au adatom. G^s_y is the dominant component. The fluctuations in $G^s_{x,y}$ are one order larger than the corresponding values themselves.

The variation of the spin polarized conductance and their fluctuations as a function of the Fermi energy are shown in Fig.5.12 for the case of Au adatoms. The x, y and z-component of the spin polarization are plotted in Fig.5.12(a)-(c) and their corresponding fluctuations in Fig.5.12(d)-(f). Here, owing to large fluctuations compared to the charge conductance case, 200 random-adatom configurations are taken. The magnitudes of G^s_x and G^s_z are smaller by two orders of magnitude than G^s_y. Also, x and z components of the spin polarizations do not have any regular feature as a function of the Fermi energy. However, the fact that they have non-zero values speaks on the prospects of them being used as spintronic devices. It may be noted that the chemical potential for the Au adatoms is taken as $\mu = 0.1$ (in units of t), so when the Fermi energy becomes equal or greater than the μ value, the screening of charges between the Au adatoms and its neighbouring carbon atoms may no longer valid. The absence of such screening renders a large fluctuation in the spin Hall conductance. Hence to have a better clarity we have shown the data corresponding to $E \leq 0$. We find that G^s_y and ΔG^s_y increase as we increase the adatom density.

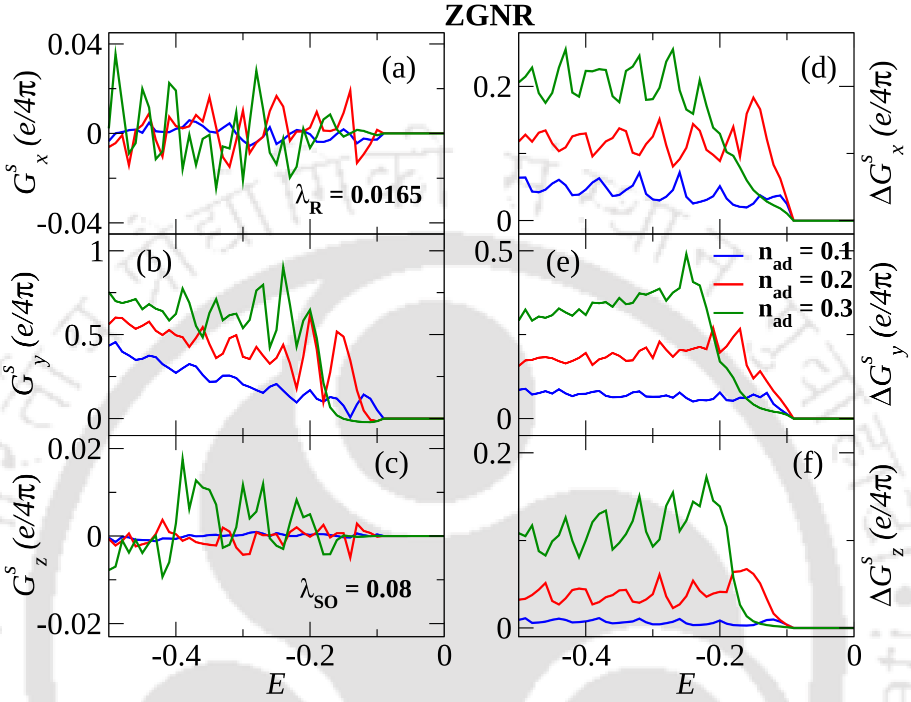

Figure 5.13: (a-c) All the three components of spin polarized conductance and (d-f) their corresponding fluctuations are plotted as a function of Fermi energy for ZGNR case only with $\lambda_{SO} = 0.08$ (hypothetical adatom). Rest of the parameters are same as Au adatom.

By increasing the strength of intrinsic SOC, the results discussed above can be improved a little. In this case we set $\lambda_{SO} = 0.08$. Rest of the parameters are taken exactly same as that of Au adatom. Fig.5.13 shows the variation of G^s_x, G^s_y and G^s_z and their corresponding fluctuations as a function of Fermi energy for $n_{ad} = 0.1, 0.2$ and 0.3. The magnitudes of all the three components of spin polarization increase than the situation that corresponds to Au adatoms (Fig.5.12), along with reduced oscillatory nature for $E \geq 0.1$. Fig.5.13(d-f) show the behaviour of ΔG^s_x, ΔG^s_y and ΔG^s_z. Here they show very similar behaviour as a function of the Fermi energy. One can ask why the fluctuations have a greater magnitude than their observables. Since the spin polarized conductance can have both positive as well as negative values and also since their magnitudes are close to zero, there is a finite possibility that the averaged values can be close to zero. On the other hand, if we recall the expression for the fluctuations (see Eq.(5.4)), the term $\langle (G^s_\alpha)^2 \rangle$ is always is greater than zero and additive in nature. As a result, ΔG^s_α assumes large (and oscillatory) values.

For additional support, we have also plotted the local charge current for the ZGNR system with Au adatoms and also for the adatoms with enhanced intrinsic spin-orbit interaction as shown in Fig.5.14. The local current distribution plot for Au adatom is shown in Fig.5.14(a). Clearly, the current is flowing through the bulk and hence the system does not have any QSH phase. However, for the enhanced intrinsic SOC case (Fig.5.14(b)), the local current flows only along the two sides of the system, revealing that the system again recovers the QSH phase.

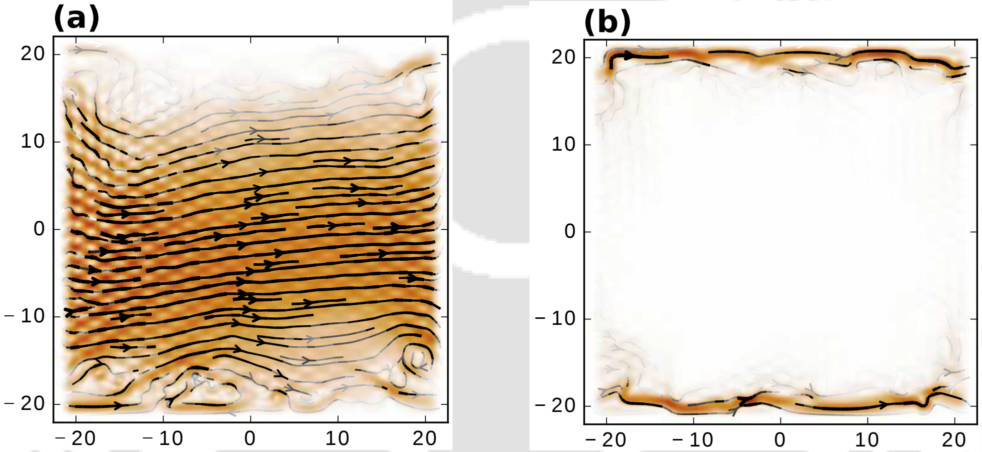

Figure 5.14: (a) Local charge current distribution plot in case of Au adatom. (b) Local charge current plot for adatoms with enhanced intrinsic SOC. Plot in (b) shows clearly existence of edge modes and non-conducting bulk states.

5.2.2 Four terminal (4T) conductance

We have also studied a four terminal (4T) Au decorated graphene nanoribbon setup in order to specifically observe the spin Hall conductance. To begin with the results the case of a 4T device, we shall remind ourselves Fig.5.2, where an electric current is allowed to pass between terminals 1 and 2 and the corresponding longitudinal conductance is measured. Terminals 3 and 4 are the voltage probes and hence there will be no charge current flowing through them. The spin Hall conductance is measured between terminals 3 and 4. The longitudinal conductance is measured in units of e^2/h and the spin Hall conductance is measured in units of $e/4\pi$.

In this section, in addition to Au adatoms, we have also considered Tl adatoms. The inclusion of Tl in the present context is to emphasize on the spin Hall conductance spectrum which is essential for spintronic applications. This point elaborated in the following discussion.

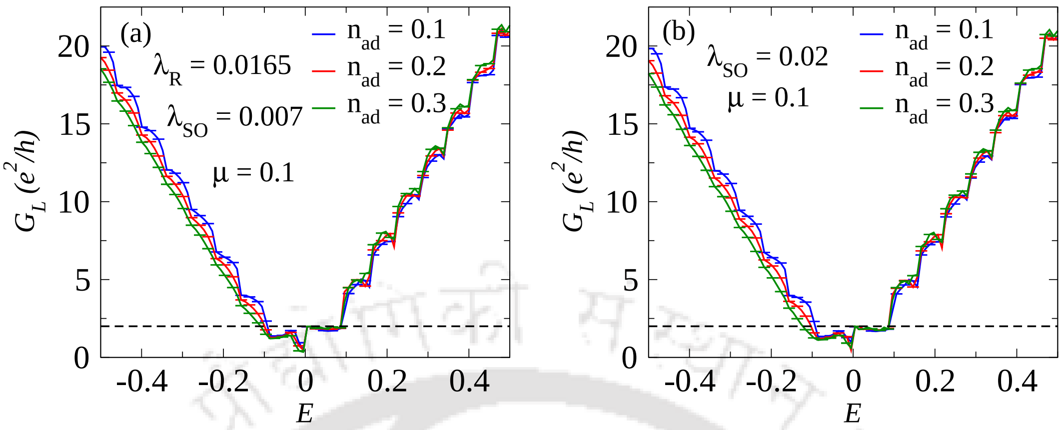

Figure 5.15: The longitudinal conductance, G_L is plotted as a function of the Fermi energy, E for three different adatom concentrations for (a) Au adatom and (b) Tl adatom. The $2e^2/h$ plateau is destroyed signalling onset of ordinary insulating phase.

The behaviour of the longitudinal conductance, G_L for the 4T case is plotted as a function of the Fermi energy, E for Au and Tl as shown in Fig.5.15(a) and Fig.5.15(b) respectively. The behaviour of G_L is more or less same both for types of adatoms, showing that the longitudinal conductance is independent of the intrinsic or Rashba spin-orbit interactions, which it should be. Around the zero of the Fermi energy, there is no flat plateau with a $2e^2/h$ value and hence there is no QSH phase.

The variation of spin Hall conductance (in units of $e/4\pi$) as a function of the Fermi energy is plotted in Fig.5.16(a). The energy range (in units of t) is taken for [-0.5:0], for the same reason as we discussed in Fig.5.12. Al the three components of the spin Hall conductance have the same order of magnitude and they increase with increasing the adatom concentration. The corresponding fluctuations are also plotted in Fig.5.16(b). The fluctuations increase with increasing adatom concentration.

Tl adatoms only enhance the intrinsic SOC and as a result, they can only generate the z-component of the spin Hall conductance, G^z_{SH}. The variation of G^z_{SH} and the corresponding fluctuations ΔG^z_{SH}, are plotted as a function of the Fermi energy as shown in Fig.5.17(a) and Fig.5.17(b) respectively. The magnitude of G^z_{SH} is greater than the case for Au adatoms, which is because of the disparity in the strength of the intrinsic SOC. For Au adatoms, $\lambda_{SO} = 0.007$, whereas for Tl adatoms the intrinsic SOC ($\lambda_{SO} = 0.02$) is greater by one order of magnitude. The fluctuations ΔG^z_{SH} also increases as usual with increasing the adatom concentration and has the same order of magnitude as for the case of Au adatoms.

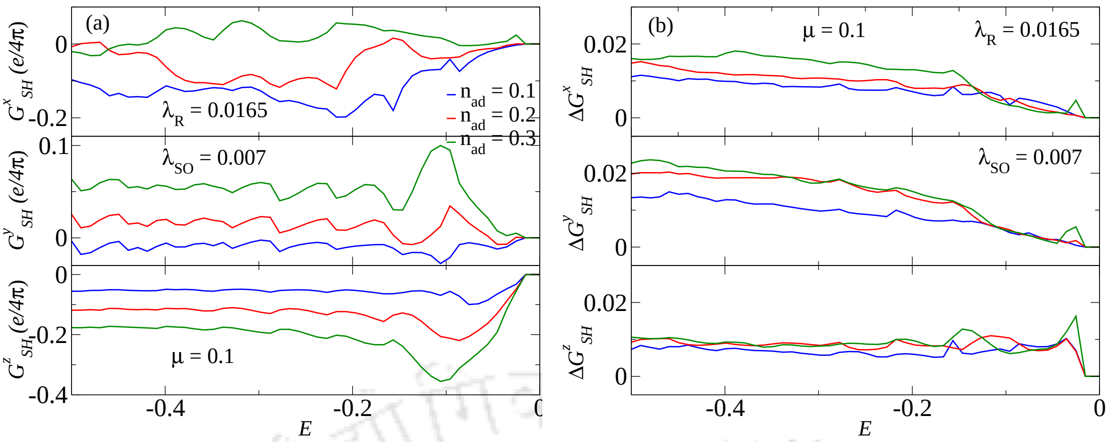

Figure 5.16: (a) Three different components of the spin Hall conductance G^x_{SH}, G^y_{SH} and G^z_{SH} are plotted for Au adatoms as a function of the Fermi energy. (b) Corresponding fluctuations are plotted as a function of the Fermi energy. All the three components are of the same order. There is no longitudinal mirror symmetry present in the system.

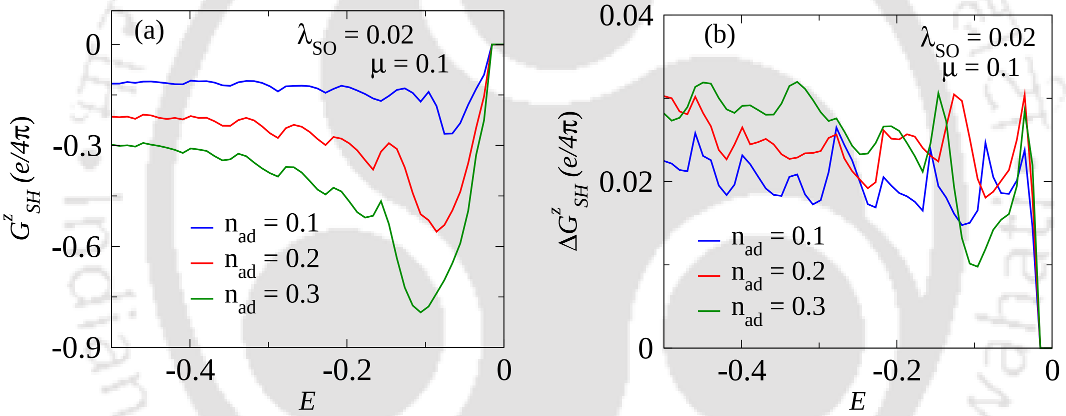

Figure 5.17: G^z_{SH} is plotted for Tl adatoms as a function of the Fermi energy. (b) The corresponding fluctuation is plotted as a function of the Fermi energy. Large adatom density yields higher values of G^z_{SH}.

The flow of the local charge and spin currents are shown in Fig.5.18 for Au adatoms. As shown in Fig.5.18(a), the local charge current is flowing from left end of the system to the right without having any disturbance and is also flowing through the bulk. As we have noticed from the longitudinal conductance behaviour, in the local charge current case there is are edge states carrying current with the presence of insulating bulk states.

Fig.5.18(b),(c) and (d) are for the local spin currents J_x, J_y and J_z respectively. Few of the paths are seen to be even circling around certain points, thereby signaling a vortex-like behaviour. On an average, it is clearly noticeable that the spin currents are flowing in the transverse directions.

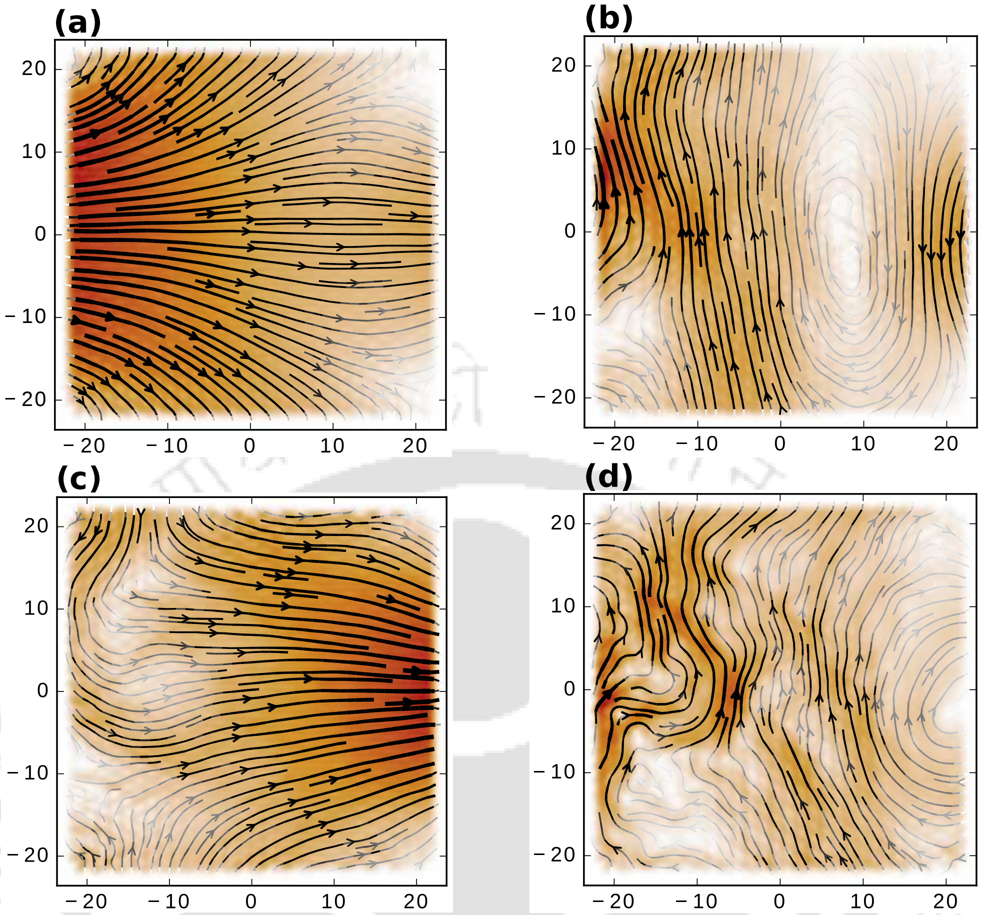

Figure 5.18: (a) The local charge current J_0, (b) the x-component of the local spin current, J_x, (c) the y-component of the local spin current, J_y and (d) the z-component of the local spin current, J_z are shown for the Au adatom case. We set the Fermi energy at $E = -0.1$ (in units of t) and the adatom concentration in the present case is $n_{ad} = 0.1$.

The local charge current and the z-component of the local spin current for Tl adatoms are shown in Fig.5.19(a) and (b) respectively. Here the Fermi energy is fixed at the same value as that of Au adatom, that is at $E = -0.1$ (in units of t) and with adatom concentration, $n_{ad} = 0.1$. The nature of the local charge current is almost same as that of Au adatoms, showing that the charge current is independent of any kind of SOC that is present in the system. For the z-component of the local spin current, few of the paths are also circling around certain points as we have observed in case of Au adatom.

One point should be mentioned here that all the plots in Fig.5.14, Fig.5.18 and Fig.5.19 are obtained for a single configuration corresponding to $n_{ad} = 0.1$. Another configuration or taking an average over several configurations may change the plots, but the qualitative features will remain unaltered.

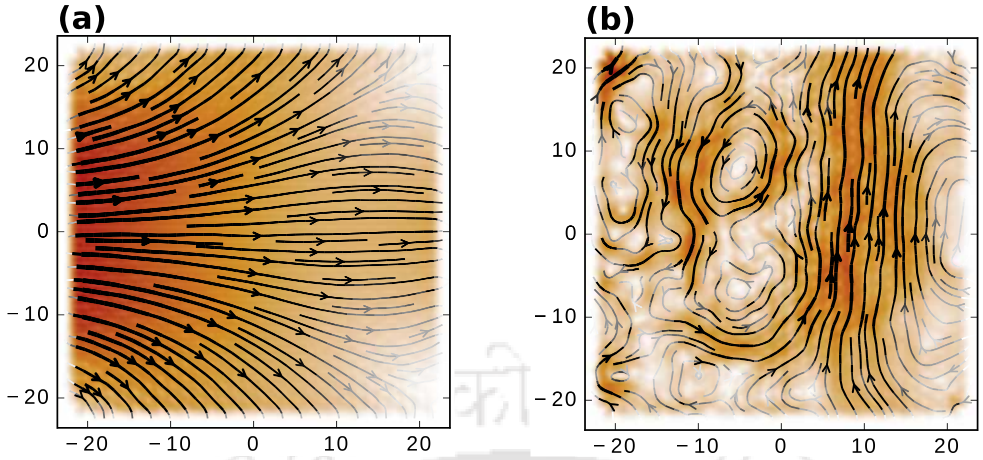

Figure 5.19: (a) The local charge current J_0 and (b) the z-component of the local spin current, J_z are shown for the Tl adatom GNR. We set the Fermi energy at $E = -0.1$ (in units of t) and the adatom concentration in the present case is $n_{ad} = 0.1$.

5.3 Conclusion

In the present chapter, we have studied the behaviour of the charge and spin polarized conductances in two terminal zigzag and armchair graphene nanoribbons with Au adsorbates. Au as an adatom is chosen since it induces Rashba SOC in the ribbon. We made a comparison between the conductance properties of ZGNR and AGNR, where both types of ribbons are found to shown similar qualitative behaviour. In case of Au adatom, the systems are no longer in the QSH phase. However, if we enhance the strength of the intrinsic SOC which may happen for some type of adatoms, the QSH effect can be restored. Nevertheless, the non-zero values of the spin polarized conductance ensure their possible applications in spintronics. A four terminal setup is also studied with Au and Tl adatoms. The spin Hall conductance is greater for the Tl adatoms than that for Au adatoms. However, the Tl adatoms can generate only the $z-$ component of the spin Hall conductance (owing to the absence of RSOC), while Au adatoms are able to generate all its three components.

It may be noted that we have considered an artificial adatom which can induce an intrinsic SOC at least one order larger than that is possible for Au adatoms. Thus careful scrutiny of different (heavy) elements of the periodic table that can induce larger SOC in graphene nanoribbons is needed.

Chapter 6

Magnetic Adatoms in Graphene Nanoribbons

The recent fabrication of freestanding graphene nanoribbons (GNRs)[46,47] has generated renewed interest in carbon-based materials with exotic properties. Since the edges play an important role in determining the electronic properties of GNRs, they offer a variety of possibilities for tunable electronic properties, such as edge modulation by inorganic atoms, molecules or radicals[175–178], application of transverse electric fields[179], adsorption or doping of atoms or molecules[65,161–166,180,181] etc. Metal atoms adsorbed onto graphene sheets also represent a new way for the development of new electronic or spintronic devices. The electronic, structural, and magnetic properties of transition metals (TM) on graphene sheets[65,161,162] and graphene nanoribbons (GNR)[163–166] have been studied extensively, which are mostly based on ab-initio density-functional theory (DFT). The spin dependent transport in GNRs in presence of Rashba SOC has been investigated in some cases, such as spin filtering effect in zigzag GNR[174], possible spin polarization directions for GNR with Rashba SOC[171], effects of spatial symmetry of GNR on spin polarized transport[172] etc. Since we have extensively studied the properties of adatom decorated GNRs in the last chapter, a comparison of the corresponding scenario for the magnetic adatoms is particularly a relevant exercise and forms the focus of this chapter.

Among the metal adatoms, the study of GNRs in presence of transition metals warrants some special attention since TMs serve as important catalysts for the synthesis of graphite, CNT, GNR etc. Since TM catalysts (particularly iron (Fe)) is a common impurity in the graphite[63], graphene layers fabricated from graphite are likely to have these impurities. Longo et al.[64] have shown that the behaviour of Fe atom in a GNR is magnetic, in contrast to the behavior found in graphene[65,66].

Mao et al.[67] showed that adsorption of Fe on graphene makes graphene metallic and generates complete spin polarization. Basically the study of TM adsorption on graphene[68,69] shows possible applications in the realization of graphene-based electronic and spintronic devices. Motivated by the above studies, it will be highly desirable to explore the spintronic behaviour of TM adsorption on graphene and graphene-based structures.

In the present chapter, we explore the charge and spin transport properties of ZGNR decorated by magnetic adatoms. For this, we consider a case where TM (particularly Fe) are adsorbed onto ZGNR. The resulting broken structural symmetry gives rise to a Rashba spin-orbit interaction (RSOC) and the hybridization between the carbon π states and the $3d$-shell states of magnetic adatoms generates a macroscopic exchange field[61]. The first principle calculations report a bulk gap of almost 5.5 meV in Fe adsorbed GNRs, which should be possible to verify in experiments[61]. Further, in order to avoid any complicacy, such as adatom-adatom interaction, spin dependent interactions etc., we consider a very small concentration of magnetic adatoms, so that any interaction other than the RSOC and the exchange field will not be present in our analysis.

We organize this chapter as follows. In the following section, we present, for completeness, the theoretical formalism leading to the expressions for the two terminal charge and spin polarized conductances and four terminal longitudinal and spin Hall conductances using the well-known Landauer-Büttiker formula. Hence we include an elaborate discussion of the numerical results on the conductance. Here, we have attended to resolve few queries, how the spin polarized conductance behaves in the two terminal case, whether there is any similarity between the two terminal spin polarized conductance and four terminal spin Hall conductance. We have also included an interesting comparison for the charge conductance properties for the case of a two and a four terminal ZGNR.

6.1 Theoretical formulation and model

To begin with, we describe the geometry of the system and make our notations clear. We consider a graphene sheet adsorbed with magnetic atoms, which induces Rashba SOC and generates an exchange field. The effective tight-binding Hamiltonian for graphene with such adatoms is given by[61],

$$H = -t\sum_{\langle ij\rangle} c_i^\dagger c_j + i\lambda_R \sum_{\langle ij\rangle\in\mathcal{R}} c_i^\dagger \left(\vec{\sigma}\times\hat{\mathbf{d}}_{ij}\right)_z c_j + \lambda_{EB}\sum_{i\in\mathcal{R}} c_i^\dagger \sigma_z c_i \tag{6.1}$$

where $c_i^\dagger = \begin{pmatrix} c_{i\uparrow}^\dagger & c_{i\downarrow}^\dagger \end{pmatrix}$ is the creation operator of electrons at site i. The first term is the nearest neighbour hopping term, with a hopping strength, $t = 2.7$ eV. The second term is the nearest neighbour Rashba term which explicitly violates $z \to -z$ symmetry. This term is induced by the adatoms residing on the set of hexagons $\mathcal{R}$ that are inhabited by the magnetic adatoms. The third term is the exchange bias that (as shown in Fig.6.1or in Fig.6.2) originates due to the inclusion of magnetic adatoms.

6.1.1 Two terminal (2T) GNR: formulation of charge and spin polarized conductances

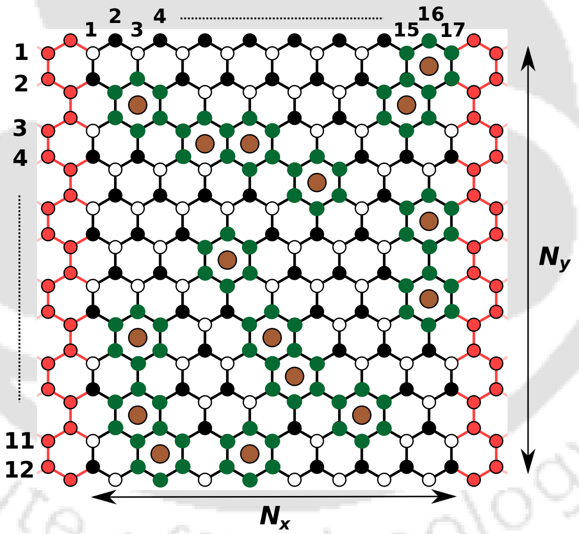

Figure 6.1: Schematic view of a two terminal graphene nanoribbon. The black and white circles represent the A and B sublattices of graphene. The brown circles are the magnetic adatoms. The green circles are the affected site due to magnetic adatoms. The black lines surrounding the magnetic atoms correspond to nearest neighbour hopping and Rashba SOC. Rest of the black lines contain only nearest neighbour hopping. The leads are attached at both ends, which are denoted by red color and are semi-infinite in nature. The leads are free of any kind of SOC. N_x and N_y are the length and width of the nanoribbon respectively. There is no intrinsic spin-orbit coupling.

Fig.6.1 shows the geometry used for the calculations of charge and spin polarized conductances for a 2T device. The theoretical formulation leading to the expressions for conductance is same as shown in Chapter 5. Fig.6.1 is the setup that corresponds to ZGNR. The length and the width of these systems can be determined as shown in the given figure. In Fig.6.1, the width is given by, $N_y = 12$ and the length is, $N_x = 21$. Thus we can denote the zigzag setup by N_xZ-N_yA = 17Z-12A. This nomenclature for denoting the dimensions of the nanoribbon will be followed throughout the chapter.

The black and white circles stand for the A and B sublattices of graphene. The brown circles are the magnetic adatoms. The green circles are the affected sites due to magnetic adatoms. The black lines surrounding the adatoms correspond to the nearest neighbour hopping and the Rashba SOC. Rest of the black lines denote only nearest neighbour hopping. The leads are semi-infinite in nature, attached at both ends and are denoted by red color. The leads are considered to describes by a pure tight binding graphene lattice and hence are free of any kind of SOC.

6.1.2 Four terminal (4T) GNR: formulation of longitudinal and spin Hall conductances

In order to observe the spin Hall conductance, a charge current is allowed to flow between terminals 1 and 2, and a spin current is observed along the transverse direction of the rectangular sample, that is between terminals 3 and 4 as shown in Fig.6.2. The theoretical formulation for the four terminal longitudinal and spin Hall conductances are already outlined in Chapter 5.

6.2 Results and Discussion

We have studied the charge and spin conductance properties in ZGNR decorated by magnetic adatoms and compared the results for two and four terminal devices.

Before embarking on the results, we briefly describe the values of different parameters used in our calculation. We set the hopping term, $t = 2.7$ eV. Throughout our work, we take the ZGNR setup as 89Z-48A for the two terminal case, whereas for the four terminal device it is 85Z-52A. All the energies are measured in the unit of t. The charge conductance is measured in units of $\frac{e^2}{\hbar}$ and the spin polarized conductance is measured in units of $\frac{e}{4\pi}$. Also the lattice constant, a is taken to be unity. All the measurable quantities are averaged over 50 independent random-adatom configurations for different adatom concentrations, n_{ad}. In this work, we have considered three different adatom concentrations, namely, $n_{ad} = 0.025, 0.05$ and 0.1. Further,

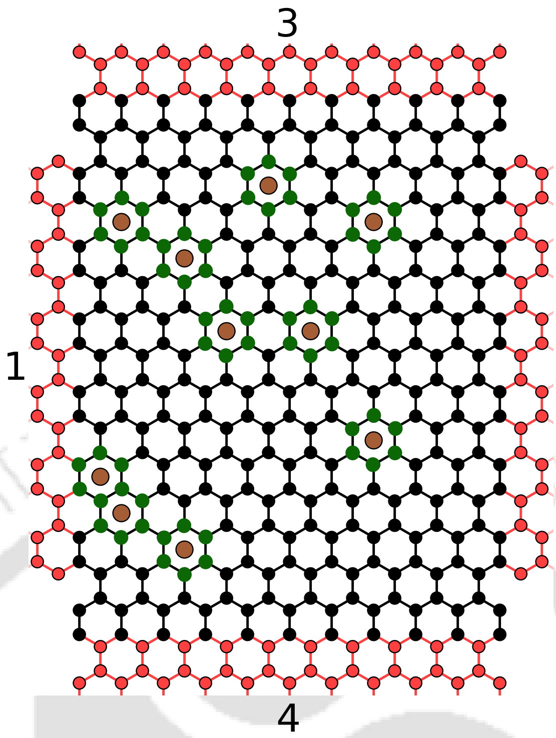

Figure 6.2: Schematic view of a four terminal graphene nanoribbon. The black and white circles represent the A and B sublattices of graphene. The brown circles are the magnetic adatoms. The green circles are the affected sites due to magnetic adatoms. The black lines surrounding the Au atoms correspond to nearest neighbour hopping and Rashba SOC. Rest of the black lines contain only nearest neighbour hopping. The leads are attached at the four sides, which are denoted by red color and are semi-infinite in nature. The leads are free of any kind of SOC.

we have checked that 50 configurations are adequate in the present context, especially, since the adatom densities considered here are small.

6.2.1 Two terminal

The behaviour of charge conductance, G for two terminal case is studied as a function of the Fermi energy, E as shown in Fig.6.3 for two different cases, $\lambda_R = 0$ in Fig.6.3(a) and $\lambda_R = 0.2$ in Fig.6.3(b). The strength of the exchange field is kept fixed at $\lambda_{EB} = 0.18$. Corresponding to these parameters, the insulating bulk states are clearly discernible from the chiral conducting edge states[61]. Thus with $t = 2.7$ eV, $\lambda_R = 0.54$ eV and $\lambda_{EB} = 0.486$ eV.The variation of G as a function of the Fermi energy is quite similar for two different strengths of the Rashba SOC. G is symmetric around the zero of the Fermi energy and shows a necklace-type pattern for both the case. However, the behaviour of G close to zero of the Fermi energy is different for the two different values of λ_R. In order to visualize the behaviour of G close to zero of the Fermi energy, we plot G for a small range of the Fermi energy as shown in the inset in Fig.6.3. In the absence of Rashba SOC, G always stays finite. On the other hand, in presence of Rashba SOC, G tends to vanish values in the vicinity of $E = 0$ as we increase the adatom concentration and it identically vanishing at $n_{ad} = 0.1$. The $2e^2/h$ plateau in pristine graphene is believed to be a signature of the quantum spin Hall insulating phase protected by the time reversal symmetry. In presence of the exchange bias, the time reversal symmetry is explicitly violated leading to the disappearance of the plateau and giving rise to features of an ordinary insulator.

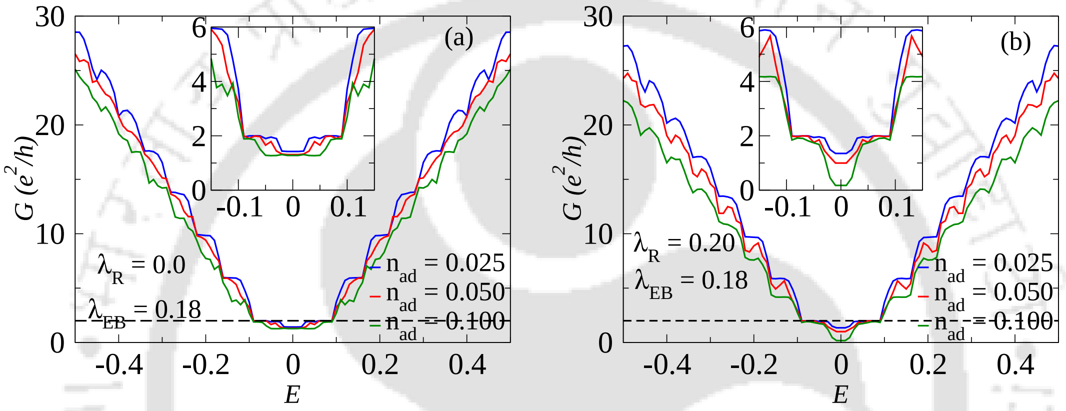

Figure 6.3: The two terminal charge conductance, G is plotted as a function of the Fermi energy, E (a) in the absence of Rashba SOC and (b) in the presence of Rashba SOC with strength, $\lambda_R = 0.2$. The strength of the exchange field is fixed in both the cases at $\lambda_{EB} = 0.18$. To visualize the behaviour of G near the zero of the Fermi energy, we plot the variation of G for a small range of the Fermi energy as shown in the insets.

We did not show the fluctuations in the charge conductance in Fig.6.3 in order to avoid cluttering of data. However, the fluctuations in the charge conductance, ΔG is plotted as a function of the Fermi energy separately as shown in Fig.6.4 for clarity. Fig.6.4(a) shows the variation of G in the absence of Rashba SOC and Fig.6.4(b) for a Rashba strength, $\lambda_R = 0.2$. In both cases, fluctuations increase with increasing of the adatom concentration. Rashba SOC suppresses the fluctuations in the charge conductance as seen from Fig.6.4(b). The spike-like behaviour in ΔG is due to the finite number of open channels in the leads and may be due to the spin precession effect[182,183]. For clarity, we have taken only two different adatom concentrations, namely, $n_{ad} = 0.025$ (denoted by blue color) and 0.1 (denoted by green color).

It is expected that in the absence of Rashba SOC, the exchange field generates only the z-component of the spin polarized conductance, as the exchange field contains only the z-component of the Pauli spin matrix (see Eq.(6.1)). However, the

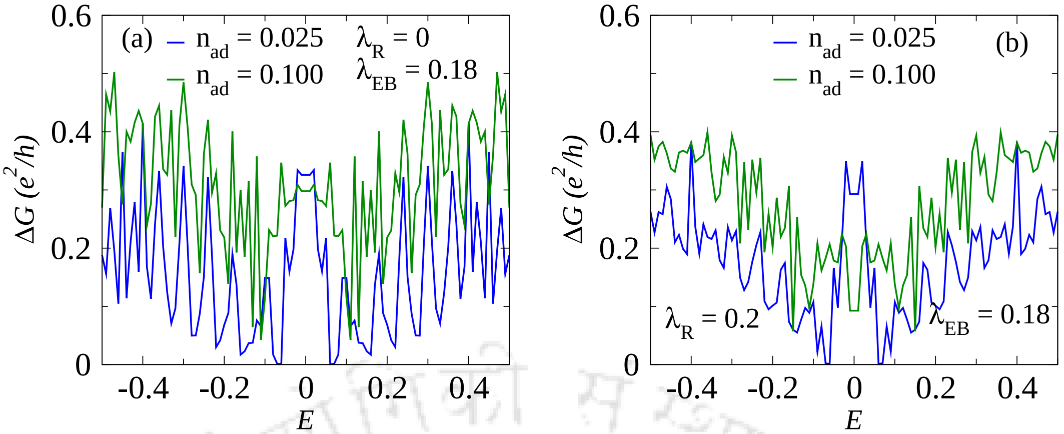

Figure 6.4: The fluctuations in the charge conductance, ΔG is plotted as a function of the Fermi energy, E for (a) $\lambda_R = 0$ and (b) $\lambda_R = 0.2$. Only two different adatom concentrations are taken, namely, $n_{ad} = 0.025$ and 0.1 for clarity.

inclusion of the Rashba SOC generates all the three components of the spin polarized conductance.

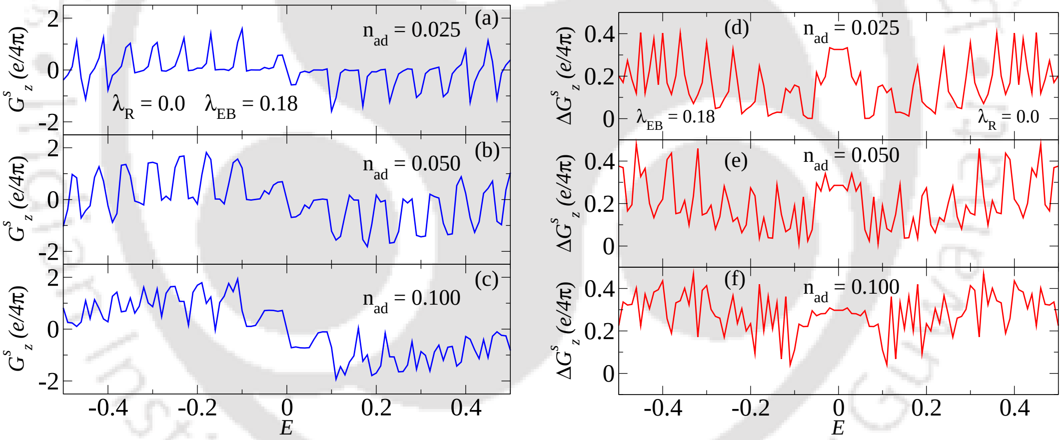

Figure 6.5: (a-c)The two terminal spin polarized conductance, G_z^s is plotted as a function of the Fermi energy in the absence of Rashba SOC for three different adatom concentrations, namely n_{ad} =0.025, 0.05 and 0.1. (d-f) Their corresponding fluctuations are plotted as a function of E.

Fig.6.5(a-c) shows the variation of the z-component of the spin polarized component, G_z^s (in units of $e/4\pi$) as a function of the Fermi energy, E in the absence of Rashba SOC for three different adatom concentrations. G_z^s is antisymmetric as a function of the Fermi energy owing to the electron-hole symmetry[135,171]. Even though we have considered very dilute adatom concentrations, still G_z^s acquires quite a large value in the absence of Rashba SOC. The spike-like nature as discussed before is due to the finite number of open channels in the leads. The fluctuations in

G_z^s, denoted by ΔG_z^s is plotted as a function of the Fermi energy, E as shown in Fig.6.5(d-f). ΔG_z^s is symmetric about $E = 0$. However, in the absence of Rashba SOC, ΔG_z^s is more or less independent of the adatom concentration.

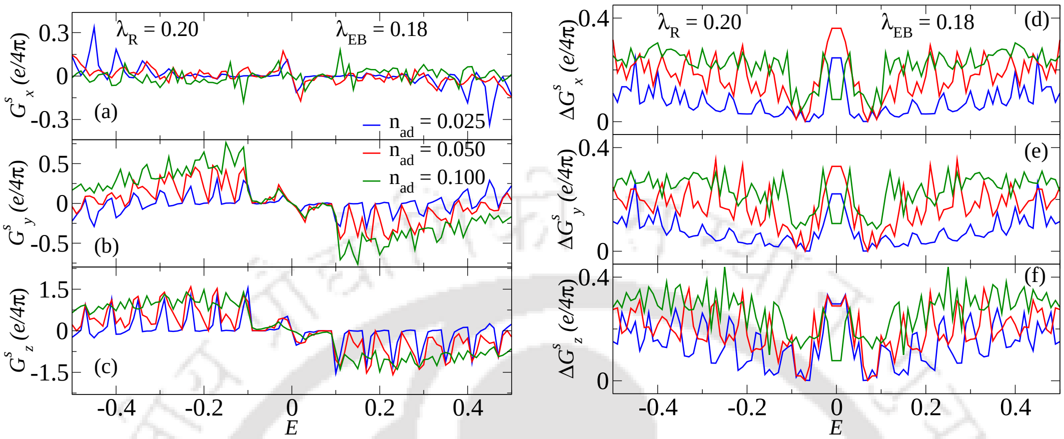

Figure 6.6: In presence of Rashba SOC, the three components of the spin polarized conductance (a) G_x^s, (b) G_y^s and G_z^s are plotted as a function of the Fermi energy. (d-f) Their fluctuations are plotted as a function of E. Now all the three components are finite.

The behaviour of all the three components of spin polarized conductance as a function of E in presence of Rashba SOC is plotted in Fig.6.6(a-c). The magnitude of the spin polarized conductance increases with increasing the adatom concentration. The z-component, namely G_z^s has a higher magnitude than the other two components of the spin polarized conductance. However, all of them are antisymmetric about $E = 0$, as they should be. The magnitude of G_z^s in presence of the Rashba SOC is lower than the values corresponding to those of in the absence of the Rashba SOC. The spike-like feature is most prominent in the behaviour of G_z^s and is marginally observed in G_y^s. Further, as we have already mentioned in Chapter 5, the fluctuations present in the data for spin polarized conductance are due to the finite size effects originating from the finite number of conducting modes present in the leads.

The behaviour of the corresponding fluctuations in the spin polarized conductance is shown in Fig.6.6(d-f). As the adatom concentration is increased, the fluctuations also increase. But the most interesting feature about the fluctuations is that all the three components, that is $\Delta G_i^s (i = x, y, z)$ have a unique behaviour as elaborated in the following. Even if the different components of the spin polarized conductance have different variations as a function of E and have different orders of magnitude for a particular strength of the exchange field in presence of Rashba SOC, yet the orders of magnitude of their fluctuations are almost same. Further, as usual, the fluctuations increases with increasing adatom concentration.

The inclusion of magnetic adatoms generates the exchange field and as a result, the time reversal symmetry is broken. Hence the system will no longer have a Kramer's doublet. This phenomena can be justified through the density of states (DOS) for different species, that is DOS for up and down spins. We denote the total density of states by DOS, the density of states coming from spin up electron by UDOS and that from spin down electron by DDOS. We also define the difference between the UDOS and DDOS by DiffDOS.

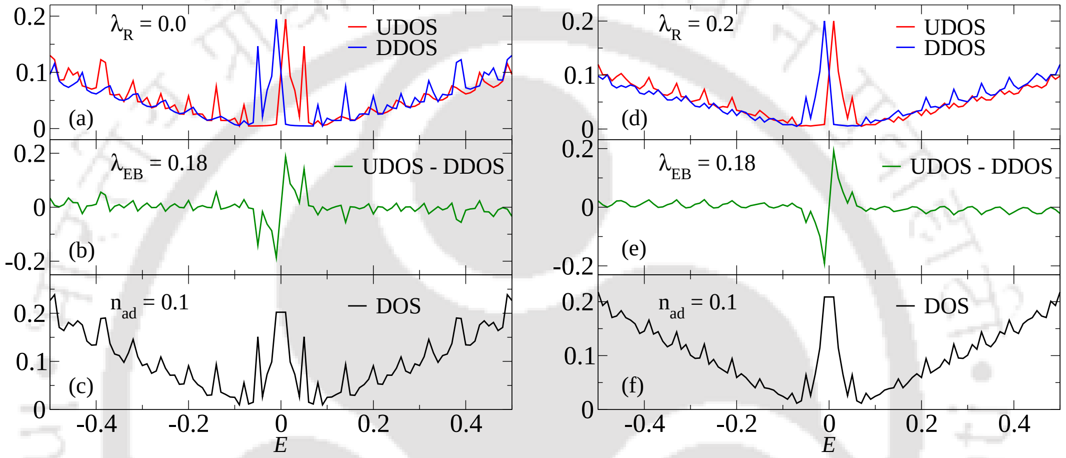

Figure 6.7: The density of states (DOS) for the spin up (UDOS) and spin down (DDOS) electrons are plotted as a function of the Fermi energy, E (a) for $\lambda_R = 0$ and (d) for $\lambda_R = 0.2$. The difference between UDOS and DDOS are plotted as a function of E (b) for $\lambda_R = 0$ and (e) for $\lambda_R = 0.2$. The behaviour of total DOS is plotted as a function of the Fermi energy (c) for $\lambda_R = 0$ and (e) for $\lambda_R = 0.2$. For clarity of presentation, we consider only a single adatom concentration, that is, $n_{ad} = 0.1$.

The variation of the DOS as a function of the Fermi energy is plotted in Fig.6.7 for a particular strength of the exchange field, $\lambda_{EB} = 0.18$. Fig.6.7(a) shows the behaviour of UDOS and DDOS in the absence of Rashba SOC and Fig.6.7(d) in presence of Rashba SOC. It is observed that UDOS is antisymmetric with respect to the DDOS as a function of the Fermi energy. The difference between UDOS and DDOS, that is, DiffDOS is plotted in Fig.6.7(b) and Fig.6.7(e) in the absence and presence of Rashba SOC respectively. In both cases UDOS $-$ DDOS is antisymmetric about $E = 0$. The total DOS, that is the sum of DOS due to spin up and spin down electrons is plotted in Fig.6.7(c) and Fig.6.7(f). DOS is symmetric about $E = 0$.

We can summarize the observations noted from the DOS data, as shown by the following set of properties,

$$\begin{aligned} \mathrm{UDOS(E)} &= \mathrm{DDOS(-E)} \\ \mathrm{DiffDOS(E)} &= -\mathrm{DiffDOS(-E)} \\ \mathrm{DOS(E)} &= \mathrm{DOS(-E)} \end{aligned} \tag{6.2}$$

In order to have a deeper look, we have also shown the local charge and spin currents for a fixed Fermi energy. Since the left lead acts as an input to the system, we are interested in the local charge and spin currents which have originated due to the left lead.

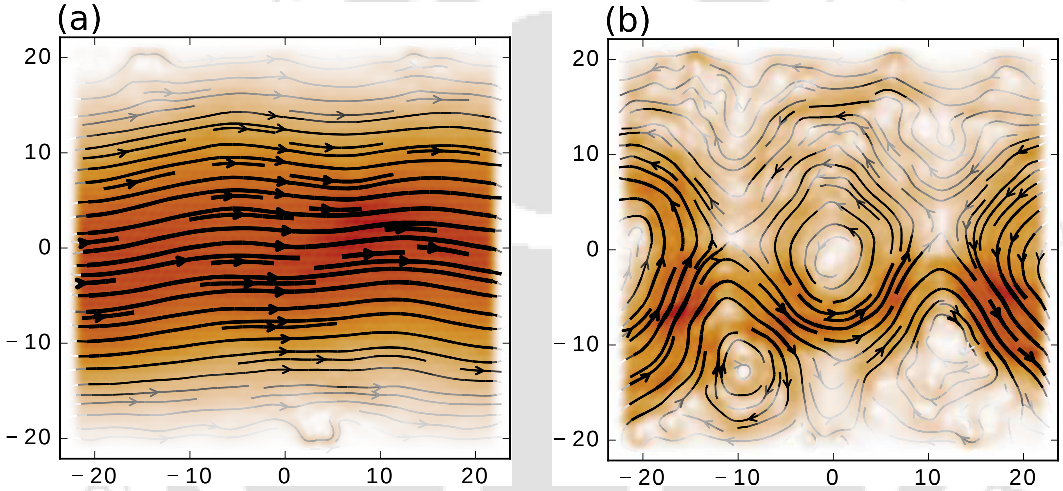

Figure 6.8: (a) The local charge current, J_0 and (b) the z-component of the local spin current are shown in the absence of Rashba SOC. Both the figures are obtained for the adatom concentration $n_{ad} = 0.1$ and we set the Fermi energy at $E = -0.09$ (in units of t). Figure (b) shows a presence of some centers around which J_z whirls.

Fig.6.8(a) shows the nature of the local charge current, J_0 in the absence of Rashba SOC for a fixed value (close to zero) of the Fermi energy, namely $E = -0.09$ (in units of t). Clearly, the local charge current is flowing from the left to the right lead without any distortion. In case of the spin currents, three components, namely J_x, J_y, J_z can exist. Since in the absence of Rashba SOC only z-component of the local spin current is present, we have calculated J_z as shown in Fig.6.8(b). The number of paths between left and right leads is less compared to the local charge current. Few of the paths are even circling around certain points signaling a vortex-like behaviour.

Since the inclusion of Rashba SOC generates the two other components of the spin polarized conductance, namely the x and y components, it will be meaningful to study the local spin currents of these components. The existence of all of these components should be beneficial for spintronic applications of magnetic adatom decorated GNRs.

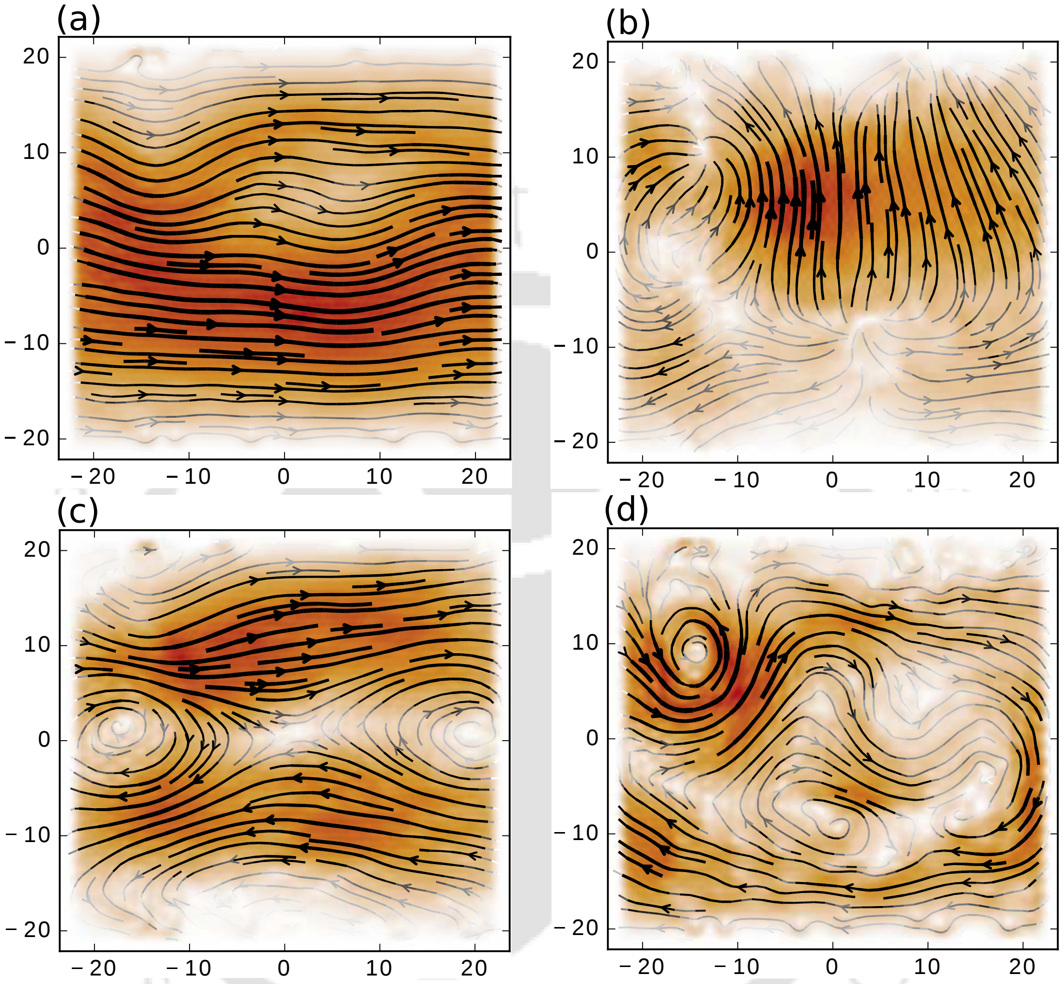

Figure 6.9: (a) The local charge current J_0, (b) the x-component of the local spin current, J_x, (c) the y-component of the local spin current, J_y and (d) the z-component of the local spin current, J_z are shown in the presence of Rashba SOC with strength $\lambda_R = 0.2$. The strength of the exchange field is $\lambda_{EB} = 0.18$. We set the Fermi energy at $E = -0.09$ and the adatom concentration in the present case is $n_{ad} = 0.1$. Vortex like features, similar to Fig.6.8(b) are noticed in the J_x, J_y and J_z plots.

For this, we set, as before, the strength of the Rashba SOC at $\lambda_R = 0.2$ and fixed the energy at $E = -0.09$. The local charge and spin currents are shown in Fig.6.9. The local charge current, J_0 is again flowing between left and right leads as shown in Fig.6.9(a), which reveals that J_0 is almost independent of the Rashba SOC which is understandable. Fig.6.9(b),(c) and (d) show respectively J_x, J_y and J_z. If we recall Fig.6.6, where $G_i^s(i = x, y, z)$ are plotted as a function of the Fermi energy, the

x-component of the spin polarized conductance has the lowest magnitude compared to the other two components. This can be explained from Fig.6.9(b). Here we see that the number of clear paths between left and right leads are very less compared to the paths corresponding to J_y and J_z. As a result, G^s_x has lesser magnitude than that of G^s_y and G^s_z.

One point should be mentioned here that all the plots in Fig.6.8 and Fig.6.9 are obtained for a single configuration corresponding to $n_{ad} = 0.1$. Another configuration or taking an average over several configurations will change the current distribution between the leads but will have similar implications as checked by us.

6.2.2 Four terminal (4T)

Having emphasized upon the conductance characteristics of a 2T GNR, it is useful to compare and contrast the conductance properties for 4T devices.

To begin with the results in case of a 4T device, we shall remind ourselves that the setup for measuring the longitudinal conductance (G) and spin Hall conductance (G_{SH}). As shown in Fig.6.2, an electric current is allowed to pass between terminals 1 and 2, and the longitudinal conductance is measured. Terminals 3 and 4 are the voltage probes, hence there will be no charge current flowing through them. The spin Hall conductance is measured between terminals 3 and 4.

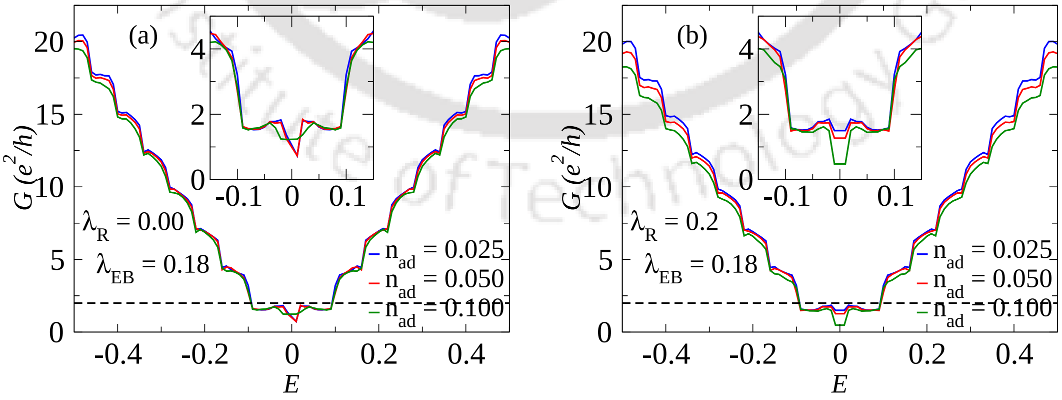

Figure 6.10: The four terminal charge conductance, G is plotted as a function of the Fermi energy, E (a) in the absence of Rashba SOC and (b) in the presence of Rashba SOC with strength, $\lambda_R = 0.2$. The strength of the exchange field is fixed in both the cases at $\lambda_{EB} = 0.18$. To visualize the behaviour of G near the zero of the Fermi energy, we plot the variation of G for a small range of the Fermi energy as shown in the inset.

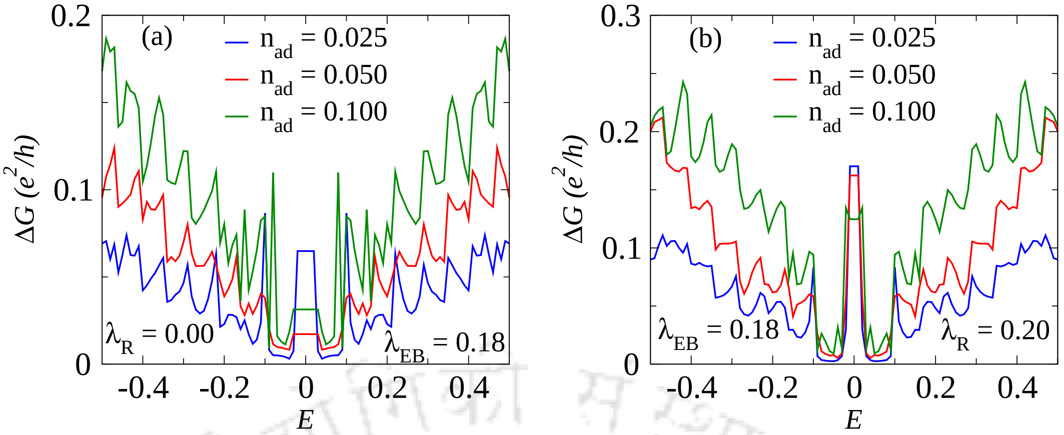

Figure 6.11: The fluctuations in the charge conductance, ΔG is plotted as a function of the Fermi energy, E for (a) $\lambda_R = 0$ and (b) $\lambda_R = 0.2$. Three different adatom concentrations are taken, namely, $n_{ad} = 0.025$, 0.05 and 0.1.

The behaviour of the charge conductance, G for a 4T device is studied as a function of the Fermi energy, E as shown in Fig.6.10 for two different cases as earlier, namely, $\lambda_R = 0$ in Fig.6.10(a) and $\lambda_R = 0.2$ in Fig.6.10(b). The strength of the exchange field is kept fixed as in case of two terminal case, that is at $\lambda_{EB} = 0.18$. G is symmetric around the zero of the Fermi energy and shows a necklace-type pattern for both the cases. However, the behaviour of G close to zero of the Fermi energy is different for two different values of λ_R. We plot G for a small range of the Fermi energy in the vicinity of $E = 0$ as shown in the inset in Fig.6.10. In the absence of Rashba SOC, G always remains non-zero. On the other hand, in presence of Rashba SOC, G tends to have lower values near $E = 0$ as we increase the adatom concentration. One can expect a conventional insulating behaviour in the vicinity of $E = 0$ in presence of Rashba SOC if we increase the adatom concentration beyond $n_{ad} = 0.1$.

There is a crucial difference between the 2T and 4T devices with regard to the plateau at $2e^2/h$ in the vicinity of the zero of the Fermi energy implying the existence or absence of a quantum spin Hall phase. As discussed earlier, there is a fairly flat plateau for a 2T GNR without magnetic adatoms, which is visibly absent for a 4T GNR (see Fig.6.10 and the insets) owing to the absence of edges in the sample which subsequently rules out the presence of edge states. This is another minor difference, where, in a 2T device, we have observed G to completely vanish at $n_{ad} = 0.1$, while in the 4T GNR, it is small but finite at $n_{ad} = 0$, however would eventually vanish for $n_{ad} > 0.1$.

The fluctuations in the charge conductance, ΔG is plotted in Fig.6.11(a) in the absence of Rashba SOC and in Fig.6.11(b) in presence of Rashba SOC. In each of the plots, ΔG falls off as we come close to $E = 0$, from either side of the band and again increases near $E = 0$. The fluctuations increase as we increase the adatom concentration. By comparison of the two plots, we observe that the inclusion of Rashba SOC causes larger fluctuations than the corresponding case where Rashba SOC is absent.

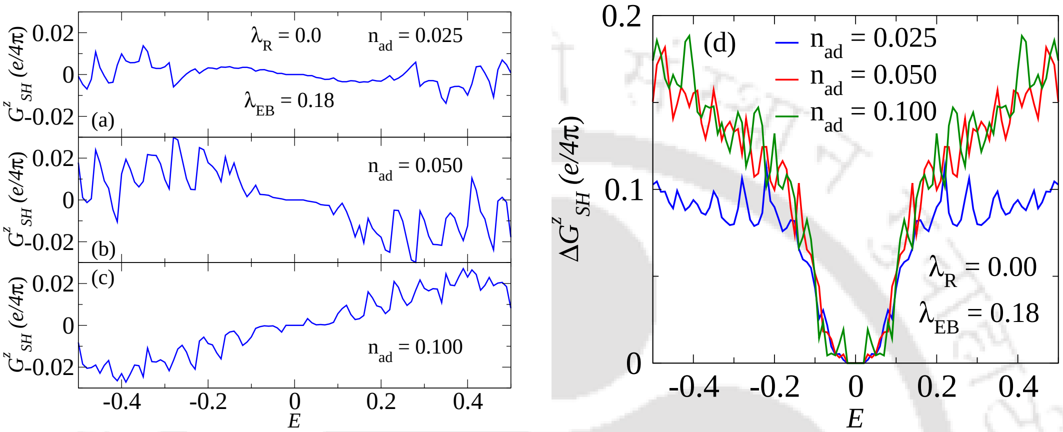

Figure 6.12: (a-c) The four terminal spin polarized conductance, G^s_z is plotted as a function of the Fermi energy, E in the absence of Rashba SOC for three different adatom concentrations. (d) Their corresponding fluctuations are plotted as a function of E.

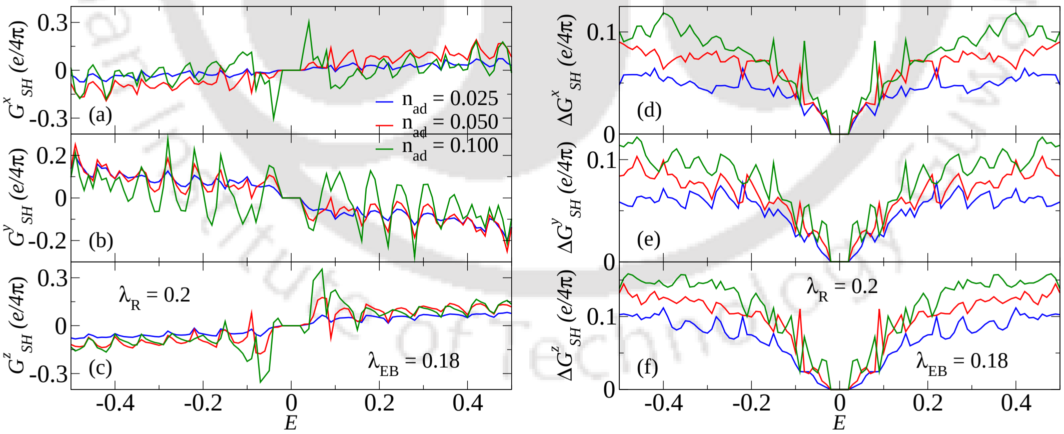

Figure 6.13: In presence of Rashba SOC, the three components of the spin polarized conductance (a) G^s_x, (b) G^s_y and G^s_z are plotted as a function of the Fermi energy, E. (d-f) Their fluctuations are plotted as a function of E.

Same as that of the spin polarized conductance, the spin Hall conductance also has three components, namely G^x_{SH}, G^y_{SH} and G^z_{SH}. Since the x and y-components of the spin Hall conductance are absent in the absence of Rashba SOC, we have shown only the variation of G^z_{SH} in units of $e/4\pi$ as a function of the Fermi energy in Fig.6.12(a-c)and corresponding fluctuations in Fig.6.12(d).

G^z_{SH} is plotted for three different adatom concentrations separately for better clarity. The behaviour of G^z_{SH} is antisymmetric about $E = 0$ and the magnitude (irrespective of the sign factor) increases as the adatom density is enhanced. The maximum values of G^z_{SH} are observed on either side of the zero of the Fermi energy and close to $E = 0$, the value decreases. The corresponding fluctuations are shown in a single plot in Fig.6.12(d). As expected, with increasing the adatom concentration, ΔG^z_{SH} increases. Another important point to be noted here is that there is a finite region about the zero energy where G^z_{SH} and ΔG^z_{SH} are strictly zero irrespective of the adatom concentration. This vanishing of the conductance and its corresponding fluctuations are due to the availability of single transmission mode[171,174].

The effect of the inclusion of Rashba SOC on the three components of the spin Hall conductance is observed in Fig.6.13(a-c). All of them are antisymmetric about $E = 0$. Their magnitudes increase as the adatom concentration is increased. Though the behaviour of the different components of the spin Hall conductance has different variations as a function of the Fermi energy, their orders of magnitude are similar. The fluctuations in the spin Hall conductance are plotted in Fig.6.13(d-f) as a function of the Fermi energy. as observed the case in the absence of Rashba SOC, in the present case, G^x_{SH}, G^y_{SH} and G^z_{SH} have similar variations with E, that is they increase with increasing adatom concentrations. Further, their orders of magnitude are also same.

The DOS plots in the absence of Rashba SOC are shown in Fig.6.14(a-c) and in the presence of Rashba SOC in Fig.6.14(d-f). UDOS (for the up spin) and DDOS (for the down spin) are antisymmetric to each other as we have observed in case of a two terminal device. The magnitudes of UDOS and DDOS are higher at larger values of E as shown in Fig.6.14(a) and Fig.6.14(d), and in both the cases, that is, in presence and absence of Rashba SOC, their magnitudes seem to be independent of the strength of Rashba SOC. The difference between UDOS and DDOS, DiffDOS (= UDOS - DDOS) has an antisymmetric variation as a function of the Fermi energy and has somewhat larger oscillatory behaviour in presence of RSOC than that in the absence of RSOC. Also, the total DOS is symmetric about $E = 0$. Basically, all the three quantities are in good agreement with Eq.(6.3) both in the absence and presence of Rashba SOC.

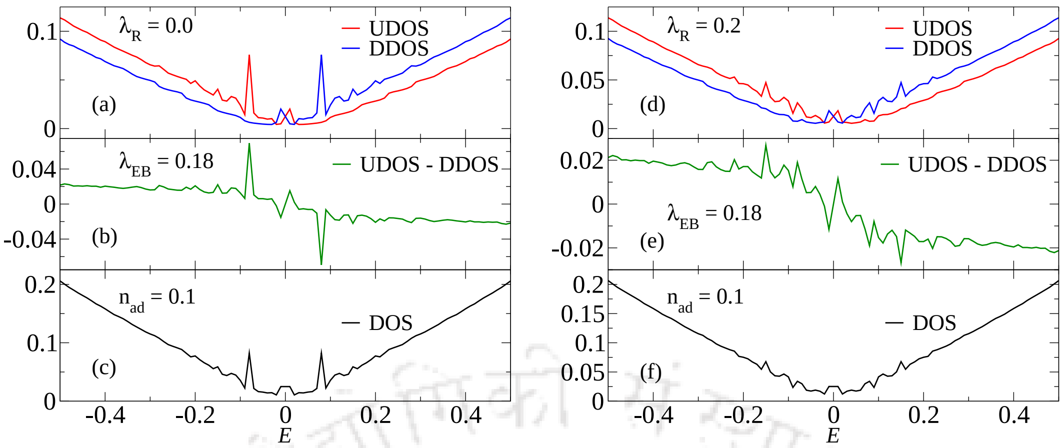

Figure 6.14: The four terminal density of states (DOS) for the spin up (UDOS) and spin down (DDOS) electrons are plotted as a function of the Fermi energy (a) for $\lambda_R = 0$ and (d) for $\lambda_R = 0.2$. The difference between UDOS and DDOS are plotted as a function of E, (b) for $\lambda_R = 0$, and (e) for $\lambda_R = 0.2$. The behaviour of total DOS is plotted as a function of the Fermi energy (c) for $\lambda_R = 0$ and (e) for $\lambda_R = 0.2$. For clarity of presentation we have considered only a single adatom concentration, $n_{ad} = 0.1$.

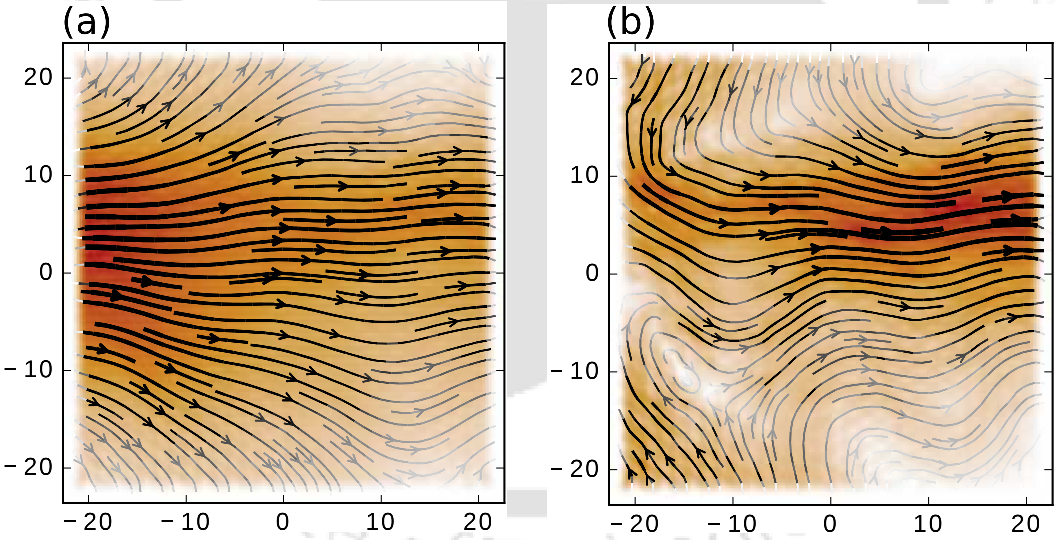

Figure 6.15: (a) For the four terminal case, the local charge current, J_0 and (b) the z-component of the local spin current are shown in the absence of Rashba SOC. Both the figures are obtained for the adatom concentration $n_{ad} = 0.1$ and we set the Fermi energy at $E = -0.09$ (in units of t).

Finally, the local charge current and the z-component of the local spin current are shown in Fig.6.15(a) and Fig.6.15(a) respectively in the absence of Rashba SOC. For the local charge current, it is observed that, though the transverse leads are voltage probes, the charge current still flows between lead 1 and lead 3. In another word, the charges accumulate at the transverse edges of the sample and as a result, less charge current flows between terminals 1 and 2. This, in turn, reduces the charge conductance in case of a 4T device than the 2T case. The z-component of the local spin current is clearly flowing from terminals 1 to 3 and between terminal 1 to 4. As a result, the non-zero G_{SH}^{z} occurs due to the presence of the exchange field.

The local charge and spin currents are shown in Fig.6.16 in presence of Rashba SOC. The local charge current, J_0 flows between the left and the right leads (terminals 1 and 2 respectively) as shown in Fig.6.16(a). We observe that J_0 is almost independent of the Rashba SOC. This explains why the charge conductance is independent of the Rashba SOC as shown in Fig.6.10(a) and Fig.6.10(b).

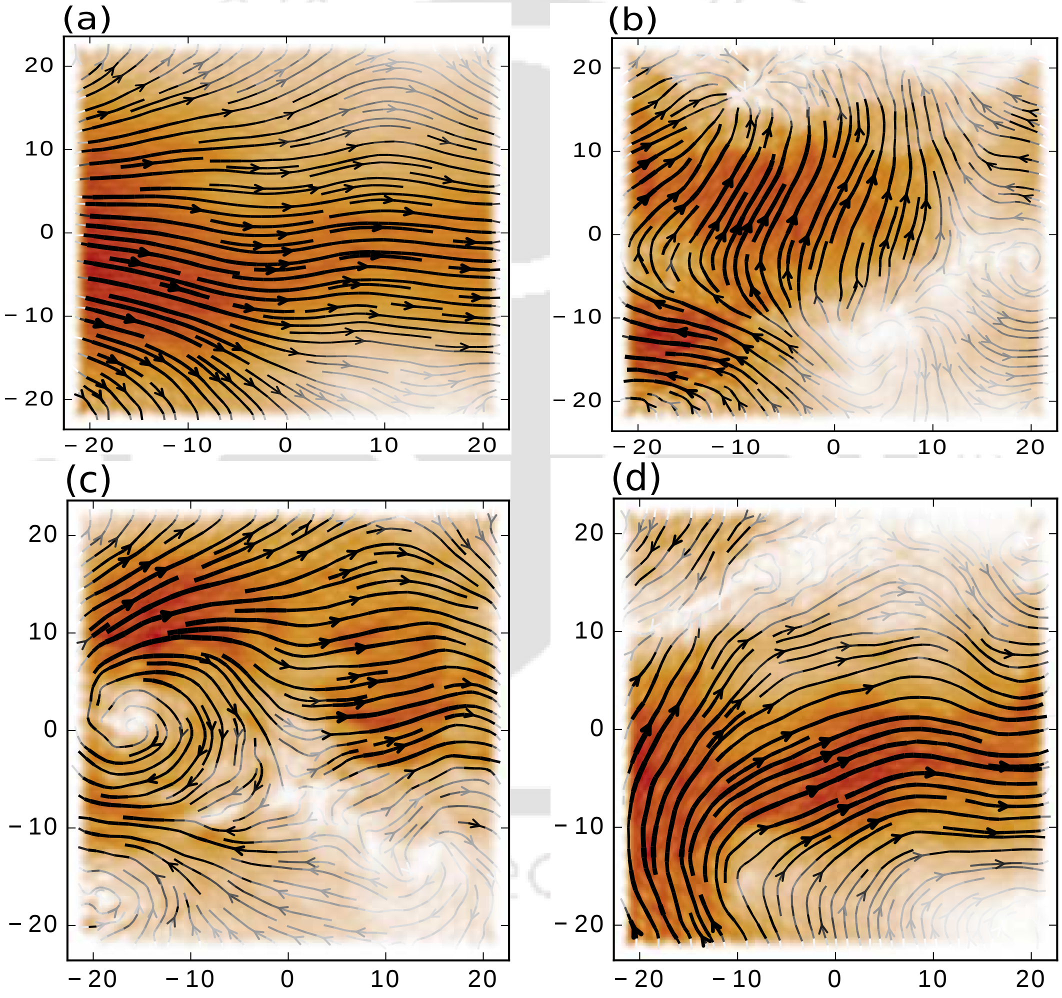

Figure 6.16: (a) The local charge current J_0, (b) the x-component of the local spin current, J_x, (c) the y-component of the local spin current, J_y and (d) the z-component of the local spin current, J_z are shown in the presence of Rashba SOC with strength $\lambda_R = 0.2$. The strength of the exchange field is $\lambda_{EB} = 0.18$. We set the Fermi energy at $E = -0.09$ and the adatom concentration in the present case is $n_{ad} = 0.1$.

Fig.6.16(b), (c) and (d) show respectively the local currents, namely J_x, J_y and

J_z. We observe that the magnitude of the z-component of the spin Hall conductance (see Fig.6.12(a-c)) is one order magnitude lower than any one of the components of SHC in presence of Rashba SOC, which can be explained as in the following. From Fig.6.16(b-c), the number of paths between terminal 1 and either of terminals 3 or 4 are more than the absence of Rashba SOC case as shown in Fig.6.15(b). As a result, the amount of spin current will be less in the absence of Rashba SOC.

6.3 Conclusion

In the present chapter, we have studied the behaviour of the charge and spin transport properties in graphene nanoribbon with magnetic adsorbates both in the case of a two terminal and a four terminal GNR. Specifically for the two terminal case, we study the charge and spin polarized conductance and for the four terminal case, the spin Hall conductance. In all the cases we found that the charge conductance is symmetric about the zero of the Fermi energy, while the spin polarized conductances (for two terminal case) and the spin Hall conductance (for four terminal case) are antisymmetric about the zero of the Fermi energy. The fluctuations of the charge and spin conductances show systematic behaviour, that is they increase with increasing adatom concentration. We have also studied the DOS behaviour and they are alike in both the two and the four terminal cases. The local charge current is found to be independent of the strength of Rashba SOC, while the three components of the local spin currents are sensitive to Rashba SOC that is generated by the magnetic adatoms. Further the z-component of the spin polarized conductance for a 2T GNR is larger by approximately a factor of 5 compared to its 4T counterpart, while the other two components are nearly same for the 2T and 4T devices. Of course, a 4T device permits observations of a spin Hall conductance, which is absent in the case of a 2T GNR. Moreover the conductance properties of a 4T setup have lesser fluctuations.

The increase in the components of the spin polarized conductances in magnetic decorated GNRs with Rashba SOC signal a larger spin current flowing in the sample and hence must have greater utility as possible spintronic devices.

Chapter 7

Six terminal Graphene Nanoribbons: Interplay of Rashba coupling and magnetic field

Having done an extensive study of the spin Hall effect in Rashba coupled electronic devices, we intend to incorporate the effect of an external magnetic field. It is clear from the discussion of the preceding chapters that the spin-orbit coupling upholds the time reversal symmetry which is now going to be explicitly broken by the magnetic field. Besides, an inclusion of the external magnetic field, in addition to the spin-orbit coupling, provides a platform to explore an interplay between the two. The former gives rise to the quantum Hall effect and the latter is the origin of spin Hall effect.

The quantum Hall effect[39], one of the finest discoveries in condensed matter physics[5], occurs typically below 1 K in a two-dimensional electronic system in presence of a strong perpendicular magnetic field. The Hall resistance is quantized integer and fractional multiples of h/e^2 with a great accuracy, one part per million, and due to this impressive accuracy, it is designated as a standard of resistance[184]. The integer quantum Hall effect (IQHE) can be explained without invoking inter-particle interactions, while the fractional counterpart, conventionally denoted by FQHE demands an interacting framework.

On a parallel front, the spin analog of the quantum Hall effect is the spin Hall effect (SHE), which was observed in p-doped semiconductors by Murakami *et al.*[37] and in Rashba spin-orbit coupled (RSOC) two-dimensional electron system (2DES) by Sinova *et al.*[38]. Since graphene is under focus for our thesis, we wish to scrutinize it more closely for graphene. The Rashba spin-orbit interaction couples the spin degree of freedom and the orbital motion of the electron in graphene[29]. However, the strength of the intrinsic Rashba SOC is quite small in pristine graphene (of the order of μeV). But recent observations showed that the strength of the Rashba SOC can be enhanced by a few order of magnitude, that is up to 100 meV via Au intercalation at the graphene-Ni interface[185]. Further, a Rashba splitting about 225 meV in epitaxial graphene layers grown on the surface of Ni[186] and a giant Rashba SOC from Pb intercalation at the graphene-Ir surface[187] are noted in experiments. In view of this, the above discussion has implications for the spintronic applications of a graphene nanoribbon (GNR).

A fundamental principle of quantum mechanics states that time reversal symmetry always preserves the Kramer's degeneracy of a function, $\psi(\mathbf{k},\sigma)$ which implies that it is same as its complex conjugate $\psi^*(\mathbf{k},\sigma)$, $\mathbf{k}$ and σ being the wave vector and electron spin respectively. The Kramer's degeneracy remains unaffected when the spin-orbit interaction term is included in the Hamiltonian[50]. But in presence of a magnetic field, the time reversal symmetry is broken[51]. As a result, the system will no longer have a Kramer's doublet. Motivated by such distinct physics prevalent for spin-orbit coupling and the magnetic field, one can expect an interplay between the magnetic field and Rashba SOC in a GNR. Thus we have studied the conductance properties for both spin and charge degrees of freedom in a six terminal GNR in presence of Rashba SOC and a magnetic field in this chapter. A six terminal device as shown in Fig.7.1 is called a Hall bar and is routinely used in Hall voltage measurements.

We organize this chapter as follows. In the following section, we present the theoretical formalism leading to the expressions for the charge and spin Hall conductances using the well-known Landauer-Büttiker formula[1,133]. Hence we include an elaborate discussion of the results, Where, we have tried to resolve few issues, such as whether the quantum Hall state (specific to the magnetic field) exists in presence of Rashba SOC or how the spin Hall conductance (specific to Rashba SOC) behaves in presence of a magnetic field and so on.

7.1 Theoretical formulation and model

The schematic view of six terminal graphene nanoribbon is shown in Fig.7.1 which we have employed here to observe the integer quantum Hall and spin Hall effects. The six leads are shown by the red color. The black circles denote the scattering region. Leads 1-4 are the armchair GNR (AGNR), while leads 5 and 6 are the zigzag

GNR (ZGNR). The width of the leads can be determined as shown in Fig.7.2. In Fig.7.1, the periodic nature of lead-1 is armchair (in the y direction) and along the width of the lead (in the x direction) it has a zigzag shape. On the other hand, the periodicity of lead-1 is zigzag (in the $-x$ direction) and the width is in armchair shape (in the y direction). Hence Fig.7.2(a) denotes an AGNR lead with width 11Z (Z : Zigzag) and Fig.7.2(b) stands for the ZGNR with width 6A (A : Armchair). The scattering region has a rectangular shape and along the y direction it has an armchair shape, while along the x direction it has a zigzag shape. Hence we represent our scattering region as having dimension of N_xZ-N_yA = 25Z-16A.

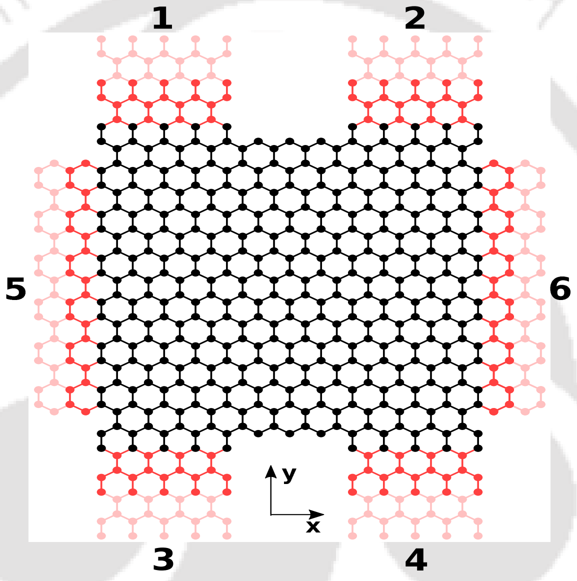

Figure 7.1: Schematic view of a six terminal graphene nanoribbon. The honeycomb lattice denoted by the black circles is the scattering region. Leads are denoted by the red circles. The leads are semi-infinite in nature and free of any kind of interactions. Leads 1-4 are the armchair leads and lead 5 and lead 6 are the zigzag.

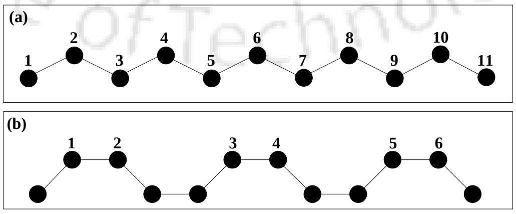

Figure 7.2: Schematic diagram showing the widths of AGNR and ZGNR leads. (a) AGNR lead with a width 9 units and (b) ZGNR lead with a width 6 units.

The geometry in Fig.7.1 is used to compute the Hall and longitudinal conductance in presence of a perpendicular magnetic field. We also include a Rashba SOC (as it is intrinsic in graphene, albeit small) in order to observe spin Hall effect.

The tight binding Hamiltonian in presence of magnetic field and Rashba SOC can be written as,

$$H = \sum_{\langle mn \rangle} t_{mn} c_m^\dagger c_n + i\lambda_R \sum_{\langle mn \rangle} c_m^\dagger \left(\mathbf{s} \times \hat{\mathbf{d}}_{mn}\right)_z c_n \tag{7.1}$$

where $c_m^\dagger = \begin{pmatrix} c_{m\uparrow}^\dagger & c_{m\downarrow}^\dagger \end{pmatrix}$ are the creation operators of electrons at a site m. t_{mn} represents the hopping strength between the nearest-neighbor sites. The effect of the magnetic field is incorporated in the hopping term through the Peierl's phase factor[188,189] and can be written as,

$$t_{mn} = -te^{-ie/\hbar \int_m^n \mathbf{A}\cdot dl} \tag{7.2}$$

where t is the hopping strength in absence of a magnetic field and for graphene $t = 2.7$ eV[40], and $\mathbf{A}$ denotes the vector potential. Since the magnetic field is directed along z-direction, for the vector potential, $\mathbf{A}$ we choose the Landau gauge by assuming $\mathbf{A} = (-By, 0, 0)$ (B: magnetic field). The second term is the nearest neighbour Rashba[29] term which explicitly violates $z \to -z$ symmetry. λ_R is the strength of the spin-orbit coupling.

In order to observe IQHE, a current I is allowed to pass between terminals 5 and 6. The Hall resistance, R_H is measured between terminals 2 and 4 and the longitudinal resistance is measured between terminals 1 and 2. These two resistances are denoted by,

$$R_H = \frac{V_2 - V_4}{I_5} \quad \text{and} \quad R_L = \frac{V_1 - V_2}{I_5} \tag{7.3}$$

Using R_H and R_L, we can determine the Hall and longitudinal conductances from the following expressions[190],

$$\sigma_{xx} = \frac{R_L}{R_L^2 + R_H^2} \quad \text{and,} \quad \sigma_{xy} = \frac{R_H}{R_L^2 + R_H^2} \tag{7.4}$$

where σ_{xx} is the longitudinal conductance and σ_{xy} is the Hall conductance.

In case of SHE, the current is allowed to pass through terminals 1 and 3, and hence the spin current flowing between terminals 5 and 6 is measured. We define the spin Hall conductance as,

$$G_{SH} = \frac{\hbar}{2e} \frac{I_5^s}{V_1 - V_3} \tag{7.5}$$

where I_5^s is the spin current flowing through terminal 5.

Following the Landauer-Büttiker formula[1,133], the charge and spin currents can be calculated from the following expression[168,169],

$$I_p^{s_\alpha} = \frac{e^2}{h} \sum_q \mathrm{Tr}\left[\hat{\sigma}_\alpha \Gamma_q \mathcal{G}_R \Gamma_p \mathcal{G}_A\right] (V_p - V_q) \tag{7.6}$$

where, $\hat{\sigma}_\alpha = (\sigma_0, \sigma_x, \sigma_y, \sigma_z)$. σ_0 is a 2×2 identity matrix and $\sigma_x, \sigma_y, \sigma_z$ are the Pauli matrices. σ_0 gives the usual charge current, while the Pauli matrices yield the spin currents polarized in respective directions. $\mathcal{G}_{R(A)}$ is the retarded (advanced) Green's function. Γ_p are the coupling matrices representing the coupling between the central region and the p-th lead. They are defined by the relation[2],

$$\Gamma_p = i\left[\Sigma_p - (\Sigma_p)^\dagger\right] \tag{7.7}$$

Here Σ_p is the retarded self-energy associated with the p-th lead. The self-energy contribution is computed by modeling each terminal as a semi-infinite perfect wire[102].

7.2 Results and Discussion

We have investigated the effect of the magnetic field and Rashba SOC in a six terminal graphene nanoribbon on the experimentally measurable conductance properties, namely the longitudinal conductance (σ_{xx}), the charge Hall conductance (σ_{xy}) and the spin Hall conductance (G_{SH}).

Before we get ahead with the discussion of the results, we briefly describe the values of different parameters used in our calculation. Throughout our work, we set the width of AGNR leads (leads 1-4 in Fig.7.1) as 49Z and the width of ZGNR leads (leads 5-6 in Fig.7.1) as 52A. As mentioned earlier, ZGNR leads will have widths which are of the armchair shape and vice versa. We take the scattering region as 101Z-60Z (see Fig.7.1). We set the hopping term, $t = 2.7$ eV. All the energies are measured in the unit of t. The charge Hall and longitudinal conductances are measured in units of $\frac{e^2}{h}$. The spin Hall conductance is measured in units of $\frac{e}{4\pi}$. Also the lattice constant, a is taken to be unity. The strength of the magnetic field, B is measured in units of $1/a^2$. For most of our numerical calculations, we have used KWANT[93].

The IQHE in graphene nanoribbon in presence of externally applied magnetic field is observed in Fig.7.3, where we have plotted the longitudinal and charge Hall conductances together in the same plot as a function of the inverse of the strength of the magnetic field, $1/B$ for a fixed value of the Fermi energy, namely $E = 2$. Here we have considered $\lambda_R = 0$. The red curve stands for the charge Hall conductance (σ_{xy}) and the blue one for the longitudinal conductance (σ_{xx}). σ_{xy} increases in discrete

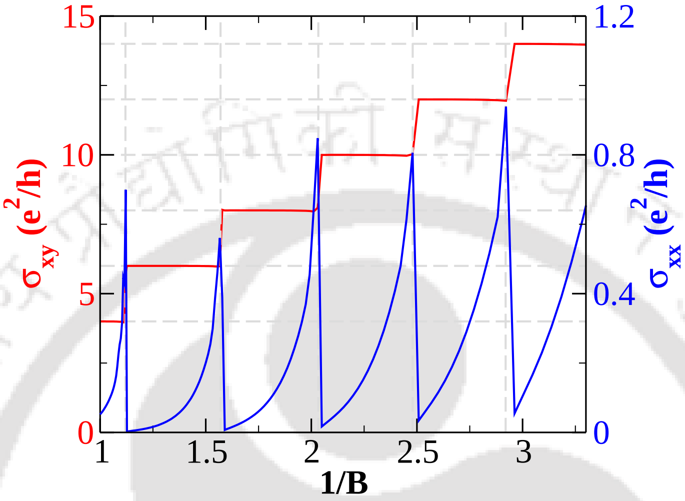

Figure 7.3: The charge Hall conductance (σ_{xy}, denoted by red color) and the longitudinal conductance (σ_{xx}, denoted by blue color) are plotted as a function of the inverse of the magnetic field strength, ($1/B$). We fixed the Fermi energy at $E = 2t$. σ_{xy} shows discrete step-like feature. σ_{xx} takes a peak whenever the Hall conductance goes from one step to the next.

steps as it should for IQHE. The charge Hall conductance is thus quantized in units of $2ne^2/h$ ($n = 1, 2, 3..$), where the 2 factor comes due to the spin degeneracy. The longitudinal conductance (shown by blue color) acquires a peak whenever σ_{xy} goes from one plateau to the next one. Apart from that, the value of σ_{xx} stays close to zero throughout the $1/B$ range.

The behaviour of the charge Hall and longitudinal conductances in presence of Rashba SOC is shown in Fig.7.4. Here we set the Fermi energy again at $E = 2$ (in units of t) and take two different strength of RSOC, namely, $\lambda_R = 0.05$ and 0.1. $\lambda_R = 0$ case is plotted for comparison. Fig.7.4(a) shows the behaviour of charge Hall conductance as a function of $1/B$. Even if the inclusion of RSOC destroys the perfectly flat plateau of the IQHE, still plateaus with much smaller width are observed. The width of these plateaus decreases as we increase the strength of RSOC. On the other hand, as shown in Fig.7.4(b), the peak longitudinal conductance increases in presence of the Rashba SOC. However, the peaks now broaden and the fall off of σ_{xx} becomes more gradual. Also, we observe fluctuations in the data for longitudinal conductance at large values of the magnetic field.

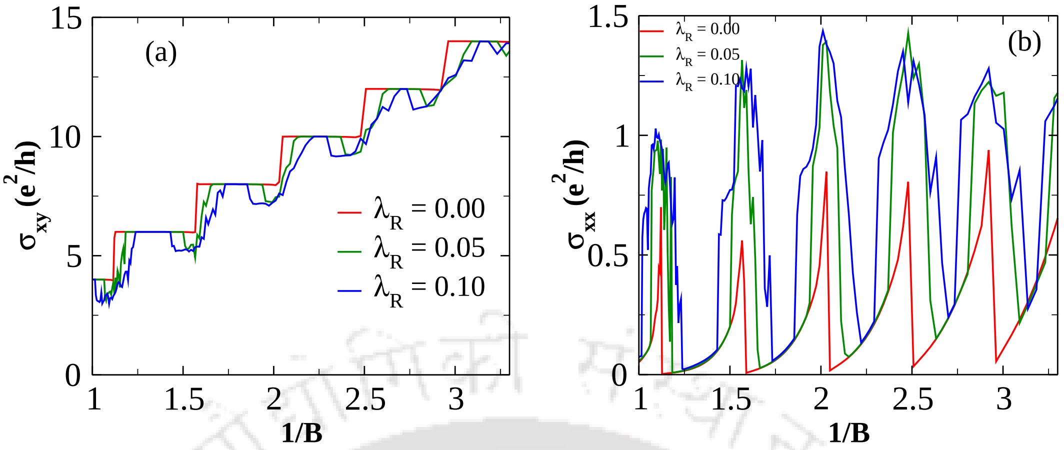

Figure 7.4: (a) σ_{xy} and (b) σ_{xx} are plotted as a function of $1/B$ in presence of Rashba SOC. The IQH effect is destroyed in presence of Rashba SOC. The behaviour of the longitudinal conductance also deviates from the nature observed in the absence of Rashba SOC.

The local density of states (LDOS) is plotted in Fig.7.5(a) in the absence and (b) in presence of a magnetic field with strength $B = 0.1$ (in units of $1/a^2$, a: lattice constant). We fixed the Rashba SOC strength at $\lambda_R = 0.1$ and the Fermi energy at $E = 2$. Throughout the system, the LDOS is almost same in the absence of the magnetic field. But in presence of the magnetic field, the charges accumulate at the transverse edges of the sample, as a result, the Hall voltage is generated. Fig.7.5(b) corroborates such a scenario, where the edges acquire deeper colours showing enhanced charge densities.

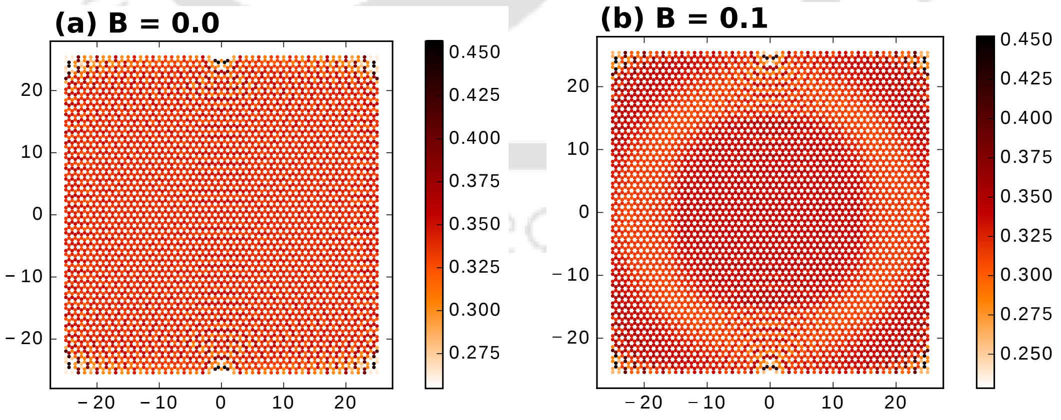

Figure 7.5: The local density of states (LDOS) is shown for two different cases. (a) Absence of magnetic field with $\lambda_R = 0.1$ and (b) in presence of magnetic field with strength $B = 0.1$ (in units of $1/a^2$, a: lattice spacing) and with the same strength of RSOC. The latter case showing the charge accumulation at the transverse edges.

The magnetic field does not preserve the time reversal symmetry and creates a

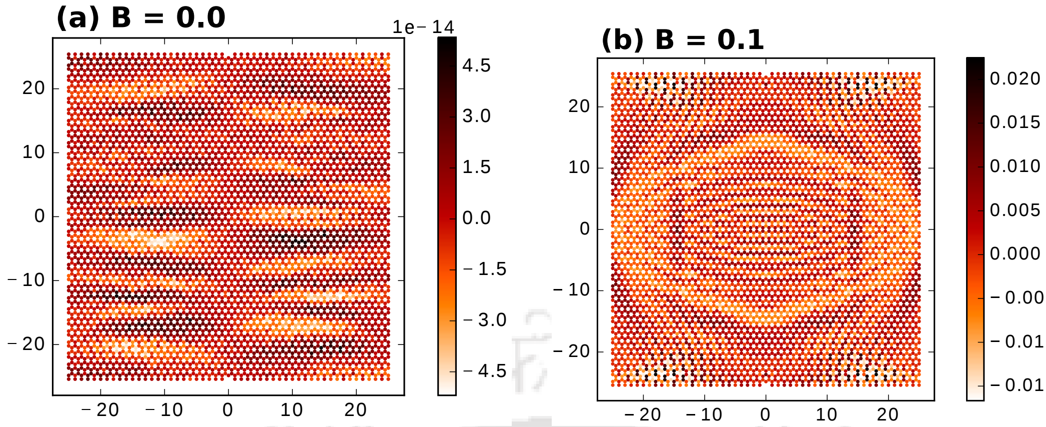

Figure 7.6: The difference between the up and down spin LDOS (DiffLDOS) is shown for two different cases. (a) The absence of magnetic field with $\lambda_R = 0.1$ and (b) in presence of magnetic field with strength $B = 0.1$ and with the same strength of RSOC. The inclusion of magnetic field shows a non-zero DiffLDOS.

biased environment for one kind of spin as compared to the other, we thus have plotted the difference between the up and down spin LDOS (we call it as DiffLDOS) in Fig.7.6. As in Fig.7.6(a), when the magnetic field is absent in the system, DiffLDOS is completely zero (shown as $\sim 10^{-14}$ in Fig.7.6(a)), which reflects the presence of time reversal symmetry. As we include the magnetic field, the time reversal symmetry is violated, and DiffLDOS starts to acquire non-zero values. The maximum value of the DiffLDOS appears at the transverse edges of the sample.

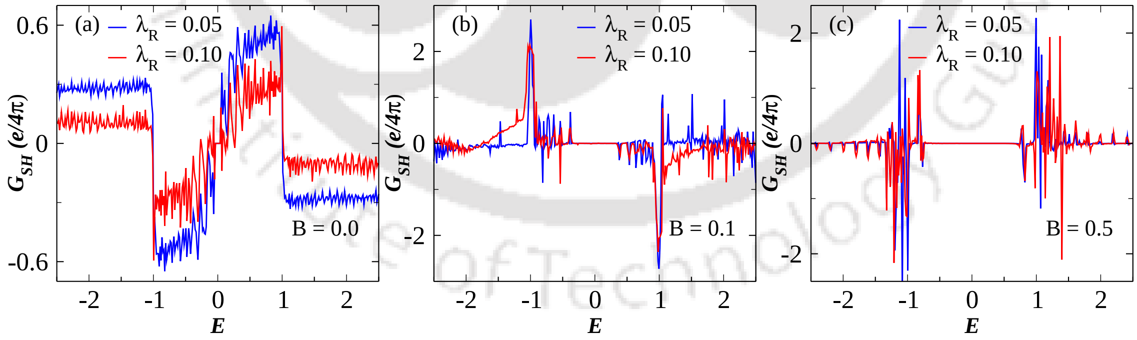

Figure 7.7: G_{SH} is plotted as a function of the Fermi energy for two different strengths of RSOC, namely $\lambda_R = 0.05$ and 0.1. (a) G_{SH} is antisymmetric as a function of the Fermi energy in the absence of the magnetic field. (b) The strength of the magnetic field is set at $B = 0.1$ and (c) $B = 0.5$. Though the magnetic field destroys the time reversal symmetry, still the spin Hall conductance can be observed.

In a usual Hall effect experiment, the charges accumulate at the transverse edges of a rectangular sample when a longitudinal current is passed through the sample and a magnetic field is applied in the z-direction. On the other hand, in presence of finite Rashba SOC, the up and down spins accumulate along the transverse edges of a rectangular sample when a current is allowed to pass along the longitudinal direction. As a result, a non-zero spin current is observed. Therefore it will be interesting and complementary to the preceding discussion, to observe the behaviour of spin Hall effect in presence of a magnetic field.

In principle, for spintronic applications, the existence of all the three components of the spin Hall conductance is important and they need to be computed (see Eq.(7.6)), however, to keep our discussion brief and without loosing any qualitative information, we calculate only the z component of the spin Hall conductance. We thus denote the z component of the spin Hall conductance as G_{SH}.

Fig.7.7 shows the variation of the spin Hall conductance G_{SH} (in units of $e/4\pi$) as a function of the Fermi energy. We take two different strengths of ROSC, namely, $\lambda_R = 0.05$ and 0.1. Fig.7.7(a) shows the behaviour of G_{SH} in absence of a magnetic field. G_{SH} is antisymmetric as a function of the Fermi energy, E, which ensures the electron-hole symmetry in the system[135]. As we include the magnetic field, though the time reversal symmetry is broken, the spin Hall effect still can be observed owing to the presence of the Rashba term as shown in Fig.7.7(b) and Fig.7.7(c). We have also taken two different values of the magnetic field, namely $B = 0.1$ and 0.5 respectively. The antisymmetric nature of G_{SH} is completely destroyed owing to the violation of the time reversal symmetry. Further, the magnitude of the maximum G_{SH} shows a considerable increase (by a factor of three) in presence of the magnetic field. Moreover, around $E = 0$, G_{SH} becomes close to zero. As we increase the strength of the magnetic field, the range of the Fermi energy increases over which G_{SH} is almost zero. The fluctuations in G_{SH} are due to the finite-size effects, mainly originating from the presence of a finite number of open channels in the leads and may be due to the spin precession effect[157,182].

7.3 Conclusion

In the present chapter, we have studied the behaviour of charge and spin Hall conductances as well as the longitudinal conductance in presence of a magnetic field and Rashba SOC in a six terminal graphene nanoribbon. We observe the IQHE in presence of magnetic field where the charge Hall conductance shows discrete step-like behaviour and the steps are quantized in units of $n\,(2e^2/h)$ (n being an integer). The inclusion of Rashba SOC almost destroys the IQH effect, however, smaller plateaus are still observed. The effect of the breaking of the time reversal symmetry is seen in the LDOS plots. Further, in presence of a magnetic field, the behaviour of the spin Hall conductance is studied. We observe that the antisymmetric nature of G_{SH} is destroyed owing to the broken time reversal symmetry.

Chapter 8

Conclusion

The study of mesoscopic systems is still a relatively recent topic, has already gained a wide attraction in condensed matter physics due to its possible future applications in nanoelectronics and spintronics devices. On the other hand, graphene is one of the most suitable candidates to study in this field of research, not only because of its various exciting electronic properties but also for the successful realization in the form of graphene nanoribbon, carbon nanotube, graphene flakes etc., in the mesoscale regime. Motivated by this, we have studied the quantum transport, specifically the spin transport in presence of spin-orbit interaction using Landauer-Büttiker formula and recursive Green's function technique. We have developed a code to calculate the two terminal charge conductance including disorder. However, in most parts of the thesis, we have used Kwant.

As a startup problem, a four terminal cross-shaped device, modeled on a tight-binding square lattice, is taken. Here we have studied the interplay between the Rashba spin-orbit interaction and onsite disorder on the longitudinal conductance, spin Hall conductance, and the spin Hall conductance fluctuations. We have shown that there is no universal nature of the spin Hall conductance fluctuation in presence of both disorder and Rashba SOC. Moreover, using the celebrated one parameter scaling theory, we did not found any onset of a metallic behaviour contrary to the findings of some of the existing literature. One interesting point of our result is that the longitudinal conductance decreases with increasing the Rashba SOC strength, that is the spin-orbit term behaves like a disorder, whereas, the spin Hall conductance increases with increasing the Rashba SOC strength.

In the subsequent discussion, we have shown that the spin polarization axis also plays an important role in quantum transport in presence of spin-orbit interactions, since the SOC destroy the rotational symmetry in spin space. Here we took a novel three terminal Y-shaped device. The angular separation between the two arms of the Y geometry plays a crucial role in measuring the charge and spin Hall conductances.

The next two consecutive chapters are dedicated to adatom decorated graphene nanoribbons. The first one is based on non-magnetic adatoms, where we have shown that for the two terminal case, by increasing the Au adatoms, one can generate all the three components of the spin polarized conductance. Here, we also show that by increasing the intrinsic spin-orbit interaction strength, the QSH phase can be restored, which was destroyed for the case of Au adatom decorated nanoribbons. We have also done a corresponding study for a four terminal device in presence of Au and Tl adatoms, where the quantum spin Hall effect can be observed.

The theoretical model for the Au-like adatoms was based on Kane-Mele model, while for the case of magnetic adatoms, the scenario is different. Magnetic adatoms, such as Fe, generates an exchange field due to the hybridization between carbon π-states and Fe atoms $3d$-state. Here we also were able to generate all the three components of the spin polarized conductance but with a greater magnitude than the non-magnetic case, since Fe adatoms induce a larger Rashba interaction. Thus we have been able to address both the fundamental physics originating due to the presence of the quantum spin Hall phase which is protected by the time reversal invariance and the technological aspects of spintronic applications of adatom decorated graphene nanoribbons.

In the last chapter, we have included a study on charge and spin transport in presence of an external magnetic field in addition to Rashba SOC for a six terminal graphene nanoribbon and revisited the integer quantum Hall effect. Since the Rashba SOC is present in the system, spin Hall effect is also observed. However, due to the presence of magnetic field, the system looses its time reversal symmetry. A consequence of this fact is studied on the spin Hall effect, which in a way destroy the antisymmetric nature of the spin Hall conductance. To summarize, the effects of spin-orbit interaction on the (integer) quantum Hall effect and magnetic field on the spin Hall physics are studied, RSOC destroys the Hall plateaus, and the magnetic field disrupts a familiar antisymmetric feature of the spin Hall conductance.

Bibliography

[1] R. Landauer, IBM Journal of Research and Development **1**, 223 (1957).

[2] S. Datta, *Electronic Transport in Mesoscopic Systems*, Cambridge University Press, Cambridge, UK, 1995.

[3] N. K. P. R. Mello, *Quantum Transport in Mesoscopic Systems: Complexity and Statistical Fluctuations*, Oxford University Press, New York, 2004.

[4] T. Ando, Y. Arakawa, K. Furuya, S. Komiyama, and H. N. (Eds.), *Mesoscopic Physics and Electronics*, Springer, New York, 1998.

[5] K. v. Klitzing, G. Dorda, and M. Pepper, Phys. Rev. Lett. **45**, 494 (1980).

[6] Y. Aharonov and D. Bohm, Phys. Rev. **115**, 485 (1959).

[7] R. A. Webb, S. Washburn, C. P. Umbach, and R. B. Laibowitz, Phys. Rev. Lett. **54**, 2696 (1985).

[8] Y. Imry, *Electronic transport in Mesoscopic systems*, Oxford University Press, New York, 1997.

[9] B. J. van Wees, H. van Houten, C. W. J. Beenakker, J. G. Williamson, L. P. Kouwenhoven, D. van der Marel, and C. T. Foxon, Phys. Rev. Lett. **60**, 848 (1988).

[10] D. A. Wharam et al., Journal of Physics C: Solid State Physics **21**, L209 (1988).

[11] P. A. Lee, A. D. Stone, and H. Fukuyama, Phys. Rev. B **35**, 1039 (1987).

[12] G. Bergmann, Physics Reports **107**, 1 (1984).

[13] P. A. Lee and T. V. Ramakrishnan, Rev. Mod. Phys. **57**, 287 (1985).

[14] R. G. García, Applied Physics Letters **60**, 1960 (1992).

[15] M. A. McCord and R. F. W. Pease, Journal of Vacuum Science & Technology B: Microelectronics Processing and Phenomena **4**, 86 (1986).

[16] R. J. Colton, C. R. K. Marrian, A. Snow, and D. Dilella, Journal of Vacuum Science & Technology B: Microelectronics Processing and Phenomena **5**, 1353 (1987).

[17] R. J. Colton, D. DiLella, R. L. Mowery, A. Snow, J. H. Wandass, and C. R. K. Marrian, Journal of Vacuum Science & Technology A: Vacuum, Surfaces, and Films **6**, 933 (1988).

[18] D. P. DiLella, J. H. Wandass, R. J. Colton, and C. R. K. Marrian, Review of Scientific Instruments **60**, 997 (1989).

[19] C. R. K. Marrian and R. J. Colton, Applied Physics Letters **56**, 755 (1990).

[20] E. A. Dobisz, C. R. K. Marrian, and R. J. Colton, Journal of Applied Physics **70**, 1793 (1991).

[21] M. N. Baibich et al., Phys. Rev. Lett. **61**, 2472 (1988).

[22] J. Barnaś, A. Fuss, R. E. Camley, P. Grünberg, and W. Zinn, Phys. Rev. B **42**, 8110 (1990).

[23] M. Tanaka, Journal of Crystal Growth **201**, 660 (1999).

[24] G. Prinz and K. Hathaway, Physics Today **48**, 4, 24 (1995).

[25] S. A. Wolf et al., Science **294**, 1488 (2001).

[26] G. Schmidt, D. Ferrand, L. W. Molenkamp, A. T. Filip, and B. J. van Wees, Phys. Rev. B **62**, R4790 (2000).

[27] L. D. Landau and E. M. Lifshitz, *Quantum Mechanics: Non-relativistic Theory (3rd edition)*, Pergamon Press, New York, 1991.

[28] G. Dresselhaus, Phys. Rev. **100**, 580 (1955).

[29] E. I. Rashba, Sov. Phys. Solid State **2**, 1109 (1960).

[30] G. Lommer, F. Malcher, and U. Rossler, Phys. Rev. Lett. **60**, 728 (1988).

[31] J. Nitta, T. Akazaki, H. Takayanagi, and T. Enoki, Phys. Rev. Lett. **78**, 1335 (1997).

[32] G. Engels, J. Lange, T. Schäpers, and H. Lüth, Phys. Rev. B **55**, R1958 (1997).

[33] S. Datta and B. Das, Applied Physics Letters **56**, 665 (1990).

[34] D. Frustaglia and K. Richter, Phys. Rev. B **69**, 235310 (2004).

[35] R. Ionicioiu and I. D'Amico, Phys. Rev. B **67**, 041307 (2003).

[36] J. E. Hirsch, Phys. Rev. Lett. **83**, 1834 (1999).

[37] S. Murakami, N. Nagaosa, and S.-C. Zhang, Science **301**, 1348 (2003).

[38] J. Sinova, D. Culcer, Q. Niu, N. A. Sinitsyn, T. Jungwirth, and A. H. MacDonald, Phys. Rev. Lett. **92**, 126603 (2004).

[39] K. S. Novoselov et al., Science **306**, 666 (2004).

[40] A. H. Castro Neto, F. Guinea, N. M. R. Peres, K. S. Novoselov, and A. K. Geim, Rev. Mod. Phys. **81**, 109 (2009).

[41] Y. Zhang, Y.-W. Tan, H. L. Stormer, and P. Kim, Nature **438**, 201 (2005).

[42] V. P. Gusynin and S. G. Sharapov, Phys. Rev. Lett. **95**, 146801 (2005).

[43] E.-J. Kan, Z. Li, J. Yang, and J. G. Hou, Applied Physics Letters **91**, 243116 (2007).

[44] X. Lin and J. Ni, Phys. Rev. B **84**, 075461 (2011).

[45] X. Du, I. Skachko, A. Barker, and E. Y. Andrei, Nat Nano **3**, 491 (2008).

[46] J. C. Meyer, A. K. Geim, K. S. Novoselov, T. J. Booth, and S. Roth, Nature **446**, 60 (2007).

[47] S. V. Morozov, K. S. Novoselov, M. I. Katsnelson, F. Schedin, L. A. Ponomarenko, D. Jiang, and A. K. Geim, Phys. Rev. Lett. **97**, 016801 (2006).

[48] K. Nakada, M. Fujita, G. Dresselhaus, and M. S. Dresselhaus, Phys. Rev. B **54**, 17954 (1996).

[49] K. Wakabayashi, M. Fujita, H. Ajiki, and M. Sigrist, Phys. Rev. B **59**, 8271 (1999).

[50] C. L. Kane and E. J. Mele, Phys. Rev. Lett. **95**, 226801 (2005).

[51] C. L. Kane and E. J. Mele, Phys. Rev. Lett. **95**, 146802 (2005).

[52] B. A. Bernevig and S.-C. Zhang, Phys. Rev. Lett. **96**, 106802 (2006).

[53] J. E. Moore, Nat Nano **464**, 194 (2010).

[54] M. Z. Hasan and C. L. Kane, Rev. Mod. Phys. **82**, 3045 (2010).

[55] X.-L. Qi and S.-C. Zhang, Rev. Mod. Phys. **83**, 1057 (2011).

[56] H. Min, J. E. Hill, N. A. Sinitsyn, B. R. Sahu, L. Kleinman, and A. H. MacDonald, Phys. Rev. B **74**, 165310 (2006).

[57] Y. Yao, F. Ye, X.-L. Qi, S.-C. Zhang, and Z. Fang, Phys. Rev. B **75**, 041401 (2007).

[58] M. König et al., Science **318**, 766 (2007).

[59] C. Weeks, J. Hu, J. Alicea, M. Franz, and R. Wu, Phys. Rev. X **1**, 021001 (2011).

[60] J. Hu, J. Alicea, R. Wu, and M. Franz, Phys. Rev. Lett. **109**, 266801 (2012).

[61] H. Jiang, Z. Qiao, H. Liu, J. Shi, and Q. Niu, Phys. Rev. Lett. **109**, 116803 (2012).

[62] O. Shevtsov, P. Carmier, C. Groth, X. Waintal, and D. Carpentier, Phys. Rev. B **85**, 245441 (2012).

[63] P. Esquinazi et al., Phys. Rev. B **66**, 024429 (2002).

[64] R. C. Longo, J. Carrete, and L. J. Gallego, The Journal of Chemical Physics **134**, 024704 (2011).

[65] A. V. Krasheninnikov, P. O. Lehtinen, A. S. Foster, P. Pyykkö, and R. M. Nieminen, Phys. Rev. Lett. **102**, 126807 (2009).

[66] E. J. G. Santos, A. Ayuela, and D. Snchez-Portal, New Journal of Physics **12**, 053012 (2010).

[67] Y. Mao, J. Yuan, and J. Zhong, Journal of Physics: Condensed Matter **20**, 115209 (2008).

[68] C. Cao, M. Wu, J. Jiang, and H.-P. Cheng, Phys. Rev. B **81**, 205424 (2010).

[69] N. K. Jaiswal and P. Srivastava, Physica E: Low-dimensional Systems and Nanostructures **54**, 103 (2013).

[70] Z. Qiao et al., Phys. Rev. B **82**, 161414 (2010).

[71] D. J. Griffiths, *Introduction to Quantum Mechanics*, Prentice-Hall, New Jersey, 1994.

[72] W. Greiner, *Relativistic quantum mechanics*, Springer, Germany, 1987.

[73] M. I. D'yakonov, Nature Material **14**, 871 (2015).

[74] R. Winkler, *Spin-Orbit Coupling effects in Two-Dimensional Electron and Hole Systems*, Springer, Germany, 2003.

[75] M. I. D'yakonov, Sov. Phys. Semicond. **20**, 110 (1986).

[76] N. A. Sinitsyn, E. M. Hankiewicz, W. Teizer, and J. Sinova, Phys. Rev. B **70**, 081312 (2004).

[77] D. Bercioux and P. Lucignano, Reports on Progress in Physics **78**, 106001 (2015).

[78] L. P. Z. B. K. Nicolic and S. Souma, *Spin currents in semiconductor nanostructures: a nonequilibrium Green-function approach (Vol:1)*, Oxford University Press, Oxford, 2010.

[79] Z. Lin and W. Jun, Chinese Physics B **23**, 087202 (2014).

[80] P. R. Bandaru, Journal of Materials Science **42**, 1809 (2007).

[81] T. P. Pareek, Phys. Rev. Lett. **92**, 076601 (2004).

[82] J. Weis and K. von Klitzing, Philosophical Transactions of the Royal Society of London A: Mathematical, Physical and Engineering Sciences **369**, 3954 (2011).

[83] J.-H. Chen, C. Jang, S. Xiao, M. Ishigami, and M. S. Fuhrer, Nat Nano **3** (2008).

[84] A. K. Geim and P. Kim, Scientific American **298** (2008).

[85] P. R. Wallace, Phys. Rev. **71**, 622 (1947).

[86] F. D. M. Haldane, Phys. Rev. Lett. **61**, 2015 (1988).

[87] X.-L. Qi and S.-C. Zhang, Physics Today **63**, 33 (2010).

[88] D. J. Thouless, M. Kohmoto, M. P. Nightingale, and M. den Nijs, Phys. Rev. Lett. **49**, 405 (1982).

[89] B. Simon, Phys. Rev. Lett. **51**, 2167 (1983).

[90] X.-L. Qi, Y.-S. Wu, and S.-C. Zhang, Phys. Rev. B **74**, 045125 (2006).

[91] M. Knig, H. Buhmann, L. W. Molenkamp, T. Hughes, C.-X. Liu, X.-L. Qi, and S.-C. Zhang, Journal of the Physical Society of Japan **77**, 031007 (2008).

[92] R. Seshadri, K. Sengupta, and D. Sen, Phys. Rev. B **93**, 035431 (2016).

[93] W. G. Christoph, W. Michael, R. A. Anton, and W. Xavier, New Journal of Physics **16**, 063065 (2014).

[94] E. Abrahams, P. W. Anderson, D. C. Licciardello, and T. V. Ramakrishnan, Phys. Rev. Lett. **42**, 673 (1979).

[95] D. K. Schroder, *Semiconductor material and device characterization*, Chapter 2, John Wiley and Sons, New York, 1990.

[96] H. Haug and A. P. Jauho, *Quantum Kinetics in Transport and Optics of Semi-Conductors*, Springer-Verlag, Germany, 1998.

[97] A.-P. Jauho, N. S. Wingreen, and Y. Meir, Phys. Rev. B **50**, 5528 (1994).

[98] R. Kubo, Journal of the Physical Society of Japan **12**, 570 (1957).

[99] S. Datta, *Quantum Transport: Atom to Transistor*, Cambridge University Press, Cambridge, 2005.

[100] D. S. Fisher and P. A. Lee, Phys. Rev. B **23**, 6851 (1981).

[101] Y. Imry, *'Physics of mesoscopin systems' in Directions in Condensed Matter Physics*, World Scientific Press, Singapore, 1986.

[102] B. K. Nikolić, Phys. Rev. B **64**, 014203 (2001).

[103] S. G. D.K. Ferry, *Transport in Nanostructures*, Cambridge University Press, Cambridge, 1997.

[104] P. Drouvelis, P. Schmelcher, and P. Bastian, Journal of Computational Physics **215**, 741 (2006).

[105] M. Wimmer and K. Richter, Journal of Computational Physics **228**, 8548 (2009).

[106] M. Duckheim, D. Loss, M. Scheid, K. Richter, i. d. I. m. c. Adagideli, and P. Jacquod, Phys. Rev. B **81**, 085303 (2010).

[107] V. A. Gopar, D. Weinmann, R. A. Jalabert, and R. L. Stamps, Phys. Rev. B **69**, 014426 (2004).

[108] B. K. Nikoli and R. L. Dragomirova, Semiconductor Science and Technology **24**, 064006 (2009).

[109] K. Kazymyrenko and X. Waintal, Phys. Rev. B **77**, 115119 (2008).

[110] G. Thorgilsson, G. Viktorsson, and S. Erlingsson, Journal of Computational Physics **261**, 256 (2014).

[111] L. V. Keldysh, Sov. Phys. JETP **20**, 256 (1965).

[112] L. P. Kadanoff and G. Baym, *Quantum Statistical Mechanics*, W. A. Benjamin, Inc., Menlo Park, California, 1962.

[113] J. Taylor, H. Guo, and J. Wang, Phys. Rev. B **63**, 245407 (2001).

[114] R. Lake, G. Klimeck, R. C. Bowen, and D. Jovanovic, Journal of Applied Physics **81**, 7845 (1997).

[115] A. Svizhenko, M. P. Anantram, T. R. Govindan, B. Biegel, and R. Venugopal, Journal of Applied Physics **91**, 2343 (2002).

[116] V. N. Do, P. Dollfus, and V. L. Nguyen, Journal of Applied Physics **100**, 093705 (2006).

[117] D. D. Awschalom, D. Loss, and N. Samarth, *Semiconductor Spintronics and Quantum Computation*, Springer Berlin Heidelberg, Berlin, Heidelberg, 2002.

[118] L. Sheng, D. N. Sheng, and C. S. Ting, Phys. Rev. Lett. **94**, 016602 (2005).

[119] A. A. Burkov, A. S. Núñez, and A. H. MacDonald, Phys. Rev. B **70**, 155308 (2004).

[120] J. Schliemann and D. Loss, Phys. Rev. B **69**, 165315 (2004).

[121] Y. K. Kato, R. C. Myers, A. C. Gossard, and D. D. Awschalom, Science **306**, 1910 (2004).

[122] V. Sih, R. C. Myers, Y. K. Kato, W. H. Lau, A. C. Gossard, and D. D. Awschalom, Nat Phys. **1**, 31 (2005).

[123] J. Stephens, R. K. Kawakami, J. Berezovsky, M. Hanson, D. P. Shepherd, A. C. Gossard, and D. D. Awschalom, Phys. Rev. B **68**, 041307 (2003).

[124] J.-i. Inoue, G. E. W. Bauer, and L. W. Molenkamp, Phys. Rev. B **70**, 041303 (2004).

[125] Y. Araki, G. Khalsa, and A. H. MacDonald, Phys. Rev. B **90**, 125309 (2014).

[126] D. Di Sante, P. Barone, E. Plekhanov, S. Ciuchi, and S. Picozzi, Sci. Rep. **5**, 11285 (2015).

[127] P. A. Lee and A. D. Stone, Phys. Rev. Lett. **55**, 1622 (1985).

[128] W. Ren, Z. Qiao, J. Wang, Q. Sun, and H. Guo, Phys. Rev. Lett. **97**, 066603 (2006).

[129] Z. Qiao, J. Wang, Y. Wei, and H. Guo, Phys. Rev. Lett. **101**, 016804 (2008).

[130] Z. QIAO, W. REN, and J. WANG, Modern Physics Letters B **25**, 359 (2011).

[131] M. Dey, S. K. Maiti, and S. N. Karmakar, Journal of Applied Physics **112**, 024322 (2012).

[132] M. Büttiker, Phys. Rev. Lett. **57**, 1761 (1986).

[133] R. Landauer, Philosophical Magazine **21**, 863 (1970).

[134] C. Caroli, R. Combescot, P. Nozieres, and D. Saint-James, Journal of Physics C: Solid State Physics **4**, 916 (1971).

[135] C. Moca and D. C. Marinescu, Phys. Rev. B **72**, 165335 (2005).

[136] J. Li, L. Hu, and S.-Q. Shen, Phys. Rev. B **71**, 241305 (2005).

[137] J. SCHLIEMANN, International Journal of Modern Physics B **20**, 1015 (2006).

[138] O. Dimitrova, Phys. Rev. B **71**, 245327 (2005).

[139] M. I. Dyakonov and V. I. Perel, JETP Lett. **13**, 467 (1971).

[140] M. Dyakonov and V. Perel, Physics Letters A **35**, 459 (1971).

[141] I. Žutić, J. Fabian, and S. Das Sarma, Rev. Mod. Phys. **76**, 323 (2004).

[142] B. K. Nikolić, L. P. Zârbo, and S. Souma, Phys. Rev. B **72**, 075361 (2005).

[143] L. Sheng, D. N. Sheng, and C. S. Ting, Phys. Rev. Lett. **94**, 016602 (2005).
[144] M. Yamamoto, J. Paaske, and P. Lindelof, Science **299**, 5607 (2003).
[145] A. Cummings, R. Akis, and D. Ferry, Applied Physics Letters **89** (2006).
[146] A. Cummings, R. Akis, D. Ferry, J. Jacob, T. Matsuyama, U. Merkt, and G. Meier, Journal of Applied Physics **104** (2008).
[147] P. Wójcik and J. Adamowski, Semiconductor Science and Technology **31**, 035021 (2016).
[148] D. Csontos and H. Q. Xu, Phys. Rev. B **67**, 235322 (2003).
[149] D. Liang and X. P. Gao, Nano Letters **12**, 3263 (2012), PMID: 22545669.
[150] E. G. Mishchenko and B. I. Halperin, Phys. Rev. B **68**, 045317 (2003).
[151] J. Schliemann and D. Loss, Phys. Rev. B **68**, 165311 (2003).
[152] Y. H. Park, H. jun Kim, J. Chang, S. H. Han, J. Eom, H.-J. Choi, and H. C. Koo, Applied Physics Letters **103**, 252407 (2013).
[153] A. Sasaki et al., Nat. Nanotechnol **9**, 703 (2014).
[154] P. D. C. King et al., Phys. Rev. Lett. **107**, 096802 (2011).
[155] K. Ishizaka et al., Nat Mater **10**, 521 (2011).
[156] S. D. Ganichev et al., Phys. Rev. Lett. **92**, 256601 (2004).
[157] L. Sheng and C. Ting, Physica E: Low-dimensional Systems and Nanostructures **33**, 216 (2006).
[158] K. I. Bolotin, K. J. Sikes, J. Hone, H. L. Stormer, and P. Kim, Phys. Rev. Lett. **101**, 096802 (2008).
[159] B. A. Bernevig, T. L. Hughes, and S.-C. Zhang, Science **314**, 1757 (2006).
[160] D. V. Tuan, F. Ortmann, D. Soriano, S. O. Valenzuela, and S. Roche, Nat Nano **10**, 857 (2014).
[161] K. T. Chan, J. B. Neaton, and M. L. Cohen, Phys. Rev. B **77**, 235430 (2008).
[162] D. W. Boukhvalov and M. I. Katsnelson, Applied Physics Letters **95**, 023109 (2009).
[163] E.-J. Kan, H. J. Xiang, J. Yang, and J. G. Hou, The Journal of Chemical Physics **127**, 164706 (2007).
[164] H. Sevinçli, M. Topsakal, E. Durgun, and S. Ciraci, Phys. Rev. B **77**, 195434 (2008).
[165] V. A. Rigo, T. B. Martins, A. J. R. da Silva, A. Fazzio, and R. H. Miwa, Phys. Rev. B **79**, 075435 (2009).
[166] W. H. Brito and R. H. Miwa, Phys. Rev. B **82**, 045417 (2010).
[167] D. Van Tuan, J. M. Marmolejo-Tejada, X. Waintal, B. K. Nikolić, S. O. Valenzuela, and S. Roche, Phys. Rev. Lett. **117**, 176602 (2016).
[168] A. Cresti, B. K. Nikolić, J. H. Garcia, and S. Roche, Rivista Del Nuovo Cimento **39**, 12 (2016).
[169] P.-H. Chang, F. Mahfouzi, N. Nagaosa, and B. K. Nikolić, Phys. Rev. B **89**, 195418 (2014).
[170] J. Klinovaja and D. Loss, Phys. Rev. X **3**, 011008 (2013).
[171] L. Chico, A. Latge, and L. Brey, Phys. Chem. Chem. Phys. **17**, 16469 (2015).
[172] Q. Zhang, K. S. Chan, and J. Li, Phys. Chem. Chem. Phys. **19**, 6871 (2017).
[173] Q. Zhang, Z. Lin, and K. S. Chan, Applied Physics Letters **102**, 142407 (2013).

[174] J.-F. Liu, K. S. Chan, and J. Wang, Nanotechnology **23**, 095201 (2012).
[175] Z. F. Wang, Q. Li, H. Zheng, H. Ren, H. Su, Q. W. Shi, and J. Chen, Phys. Rev. B **75**, 113406 (2007).
[176] H. Zheng and W. Duley, Phys. Rev. B **78**, 045421 (2008).
[177] L. L. Song, X. H. Zheng, R. L. Wang, and Z. Zeng, The Journal of Physical Chemistry C **114**, 12145 (2010).
[178] H. Zeng, J. Zhao, J. W. Wei, and H. F. Hu, The European Physical Journal B **79**, 335 (2011).
[179] X. H. Zheng, L. L. Song, R. N. Wang, H. Hao, L. J. Guo, and Z. Zeng, Applied Physics Letters **97**, 153129 (2010).
[180] H. Zhang et al., Journal of Applied Physics **117**, 113902 (2015).
[181] R. C. Longo, J. Carrete, and L. J. Gallego, Phys. Rev. B **83**, 235415 (2011).
[182] S. Ganguly and S. Basu, Physica E: Low-dimensional Systems and Nanostructures **90**, 131 (2017).
[183] L. Sheng and C. Ting, Physica E: Low-dimensional Systems and Nanostructures **33**, 216 (2006).
[184] A. Hartland, Metrologia **29**, 175 (1992).
[185] D. Marchenko et al., Nat. Commun. **3**, 1232 (2012).
[186] Y. S. Dedkov, M. Fonin, U. Rüdiger, and C. Laubschat, Phys. Rev. Lett. **100**, 107602 (2008).
[187] F. Calleja et al., Nat. Commun. **11**, 43 (2015).
[188] R. Peierls, Z. Physik **80**, 763 (1933).
[189] D. R. Hofstadter, Phys. Rev. B **14**, 2239 (1976).
[190] S. K. Maiti, M. Dey, and S. Karmakar, Physics Letters A **376**, 1366 (2012).

Vita

Sudin Ganguly was born on 13th August, 1984 in Kolkata, India. He did his B.Sc. with Physics Honours in 2008 from Vidyasagar Evening College, under University of Calcutta and M.Sc. in physics from West Bengal State University in 2010. He did Mphil in 2012 from Ramakrishna Mission Vivekananda University. He had enrolled into the Ph.D programme at Indian Institute of Technology Guwahati in 2012. He had qualified Graduate Aptitude Test in Engineering (GATE) in 2012 and CSIR-UGC NET in 2014. He has earned the Senior Research Fellowship in 2014 by Indian Institute of Technology Guwahati.